

# **ELASTIC PROPERTIES OF CLAYS**

by

Arpita Pal Bathija

A thesis submitted to the Faculty and the Board of Trustees of the Colorado School of Mines in partial fulfillment of the requirements for the degree of Doctor of Philosophy (Geophysics).

Golden, Colorado

Date \_\_\_\_\_

Signed: \_\_\_\_\_  
Arpita Pal Bathija

Approved: \_\_\_\_\_  
Dr. Manika Prasad  
Professor of Petroleum Engineering  
Thesis Advisor

Approved: \_\_\_\_\_  
Dr. Michael L. Batzle  
Professor of Geophysics  
Thesis Advisor

Golden, Colorado

Date \_\_\_\_\_

\_\_\_\_\_  
Dr. Terence K. Young  
Professor and Head,  
Department of Geophysics

## ABSTRACT

We adopted a multi-method approach to find and understand the elastic properties of clays, utilizing current advancements in technology, consisting of modeling and experiments so that they complement and validate each other. These methods range from molecular studies at angstrom scale to bulk shales at centimeter scale. The first method modeled clay interlayer properties using Monte Carlo molecular simulation for different stresses and number of interlayer water molecules. Our analyses of the equilibrium molecular structure of montmorillonite at various stresses and hydration states show that swelling behaves in a non-linear fashion with stress. This study establishes that the swelling behavior of clays under stress cannot be simply explained by bulk liquid water properties, but is an intricate interplay of the siloxane surface, cation solvation effects and stress on the interlayer water. The change in clay interlayer thickness with stress was used to calculate Young's modulus (5 GPa to 16 GPa). The arrangement of water molecules in the interlayer leads to their density variations. The density variations explain the changes in modulus of the interlayer water.

The second method was the nanoindentation study. The orientation and water content in our samples were confirmed to reduce the number of unknown parameters. Nanoindentation measurements of muscovite film on glass substrate showed that contact area can be estimated correctly and easily if the film and substrate have similar elastic properties. Larger grain sizes, lower strain rates and harder material help in achieving a better contact with the indenter tip, thereby yielding better results. Our simulation results (5 GPa to 16 GPa) matched very well with our experimental results

(4 GPa to 14 GPa) for Young's modulus, showing the dominant role of interlayer in defining the clay property.

The third method, which was at a larger scale, examined the deformation of shale sample. Experiments were conducted to study the dilation factor ( $R$ ) under different stress conditions on sandstones and shale.  $R$  has significant implications for time-lapse(4D) seismic studies where it can be used to infer reservoir or overburden thickness changes from seismic data, but is not well understood. We found that  $R$  values are dependent on the deformation mechanisms causing the strain.  $R$  values are different for P and S waves, especially in the presence of fluids.  $R$  values are also found to be strongly dependent on the stress state, implying that the use of a constant value of  $R$  from the seafloor to the reservoir depth should be avoided. This study shows that absolute  $R$  values increase for sandstones and decrease for shales with decreasing confining pressure, which explains the low  $R$  values obtained from 4D seismic data. Our data not only offers insights into the behavior of  $R$  values with different rock types, stress and fluid but can also be used to constrain the models. The static Young's modulus (2.6 GPa to 5 GPa) was calculated from the strain in the shale sample at different stress states.

This combination of physical measurements and computational modeling allows us to understand and predict in situ shale properties, which are essential for the interpretation and modeling of their seismic response.

## TABLE OF CONTENTS

|  |     |
|--|-----|
| ABSTRACT . . . . .                           | iii |
| LIST OF FIGURES . . . . .                    | vii |
| LIST OF TABLES . . . . .                     | x   |
| ACKNOWLEDGMENT . . . . .                     | xi  |
| Chapter 1 INTRODUCTION . . . . .             | 1   |
| 1.1 General Overview . . . . .               | 1   |
| 1.1.1 Clay Mineralogy . . . . .              | 1   |
| 1.2 Literature Review . . . . .              | 3   |
| 1.3 Importance . . . . .                     | 9   |
| 1.4 Overview of Chapters . . . . .           | 12  |
| Chapter 2 MOLECULAR SIMULATION . . . . .     | 15  |
| 2.1 Summary . . . . .                        | 15  |
| 2.2 Introduction . . . . .                   | 15  |
| 2.3 Literature Review . . . . .              | 16  |
| 2.4 Simulation Method . . . . .              | 20  |
| 2.5 Results . . . . .                        | 26  |
| 2.6 Conclusions . . . . .                    | 30  |
| Chapter 3 NANOINDENTATION . . . . .          | 39  |
| 3.1 Summary . . . . .                        | 39  |
| 3.2 Methodology . . . . .                    | 39  |
| 3.3 Sample Characterization . . . . .        | 44  |
| 3.3.1 Sample Preparation . . . . .           | 44  |
| 3.3.2 Scanning Electron Microscope . . . . . | 44  |
| 3.3.3 Thermal Analysis . . . . .             | 45  |
| 3.3.4 Optical Profiler . . . . .             | 47  |
| 3.4 Results . . . . .                        | 50  |
| 3.5 Conclusions . . . . .                    | 58  |

|            |  |        |
|------------|--|--------|
| Chapter 4  | AN EXPERIMENTAL STUDY OF THE DILATION FACTOR . | 63     |
| 4.1        | Summary . . . . .                              | 63     |
| 4.2        | Introduction . . . . .                         | 64     |
| 4.3        | Sample Description . . . . .                   | 66     |
| 4.3.1      | Lyons Sandstone . . . . .                      | 69     |
| 4.3.2      | Berea Sandstone . . . . .                      | 69     |
| 4.3.3      | Foxhill Sandstone . . . . .                    | 69     |
| 4.3.4      | North Sea Shale . . . . .                      | 69     |
| 4.3.5      | Rock Strength . . . . .                        | 70     |
| 4.4        | Method . . . . .                               | 72     |
| 4.4.1      | Theory . . . . .                               | 75     |
| 4.4.2      | Uncertainty Analysis . . . . .                 | 78     |
| 4.5        | Results . . . . .                              | 80     |
| 4.5.1      | Static vs. Dynamic . . . . .                   | 80     |
| 4.5.2      | Velocity . . . . .                             | 81     |
| 4.5.3      | Anisotropy . . . . .                           | 84     |
| 4.5.4      | Dilation Factor . . . . .                      | 86     |
| 4.5.5      | R Value Comparison . . . . .                   | 99     |
| 4.6        | Conclusions . . . . .                          | 100    |
| Chapter 5  | CONCLUSIONS . . . . .                          | 103    |
| 5.1        | Introduction . . . . .                         | 103    |
| 5.2        | Conclusions . . . . .                          | 103    |
| 5.3        | Suggestions for Future Work . . . . .          | 106    |
| REFERENCES | . . . . .                                      | 108    |
| APPENDIX   | . . . . .                                      | 117    |
| CD         | . . . . .                                      | Pocket |

## LIST OF FIGURES

|     |  |    |
|-----|--|----|
| 1.1 | Basic modular units of clays . . . . .   | 3  |
| 1.2 | Structure of clays as in kaolinite, muscovite and montmorillonite . . .  | 4  |
| 1.3 | Structure of clays in a 1:1 layer silicate and 2:1 layer silicate . . . . .  | 5  |
| 1.4 | Conceptual microstructure for smectite from Likos & Lu (2006). . . . .   | 13 |
| 2.1 | The stable structure from simulation run with no water molecules in the interlayer and a uniaxial stress of 1 Pa applied normal to the clay layers . . . . . | 22 |
| 2.2 | Hydration induced expansion in montmorillonite under stress . . . . .  | 34 |
| 2.3 | Simulated partial radial distribution functions (RDF) with varying water content for hydrated Na montmorillonite . . . . .                                   | 35 |
| 2.4 | Simulated partial radial distribution functions (RDF) with varying stress for hydrated Na montmorillonite . . . . .  | 36 |
| 2.5 | Young's modulus of the interlayer as a function of water molecules for a uniaxial stress difference of 1 GPa . . . . .                                       | 37 |
| 2.6 | Density of the interlayer water as a function of water molecules at a uniaxial stress of 1 GPa . . . . .   | 38 |
| 3.1 | A schematic representation of the experimental apparatus used to perform the nanoindentation experiments . . . . .   | 41 |
| 3.2 | Calibration of contact area variation with contact depth (Oliver & Pharr, 1992). . . . .   | 42 |
| 3.3 | Pile-up and sink-in leads to inaccurate contact area measurements (Oliver & Pharr, 1992). . . . .  | 43 |
| 3.4 | Environmental scanning electron micrograph of kaolinite (KGa 1b) . .   | 45 |
| 3.5 | Environmental scanning electron micrograph of montmorillonite (SWy 2)  | 46 |

|      |   |    |
|------|---|----|
| 3.6  | Water content in SWy 2 sample (as prepared) from thermal gravimetric analysis (TGA) . . . . .                                   | 48 |
| 3.7  | Thermal gravimetric analysis (TGA) and Derivative thermal gravimetric analysis (DTG) on SCa 3 sample . . . . .                  | 48 |
| 3.8  | Thermal gravimetric analysis (TGA) and Derivative thermal gravimetric analysis (DTG) on SWy 2 sample (as received) . . . . .    | 49 |
| 3.9  | Average roughness of the glass substrate measured using the Wyko optical profiler . . . . .                                     | 51 |
| 3.10 | Thickness of muscovite sample measured using the Wyko optical profiler  | 52 |
| 3.11 | Average roughness of muscovite sample measured using the Wyko optical profiler . . . . .  | 53 |
| 3.12 | Average roughness of kaolinite sample measured using the Wyko optical profiler . . . . .  | 54 |
| 3.13 | Thickness of montmorillonite sample measured using the Wyko optical profiler . . . . .  | 56 |
| 3.14 | Average roughness of montmorillonite sample measured using the Wyko optical profiler . . . . .                                  | 57 |
| 3.15 | Nanoindentation measurements on fused silica . . . . .  | 58 |
| 3.16 | Nanoindentation measurements on muscovite film over glass substrate   | 59 |
| 3.17 | Nanoindentation measurements on kaolinite (smaller grain sizes) (KGa 1b) over glass substrate . . . . .                         | 60 |
| 3.18 | Nanoindentation measurements on kaolinite film over glass substrate .   | 61 |
| 3.19 | Nanoindentation measurements on montmorillonite (SCa 3) over glass substrate . . . . .  | 62 |
| 4.1  | Schematic diagram of the shale sample prepared . . . . .  | 70 |
| 4.2  | Photograph of the Foxhill sample with strain gages and transducers attached to measure the deformation and velocities . . . . . | 74 |
| 4.3  | Measurement states where each point represents a location in stress space where velocities were measured . . . . .              | 75 |



|      |  |    |
|------|--|----|
| 4.4  | Velocity paths under hydrostatic and nonhydrostatic stresses for dry Berea sandstone . . . . .   | 79 |
| 4.5  | The ratio of dynamic to static Young's modulus in sandstones . . . . .   | 82 |
| 4.6  | Static versus dynamic Young's modulus in sandstones . . . . .  | 83 |
| 4.7  | Changes in velocities over initial velocity are plotted against change in hydrostatic pressure to find the qualitative influence of crack porosity in sandstones . . . . . | 85 |
| 4.8  | Axial velocity contours for dry and brine-saturated Berea . . . . .  | 87 |
| 4.9  | Axial and radial velocity contours for dry Foxhill . . . . .   | 88 |
| 4.10 | Axial and radial velocity contours for brine-saturated Foxhill . . . . .   | 89 |
| 4.11 | Modeled P-wave velocity as a function of crack density and alignment, assuming the pore fluid is incompressible by Hatchell & Bourne (2005b). . . . .                      | 89 |
| 4.12 | Anisotropy parameters plotted as a function of the axial stress . . . . .  | 90 |
| 4.13 | R values are plotted as a function of hydrostatic pressure . . . . .   | 92 |
| 4.14 | Strain as a function of hydrostatic pressure . . . . .   | 93 |
| 4.15 | Model calculations, illustrating the impact of flat cracks and spherical pores on the stress sensitivity of wave velocities . . . . .                                      | 94 |
| 4.16 | Sensitivity of R to fluid saturation and differential pressure . . . . .   | 95 |
| 4.17 | R with uniaxial stress . . . . .   | 96 |
| 4.18 | Change in velocities over initial velocity as a function of uniaxial stress . . . . .  | 97 |
| 4.19 | Strain versus uniaxial stress . . . . .  | 98 |

## LIST OF TABLES

|     |   |    |
|-----|---|----|
| 1.1 | Classification of phyllosilicates . . . . .   | 2  |
| 1.2 | Review table for clay modulus . . . . .   | 14 |
| 2.1 | Review table for clay hydration from early theoretical and experimental studies . . . . . | 20 |
| 2.2 | Review table for clay hydration from molecular simulation . . . . .                       | 32 |
| 2.3 | Parameters in the MCY potential function (Skipper <i>et al.</i> , 1995a). . .             | 33 |
| 3.1 | Nanoindentation measurements on KGa 1b . . . . .  | 55 |
| 3.2 | Nanoindentation measurements on SWy 2 . . . . .   | 55 |
| 3.3 | Nanoindentation measurements on SCa 3 . . . . .   | 55 |
| 4.1 | Review table for dilation factor (R) . . . . .  | 67 |
| 4.2 | Sample properties . . . . .   | 68 |
| 4.3 | Sample strength . . . . .   | 72 |

## ACKNOWLEDGMENT

There are many people who have contributed to this work and to the wonderful experience I have had at Colorado School of Mines.

First and foremost it has been a pleasure working with my Ph.D. co-advisor Manika Prasad. It is truly an honor to have been mentored by her. She is especially thanked for allowing me so much independence in my research pursuits, and for sharing all the excitements and disappointments that I felt over the years. It is difficult to overstate my gratitude to my Ph.D. co-advisor, Dr. Michael Batzle. With his enthusiasm and great efforts to explain things clearly and simply, he helped to make experiments fun for me. He provided encouragement, sound advice, good teaching, good company, and lots of good ideas. He was my main source of inspiration. I especially admire him for his sense of humor and patience, even when my samples broke down multiple times. I am truly grateful to both my advisors to believe in me, supporting me over the years and showing me the path to think freely on my own.

Before coming to CSM, Professor Jerry Harris served as a wonderful mentor at Stanford University, which laid the foundation for my PhD. I would also like to thank my manager at Spatial Data Private. Ltd., Dr. S. Rajagopalan for inspiring me into PhD program.

I am indebted to my colleagues in the Rock Abusers group, past and present, for their assistance and friendship. I would like to thank Haiyi Liang for writing the first version of the molecular simulation code. Prof. Ning Lu and Prof. Moneesh Upamanyu's help with molecular simulation is acknowledged. Prof. Richard Wend-

landt's help with technical details on clays and clay samples cannot be ignored. I am indebted to Prof. Ivar Reimanis, Dr. Rongjie Song and Masood Hashemi for their help with nanoindentation in the Material Science department at Colorado School of Mines. I am grateful to Prof. Ilya Tsvankin and Prof. Luis Tenorio for their valuable time and advice as my committee members. I would like to acknowledge Petroleum Research Fund, Clay Minerals Society and Fluids Consortium for financial support.

This work would not have been possible without the help and support from my husband, Arjun Bathija. My son, Rohil Pal Bathija's contribution in providing a loving environment and rejuvenating me every single day cannot be ignored. I am grateful for the multiple days that he spent with me in my laboratory and office playing all by himself. I am grateful to my brother Avishekh Pal for always having faith in me and supporting me throughout.

Finally, I would like to thank my parents, Minakshi Pal and Sankari Prasad Pal for their constant love and encouragement. Without their support I could have never realized this achievement.

## Chapter 1

### INTRODUCTION

#### 1.1 General Overview

Since shales are the most abundant sedimentary rocks on earth and clay minerals are a major constituent of shales, the elastic properties of clays are of utmost importance in soil science and geophysics. Several other disciplines such as material science, biological science, geology and engineering also use clays in various ways.

##### 1.1.1 Clay Mineralogy

Clay minerals are hydrous aluminum silicates and are classified as phyllosilicates (Table 1.1), or layer silicates. All layer silicates are constructed from two modular units: tetrahedral and octahedral sheets. The tetrahedron consists of one  $\text{Si}^{4+}$  atom surrounded by four  $\text{O}^{2-}$  atoms. The octahedron consists of a central  $\text{Al}^{3+}$  or  $\text{Mg}^{2+}$  atom surrounded by six  $\text{O}^{2-}$  atoms (Figure 1.1). The tetrahedron or octahedron are joined by shared oxygen atoms to form the sheets. The octahedral sheets can be trioctahedral (brucite-like) or dioctahedral (gibbsite-like). In the brucite-like sheet the cation-to-anion ratio is 1:2, so all three octahedral sites around each hydroxyl must be filled to have electrical neutrality. Whereas, in the gibbsite-like sheet the cation-to-anion ratio is 1:3, so only two of every three octahedral sites around each hydroxyl need to be filled to have electrical neutrality. The tetrahedral and octahedral sheets are stacked on top of each other (lamellae). The assemblage of one tetrahedral

sheet and one octahedral sheet is called a 1:1 layer silicate structure (Figure 1.2). In 2:1 layer silicate, an octahedral sheet is sandwiched between two tetrahedral sheets (Figure 1.3). Substitution of ions with approximately equal radii occur in tetrahedral and/or octahedral sheets, e.g.: tetrahedral sheets ( $\text{Al}^{3+}$  for  $\text{Si}^{4+}$ ) and octahedral sheets ( $\text{Mg}^{2+}$  for  $\text{Al}^{3+}$ ). Substitutions can cause unbalanced internal negative charges in the lamellae. Unbalanced negative charges are compensated by adsorption of ions near the external surfaces of the clay minerals.

Table 1.1. Classification of phyllosilicates

| Layer Type | Group        | Charge per unit formula | Subgroup         | Species         | Chemical Formula                                   |
|------------|--------------|-------------------------|------------------|-----------------|--|
| 1:1        | Kaolin       | 0                       | Kaolins(Di)      | Kaolinite       | $\text{Al}_4\text{Si}_4\text{O}_{10}(\text{OH})_8$ |
| 2:1        | Pyrophyllite | 0                       | Pyrophyllite(Di) | Pyrophyllite    | $\text{Al}_2\text{Si}_4\text{O}_{10}(\text{OH})_2$ |
| 2:1        | Smectite     | 0.2-0.6                 | Di smectites     | Montmorillonite | A  |
| 2:1        | Mica         | 1                       | Di micas         | Muscovite       | B  |

*Di=di octahedral;*

$A = R_{0.33}^{+}(\text{Al}_{1.67}\text{Mg}_{0.33})\text{Si}_4\text{O}_{10}(\text{OH})_2$ ,  $R$ =interlayer cation;

$B = (K)[(\text{Al}, \text{Fe}^{3+})_{2-x}(\text{Mg}, \text{Fe}^{2+})_x](\text{Si}_{3+x}\text{Al}_{1-x})\text{O}_{10}(\text{OH})_2$ .

*Based on Moore & Reynolds (1989).*

The smectite group of clay minerals with 2:1 layer structure is able to expand and contract its structures while maintaining its crystallographic integrity. Expansion takes place as water or some polar molecule, such as ethylene glycol, enters the interlayer space. The layers expand because the interlayer cations (R) such as  $\text{Na}^{+}$ ,  $\text{Mg}^{2+}$ ,  $\text{Ca}^{2+}$ ,  $\text{K}^{+}$ ,  $\text{Li}^{+}$ , etc. are attracted more to water than to the relatively small layer charge (Moore & Reynolds, 1989).

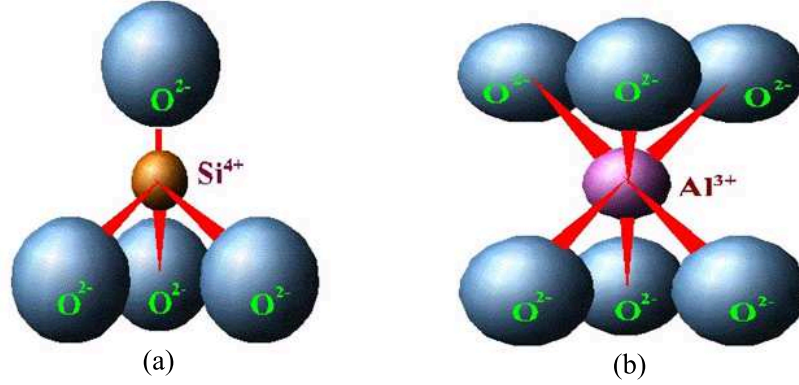


Figure 1.1. Basic modular units of clays: (a) Tetrahedron with one  $\text{Si}^{4+}$  atom surrounded by four  $\text{O}^{2-}$  atoms and (b) Octahedron with central  $\text{Al}^{3+}$  atom surrounded by six  $\text{O}^{2-}$  atoms.

## 1.2 Literature Review

The swelling of clay minerals in the presence of an aqueous solution can produce strong adverse effects in the production of pore fluids such as gas and oil (Zhang *et al.*, 2006). As pore-filling materials, they block hydraulic pathways and decrease permeability and porosity considerably but do not substantially affect seismic wave propagation. Pore-lining clay on the other hand will considerably alter seismic properties without a large effect on porosity (Tosaya, 1982; Han *et al.*, 1986; Prasad, 2001). Knowledge of the elastic properties of clay is therefore essential for the interpretation and modeling of the seismic response of clay bearing formations. Polymer, paper, ceramic, medicine, automobile and various other disciplines and industries also use clays. The swelling potential of clays present in soils needs to be assessed and treated before constructions. Presence of clays can increase or decrease the damage caused by an earthquake depending on whether they weaken or strengthen the underlying rock.

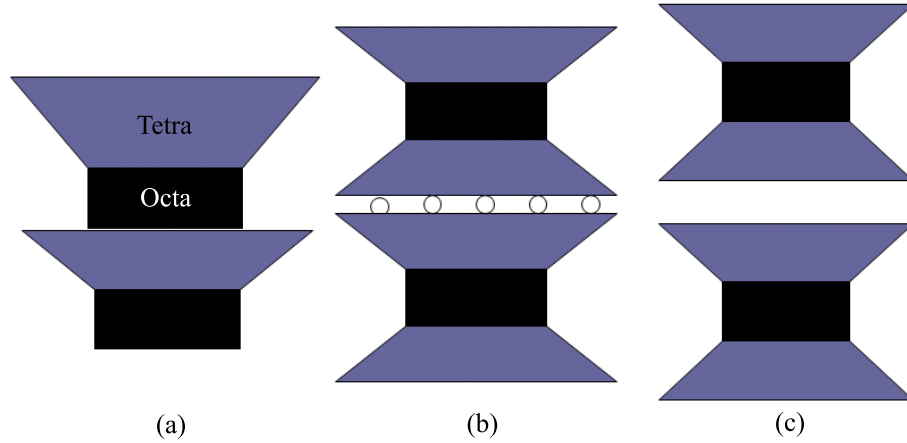


Figure 1.2. Structure of clays: (a) The assemblage of one tetrahedral sheet and one octahedral sheet is called a 1:1 layer silicate structure, as in kaolinite. (b) In 2:1 layer silicate, an octahedral sheet is sandwiched between two tetrahedral sheets with potassium ions in the interlayer, as in muscovite and (c) Another 2:1 layer silicate that can have water and cations in the interlayer, as in montmorillonite.

The stress response of materials is determined by their elastic properties and is studied by various techniques. These techniques include theoretical, experimental, computational (molecular simulations) and hybrid methods.

### Theoretical

Hornby *et al.* (1994) proposed a theory based on a combination of anisotropic formulations of the self-consistent approximation (SCA) and differential effective-medium (DEM) approximation. Their values for clay at zero porosity are bulk modulus ( $K$ ) of 22.9 GPa and shear modulus ( $G$ ) of 10.6 GPa. They predicted elastic tensors,  $C_{11}$  of 34 GPa and  $C_{33}$  of 22 GPa, estimated using a clay platelet angular distribution function derived from a digitized scanning electron microscope (SEM) image. This matched very well with the measured values for Cretaceous shale (Jones & Wang, 1981).



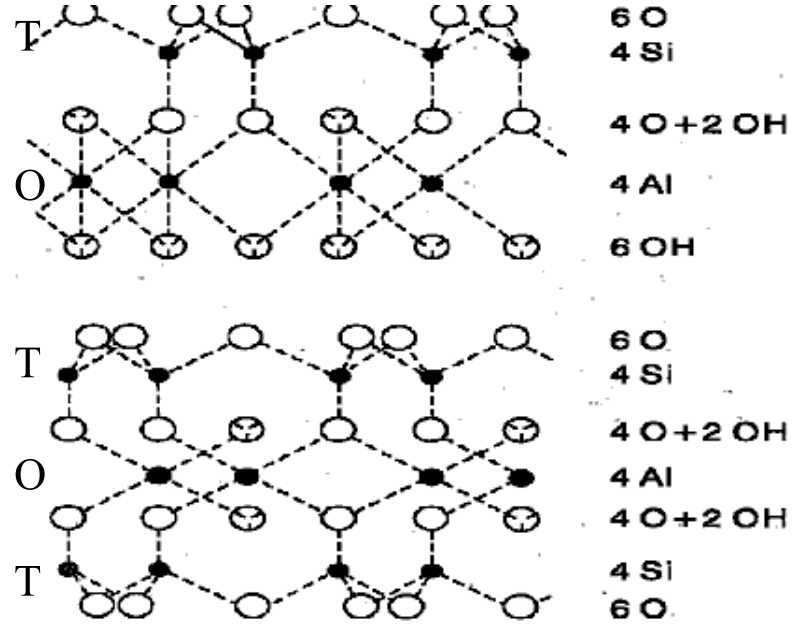


Figure 1.3. Structure of clays: The assemblage of one tetrahedral sheet (T) and one octahedral sheet (O) as in a 1:1 layer silicate is shown at the top and a 2:1 layer silicate with tetrahedra (T), octahedra (O) and tetrahedra (T) structure is shown at the bottom (Moore & Reynolds, 1989).

Elastic velocities for dry clay minerals have been estimated from published data on well-crystallized phyllosilicates (Katahara, 1996). But it is very difficult to obtain dry clay due to surface adsorbed water in its low aspect ratio pores. Moreover, clay orientation, anisotropy, and extrapolation of empirical trends beyond their range of validity have resulted in the over prediction of velocities.

Wang *et al.* (2001) extrapolated modulus values for montmorillonite and hectorite from epoxy-clay hybrids of 51 GPa and 69 GPa, respectively. The method is rather complex because it involves agglomeration, intercalation and exfoliation in the volume fraction range studied (0.35-0.85), and the effective volume fraction needs recalculation.

Using first principle density functional theory (DFT), the bulk modulus of kaolinite has been calculated to be 23 GPa and Young's modulus as 92 GPa, 170 GPa, and 31 GPa for the a, b, and c directions, respectively (Sato *et al.*, 2005). Chen & Evans (2006) estimated Young's modulus of bulk clay as 203 GPa using an empirical linear modulus-density relation for alumina, silica and their compounds. They concluded that the Young's modulus of clay platelets lies within the range 178-265 GPa and that this range does not significantly affect predicted nanocomposite moduli with up to 30% clay.

## Experimental

Brillouin scattering measurements (Vaughan & Guggenheim, 1986) on bulk muscovite mica gave in-plane moduli of the order of 170 GPa, while the modulus perpendicular to the layers is about 60 GPa. These layered clays are characterized by strong intralayer covalent bonds within the individual sheets comprising the clay, with only weak van der Waals interactions between adjacent clay sheets. This explains the relatively low modulus measured from compressibility (Faust & Knittle, 1994), as they are for  $C_{33}$ . Since the single clay platelets do not have the problems of layer stacking and shifting,  $C_{33}$  can be considered similar to  $C_{11}$  and  $C_{22}$  (Chen & Evans, 2006).

The laboratory values calculated from ultrasonic velocity measurements at a vertical stress of 200 kPa for dry clay-sand mixtures (Vallejo & Lobo-Guerrero, 2005) agreed very well with the theoretical method developed by others. The method allows the calculation of the elastic moduli of clays with large dispersed particles from the elastic moduli of the clay matrix and the concentration either by volume or weight of the large particles in the mixture. There was less agreement for samples having water contents of 10% and 20%. The samples were prepared with Ottawa sand and kaolinite

clay. They obtained values for Young's modulus of 0.15 GPa and shear modulus of 0.005 GPa for clay matrix with no sand to 0.25 GPa and 0.008 GPa for clays with 60% sand. Pure shale was viewed as an isotropic elastic solid and bulk modulus of 12.5 GPa and shear modulus of 6.0 GPa were derived from measurements on a sample with 25% porosity (Marion *et al.*, 1992). A Young's modulus value of 14 GPa was obtained for montmorillonite by extrapolation of acoustic measurements on cold-pressed samples having different porosities (Vanorio *et al.*, 2003). The low modulus can be attributed partly to the greater basal plane spacing in montmorillonite than in the other clays. Using ultrasonic P and S wave velocities, the bulk modulus of kaolinite was measured to lie between 6 and 12 GPa (Vanorio *et al.*, 2003).

Using acoustic resonance spectroscopy, a Young's modulus of 222 GPa was measured for a composite comprising alumina platelets (0.2 volume fraction) in a mullite matrix (Ledbetter *et al.*, 2001). This value was below pure mullite's value of 228 GPa, and far below the value predicted by a solid-mechanics model assuming good alumina-mullite interfaces: 256 GPa. They concluded that the mullite particles must be enveloped by silica, an elastically soft phase. Solid-mechanics modeling and electron microscope observations confirmed their conclusion.

Using atomic force acoustic microscopy and an assumed tip radius, a Young's modulus value of 6.2 GPa was measured in dickite (Prasad *et al.*, 2002). Attempts to measure the Young's modulus of an individual clay platelet using atomic force microscopy (Piner *et al.*, 2003) have been made. Unfortunately they found that impurities comprised of low molecular weight silicates as well as the intercalating salt used to process the clay like (NaOH) could not be removed from the surface of the platelets, preventing accurate measurements of the modulus of the platelets themselves.

Using a vibration resonance technique, it has been shown that Young's modulus and Poisson's ratio of industrially used silica or alumina materials are particularly sensitive to the peak temperature and soak times used for the firing operation (Aston *et al.*, 2002).

### **Simulations**

Manevitch & Rutledge (2004) obtained the product of modulus and platelet thickness by molecular dynamics (MD) simulation. The in-plane Young's modulus value of single platelets of montmorillonite, assuming effective plate thickness of 0.98 nm, is 255 GPa. The modulus of the interlayer and the two-clay-layer unit were found to be 13.18 GPa and 54.56 GPa, respectively using steered molecular dynamics simulations on dry pyrophyllite clay (Katti *et al.*, 2005b).

### **Hybrid method**

Palko *et al.* (2002) calculated velocities based on an initial set of preliminary elastic tensors  $C_{ij}$  along the same propagation directions as those measured and then varying the elastic moduli so as to minimize the misfit between the calculated and measured velocities. They also found the best fit values for the temperature derivatives of  $C_{ij}$  for mullite are valid up to 1200°C. The values predicted by this study are 173.5 GPa for bulk modulus, 88 GPa for shear modulus and 225.9 GPa for Young's modulus for polycrystalline mullite.

The different techniques provide a large range in the values of elastic moduli of clay minerals (Table 1.2): between 0.15 GPa from measurements (Vallejo & Lobo-Guerrero, 2005) and 400 GPa from calculations (Manevitch & Rutledge, 2004). Moreover, within each method are substantial variations in the reported results. This large

variation may be due to various kinds of clays, different external environments leading to varied amounts of cations and bound water in the interlayers or anisotropy owing to the layered structure of clays. The major challenges in measuring elastic properties of clay minerals are due to their small grain size, ease of reactions with polar molecules and low permeability. The layered atomic structure of clays leads to anisotropy such as that seen in mica whose elastic modulus in the perpendicular direction to the c-axis ( $C_{11}$ ,  $C_{22}$ ) is 3.5 times that along the c-axis ( $C_{33}$ ) (Habelitz *et al.*, 1997). Poisson's ratio calculated from Brillouin scattering data on muscovite (Mcneil & Grimsditch, 1993) varies between 0.11 to 0.48, which is very close to the full range of Poisson's ratio (0 to 0.5).

The clay structure is affected by the kind of water associated with it: free water and bound water. Bound water can be further subdivided into structural water attached to the clay layers and the water in the interlayer, in the case of multiple clay platelets. Heating might remove different types and amounts of water from the sample depending on the sample, heating temperature and duration. These can also lead to the variation in their properties.

Most seismic interpretations ignore the large variation in the elastic properties of clays and use a value of 22 GPa as the default clay mineral modulus (Hornby *et al.*, 1994). Despite their abundance and usage, the discrepancy in the material properties of clays is not fully understood.

### 1.3 Importance

This dissertation aims at understanding the discrepancy in the various values for elastic moduli in clay minerals, both numerically and experimentally. The presence

of clay minerals has significant consequences in the production of gas and oil. In the presence of water, some clay minerals may swell and cause considerable borehole stability problems (Zhang *et al.*, 2006). This research will help guide the risk assessment of reservoirs with high clay content undergoing enhanced oil recovery processes such as water flooding. Knowledge of the elastic properties of clay is also essential for the interpretation and modeling of the seismic response of clay bearing formations.

In nanocomposite formulation, the interlayer water is removed and the clays are intercalated with other materials, enhancing the polymer properties (Zunjarrao *et al.*, 2006). Yet, the same clay modulus is used in the design of new advanced polymers. First of all, the clay modulus is not well-constrained by direct measurements. And secondly, the change in clay modulus due to the difference in their interlayer is not taken into account. Origin of life in montmorillonite is under study in biological sciences (Ferris, 1993). Clays are also used to clean the environment by trapping toxic wastes in their interlayer. Presence of clays can increase or decrease the damage caused by an earthquake depending on whether they weaken or strengthen the underlying rock. The swelling potential of clays present in construction material needs to be assessed and treated before they can be used. Soil sciences will also benefit from this research as clay properties are needed to assess soil strength.

A multi-method approach to understand the elastic property of clays was adopted in this dissertation consisting of

- Molecular simulation of montmorillonite to obtain the equilibrium structures at various stresses and hydration states
- Nanoindentation measurements on clays, where a sharp indenter is loaded onto a sample and its response gives its mechanical properties

- Rock physics measurements on shale to obtain their dilation factor

A combination of different types of methods offer independent insights and assist in the interpretation of new results. Understanding the complex behavior of these nano clay minerals require experiments at that scale. Nanoscale measurements for mineral properties of swelling clays such as montmorillonite with quantifiable interlayer water under high stress have not been made before due to their small grain size, highly reactive behavior of these nano minerals to polar molecules, and lack of appropriate tools. A molecular simulation approach provides a means to simulate those measurements and nanoindentation is a way to perform those experiments.

The methodology for Monte Carlo simulation of interlayer molecular structure in swelling clay minerals is provided by Skipper *et al.* (1995a), but they did not study the effects of stress and higher water contents. Molecular simulations are expensive with respect to computer time which is one of the main reasons for the absence of comprehensive simulated data in the literature. A comprehensive study on swelling of clay minerals under varying stress and interlayer water content is done in this research.

Nanoindentation methodology for evaluating thin films on substrates is developed by Oliver & Pharr (1992), but no data exists on swelling clays in the literature using that methodology. There have been nanoindentation studies on muscovite with similar structure to clays (Barsoum *et al.*, 2004), kaolin mineral (Mikowski *et al.*, 2007), atomic force microscopy (Piner *et al.*, 2003) and atomic force acoustic microscopy studies on clays (Prasad *et al.*, 2002).

Shales are the most abundant sedimentary rock on earth and clays are a major constituent (over 30% by volume) of shales. The triaxial stress-strain system in the

Rock Physics Lab at Colorado School of Mines is the appropriate equipment for measuring ultrasonic properties of rocks along with their static properties. Moreover, very few people attempt experimental studies on shales as they take a long time to saturate and reach pore pressure equilibrium due to their low permeability. In addition, shales can be very sensitive to preparation, laboratory conditions and fluid chemistry. Therefore, the experimental data set obtained is unique and is available to the geophysics community through peer-reviewed publications.

Several sub-stacks of clay minerals form a quasicrystal with sub-stack porosity as shown in Figure 1.4. These quasicrystals form a network with varying interparticle porosity. The modeling can be extended to shale, by adding quartz grains to the clay networks (Hornby *et al.*, 1994). Our data will have applications in the upscaling of elastic properties from the molecular level to the bulk level. This work gave us data at molecular level (molecular simulation), intermediate level (nanoindentation) and bulk level (rock physics measurements on shale). Thus, this research provides insights into the elastic properties of these minerals which are still poorly constrained in seismic studies. The main contribution of this research is the data that can be used to constrain the models, the methods developed along the way to collect those data, and the insights gained from the analyses of the data.

## 1.4 Overview of Chapters

Starting from the atomistic scale, analyses of the equilibrium structures of the clay mineral under different conditions using the molecular simulation method are presented in Chapter 2. Experimental verification of the modeling results using nanoindentation method to find the elastic properties of these materials are presented in



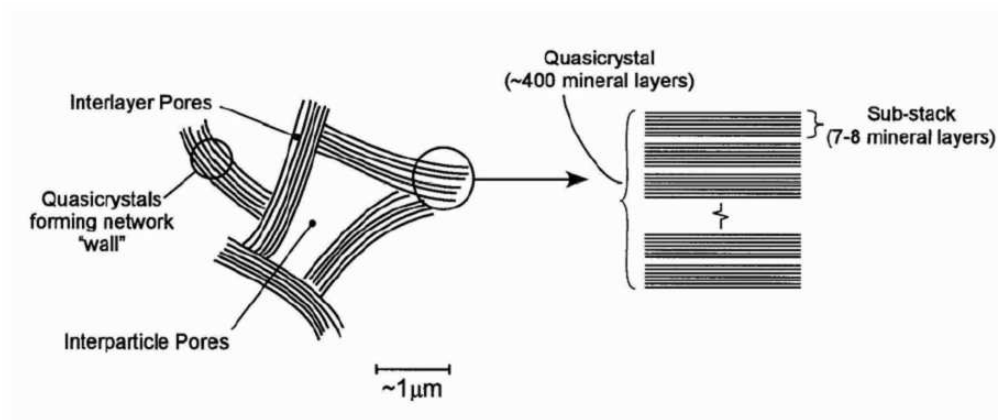


Figure 1.4. Conceptual microstructure for smectite from Likos & Lu (2006).

Chapter 3. Parts of Chapter 2 and Chapter 3 have been submitted as annual meeting abstracts for the Clay Minerals Society, the Society of Exploration Geophysicists (SEG) and as an article to the Geophysics journal. Moving to a larger scale, the ultrasonic measurements on sandstones and shale to measure their dilation factor and elastic modulus are discussed in Chapter 4. Parts of Chapter 4 have been submitted as an annual meeting abstract for the SEG and as an article to the Geophysics journal. Finally, conclusions of this work are provided in Chapter 5, along with suggestions for further study.

Table 1.2. Review table for clay modulus

| Theoretical studies  |                         |  |                                |
|--|-------------------------|--|--------------------------------|
| Analysis Method  | Material                | Modulus (GPa)  | Reference                      |
| Self consistent approximation and Differential effective medium                      | clay                    | $C_{11}=34$ ,<br>$C_{33}=22$                               | Hornby <i>et al.</i> (1994)    |
| Density Function Theory  | kaolinite               | $E_{11}=92$ ,<br>$E_{22}=170$ ,<br>$E_{33}=31$             | Sato <i>et al.</i> (2005)      |
| Empirical linear fit with density  | various                 | E=178-265  | Chen & Evans (2006)            |
| Experimental studies   |                         |  |                                |
| Analysis Method  | Material                | Modulus (GPa)  | Reference                      |
| Brillouin Scattering   | muscovite               | $C_{11}=181$ ,<br>$C_{22}=178$ ,<br>$C_{33}=59$            | Vaughan & Guggenheim (1986)    |
| Resonance spectroscopy   | alumina+mullite         | E=222  | Ledbetter <i>et al.</i> (2001) |
| Extrapolation from clay epoxy data   | montmorillonite         | E=50   | Wang <i>et al.</i> (2001)      |
| Atomic Force Acoustic Microscopy   | dickite                 | E=6  | Prasad <i>et al.</i> (2002)    |
| Extrapolation  | various                 | E=14   | Vanorio <i>et al.</i> (2003)   |
| Ultrasonic   | dry kaolinite           | E=0.15   | Vallejo & Lobo-Guerrero (2005) |
| Molecular simulation and hybrid studies  |                         |  |                                |
| Analysis Method  | Material                | Modulus (GPa)  | Reference                      |
| Minimization of misfit between calculated and measured values based on initial guess | polycrystalline mullite | E=225.9  | Palko <i>et al.</i> (2002)     |
| Molecular Dynamics   | montmorillonite         | $C_{11}=255$ ,<br>E=400                                    | Manevitch & Rutledge (2004)    |
| Molecular Dynamics   | pyrophyllite            | Interlayer<br>E=13.18,<br>Two-layer<br>clay unit<br>E=54.6 | Katti <i>et al.</i> (2005b)    |

*E* represents Young's moduli and *C* represents elastic tensor values.

## Chapter 2

### MOLECULAR SIMULATION

#### 2.1 Summary

The swelling of clays with increasing water under stress has wide ranging impacts, yet it is still poorly understood. We performed molecular simulation on montmorillonite, with varying amounts of water content in the interlayer under different stress conditions. Our analyses of the molecular structure of montmorillonite at various stresses and hydration states show that swelling behaves in a non-linear way with stress. Young's modulus for Na-montmorillonite interlayer varies from 5 GPa to 16 GPa. Steps occur in the Young's modulus profile with the formation of new water layers, but they subsequently become smaller and wider with successive water layers. These changes in modulus can be explained with density variations of the interlayer water, which are related to the arrangement of water molecules.

#### 2.2 Introduction

To unfold the mysteries of clay minerals, it is best to start at the atomic level, hence we adopted the molecular modeling approach. Molecular modeling comprises a broad range of computer methods which allow chemists to display molecules, predict their structures, make short movies of their motions, and predict how they bind to and react with each other. Most computer simulations are based on the assumption

that classical mechanics can be used to describe the motion of atoms and molecules. Monte Carlo statistical mechanics (MC) is one of the methods for atomic-level modeling of fluids. The system set up includes representation of molecules as collections of atom-centered interaction sites, utilization of classical force fields for the potential energy terms, and implementation of periodic boundary conditions (Allen & Tildesley, 1987; Frenkel & Smit, 2002). A new configuration is generated by selecting a random molecule, translating it, rotating it, and performing any internal structural variations. Acceptance of the new configuration is determined by the Metropolis sampling algorithm (Metropolis *et al.*, 1953); application over enough configurations yields properly weighted averages for structure and thermodynamic properties. The basic assumption of statistical mechanics is that a system with fixed number of particles, volume and energy is likely to be found in any of its eigenstates. The challenge in geometry optimization that follows from the basic assumption is finding the most stable structure, the global minimum. Molecules adopt many stable structures or local minima, which differ by rotations about single bonds. Moreover, molecular mechanics has limitations in accurately modeling all chemical reactions.

## 2.3 Literature Review

The review tables (Table 2.1 and Table 2.2) give an overview of the current state of the art with respect to the hydration of clay minerals from early theoretical, experimental and molecular simulation studies.

Early studies (Nagelschmidt, 1936; Bradley *et al.*, 1937) indicated a continuous variation of  $d(001)$  (interlayer spacing) with available water or relative humidity. Other workers (Mooney *et al.*, 1952) asserted that  $d(001)$  changed discontinuously.

Moore & Hower (1986) showed that for Na-smectite the variation is continuous but not linear. The change in apparent  $d(001)$  results from an ordered interstratification of continuously changing proportions of successive hydrates; i.e., as relative humidity is increased from 0 to 100%. The simulations (Karaborni *et al.*, 1996) showed that the abundant clay mineral has four stable states at basal spacings of 9.7, 12.0, 15.5, and 18.3 Å, respectively. The value 2.8 Å is taken to correspond to the thickness of one layer of water.

Chilingar & Knight (1960) conducted high pressure compaction studies ( up to 200,000 psi) and plotted the remaining moisture content in percent (dry weight) versus the logarithm of pressure. For montmorillonite, they observed a break in the curve at about 1000 psi, and from 1000 to 200,000 psi the curve is a straight line and its slope is steeper than that of kaolinite or illite. Up to 1000 psi, free liquid water is squeezed out, whereas at higher pressures up to 200000 psi, oriented water is being removed.

Colten-Bradley (1987) observed that at  $25^{\circ}C(77^{\circ}F)$ , loss of water in excess of two water layers may be affected at loading pressures of 186-634 bars (2700-9200 psi) for interlayer water densities of 1.04-1.15 g/cc. Loss of the second and first water layers may be affected at pressures of 310-1034 bars (4500-15000 psi) and 1517-5241 bars (22000-76000 psi), respectively. At  $61^{\circ}C - 81^{\circ}C(153^{\circ}F - 178^{\circ}F)$  and  $172^{\circ}C - 192^{\circ}C(342^{\circ}F - 378^{\circ}F)$ , no applied pressure is necessary to affect the loss of the second and first water layers, respectively. Conditions for the second water layer correspond to those associated with the onset of smectite-illite transformation and hydrocarbon generation.

Skipper *et al.* (1991, 1995a,b); Boek *et al.* (1995); Sposito *et al.* (1999b); Park & Sposito (2003) initiated the computer simulation studies of molecular interactions

between interlayer water and 2:1 clays. Teppen *et al.* (1997) refined the potential energy parameters by using isothermal-isobaric molecular dynamics simulations of quartz, gibbsite, kaolinite, and pyrophyllite.

Laird (1999) proposed a model for the hydration of expandable 2:1 phyllosilicates. The model assumes that interlayer volume controls interlayer hydration and that the number of cation/charge sites on external surfaces controls hydration of external surfaces.

Tamura *et al.* (2000) studied stepwise hydration (at intervals of 20% relative humidity (RH) from 0% RH to 95% RH, at a fixed temperature of 30°C) of high-quality synthetic smectite with various cations. Komadel *et al.* (2002) showed that hydration of reduced-charge montmorillonite is not dependent on the layer charge up to 73% cation exchange capacity (CEC) but, after that, the water content retained was so less that hydration was independent of RH. Likos & Lu (2002) measured the vapor desorption isotherms for the kaolinite-smectite mixtures at 24°C for RH ranging from 95% to 0%. Their results showed that the amount of water adsorbed by the clay mixtures at a given RH increases systematically with increasing smectite content. Derivative analysis of the sorption isotherms showed evidence of transitions between 2, 1 and 0 layer hydrate states for the smectite-rich mixtures. The transitions became less apparent as the smectite content decreased. Zaidan *et al.* (2003) simulated a wide range of interlayer water content (0 mg  $H_2O$ /g clay - 260 mg  $H_2O$ /g clay) using Monte Carlo (MC) and Molecular Dynamic (MD) simulations. The simulation results for the two-layer hydrate of uranyl-montmorillonite yielded a water content of 160 mg  $H_2O$ /g clay and a layer spacing of 14.66 Å. Logsdon & Laird (2004) saturated four smectites with Ca, Mg, Na or K and equilibrated at four relative humidities ranging from 56% to 99%. Their results indicate that interlayer water in smectites contributes

to the electrical conductivity of hydrated smectites.

Komadel *et al.* (2002) and Tambach *et al.* (2004) observed hysteresis in clay swelling. Grygar *et al.* (2005) characterized expandable clay minerals in Lake Baikal sediments by thermal dehydration (with  $5^{\circ}\text{C}$  steps between  $25^{\circ}\text{C}$  and  $250^{\circ}\text{C}$ ). Liu & Lin (2005) derived a complete description of the dehydration relationships among swelling pressure, basal spacing and ratio of mass of water to clay (mw/mc) in a Na-smectite water system at  $25^{\circ}\text{C}$  under variable pressure conditions. The hydration state, or the amount of interlayer water, is a function of the extent and location of the 2:1 layer charge, the interlayer cation species, the vapor pressure, the temperature and the salinity of associated water.

Extensive modeling and experimental research show that hydration of swelling clays non-uniformly increases their basal spacing (Mooney *et al.*, 1952; Skipper *et al.*, 1995a; Karaborni *et al.*, 1996). Although there has been a lot of work done on hydration studies of swelling clays, most studies either do not report stress (Karaborni *et al.*, 1996; Tamura *et al.*, 2000; Komadel *et al.*, 2002; Grygar *et al.*, 2005) or report constant stress (Skipper *et al.*, 1991; Zaidan *et al.*, 2003; de Pablo *et al.*, 2004; Likos & Lu, 2006) or very small changes in stress (Chilingar & Knight, 1960; Colten-Bradley, 1987; de Pablo *et al.*, 2004; Tambach *et al.*, 2004; Katti *et al.*, 2005a,b). Katti *et al.* (2005a,b) observed that under applied loading, deformation occurs mainly in the interlayer and that the relationship between stress and displacement of the interlayer is linear. Until now, the few studies that have reported swelling of clays under stress have a sparse distribution in the stress domain. It is difficult to understand and comprehend the complex behavior of clays from such data. A comprehensive understanding of the interplay between elastic properties of clays, water content and stress is our goal.

Table 2.1. Review table for clay hydration from early theoretical and experimental studies

| System Chem-<br>istry                         | Inter<br>layer<br><br>Cation   | Temp<br><br>(K)       | Stress<br><br>(Pa)            | Relative<br>humid-<br>ity/Water<br>(%) | Basal<br>Spacing<br>(Å) | Reference                       |
|---|--|-----------------------|-------------------------------|--|-------------------------|---------------------------------|
| Kaolinite, illite,<br>montmorillonite         | -  | -                     | 0.27-<br>1379*10 <sup>6</sup> | 0-100                                  | -                       | Chilingar<br>& Knight<br>(1960) |
| Smectite                                      | Na <sup>+</sup>  | 298.15<br>-<br>465.15 | 0-<br>524.1*10 <sup>6</sup>   | 0-2 layer                              | -                       | Colten-<br>Bradley<br>(1987)    |
| Synthetic smec-<br>tite                       | Mg <sup>2+</sup> ,<br>Ca <sup>2+</sup> ,<br>Na <sup>+</sup> ,<br>Li <sup>+</sup> ,<br>K <sup>+</sup> | 303.15                | -                             | 0-90                                   | 9.9-18.6                | Tamura<br><i>et al.</i> (2000)  |
| Natural mont-<br>morillonite                  | Li <sup>+</sup> with<br>vary-<br>ing<br>CEC  | 110-<br>300           | -                             | 0-100                                  | 9.6-15                  | Komadel<br><i>et al.</i> (2002) |
| Natural smec-<br>tites                        | Mg <sup>2+</sup> ,<br>Ca <sup>2+</sup> ,<br>Na <sup>+</sup>  | 25-<br>250            | -                             | 0-2 layer                              | 10-15                   | Grygar <i>et al.</i><br>(2005)  |
| Smectite<br>12.7nm crystal-<br>lite thickness | Na <sup>+</sup>  | 297.15                | 0                             | 2.6-84.7*                              | 9.7-15                  | Likos & Lu<br>(2006)            |
|   | Na <sup>+</sup>  | 297.15                | 0                             | 76.9-11**                              | 15-11                   | ”                               |
| Smectite<br>11.1nm crystal-<br>lite thickness | Ca <sup>2+</sup>   | 297.15                | 0                             | 2.9-84.1*                              | 12.8-<br>15.5           | ”                               |
|   | Ca <sup>2+</sup>   | 297.15                | 0                             | 77.3-<br>37.3**                        | 15.5-<br>15.5           | ”                               |

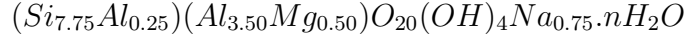
\*Hydration \*\*Dehydration

## 2.4 Simulation Method

The simulations were conducted on the high performance cluster at Advanced Scientific Computation Center, Northeastern University and the supercomputer clus-



ter at the Materials Science Department, Colorado School of Mines. A Fortran 90 program from the Materials Science department was modified for running the molecular simulation of the clay-water systems. We performed an equilibrium study using the Metropolis-based Monte Carlo method on Wyoming type montmorillonite, as it is the most commonly found and examined natural montmorillonite. It belongs to the dioctahedral smectite group (Table 1.1) and the unit cell has the chemical formula (Newman, 1987)



This unit cell has a charge of -0.75, 33% of which is in the tetrahedral sheet. The coordinates for the unit cell are based on those given by Skipper *et al.* (1995a). The starting structure has a unit-cell of dimensions  $5.28 \times 9.14 \times 6.56 \text{ \AA}$ . Our simulation model is inspired from Katti *et al.* (2005b), where two clay layers are considered, each containing four unit-cells in the X direction and two unit-cells in the Y direction as shown in Figure 2.1. There are 4 Mg atoms in the octahedral layer, 2 Al atoms in the tetrahedral layer and 6 Na ions in the interlayer of each clay layer.

The Matsuoka, Clementi and Yoshimine (MCY)(Matsouka *et al.*, 1976) model for the interaction between two water molecules has been used in this work and it has the following functional form for potential energy,  $V(r_{ij})$  :

$$V(r_{ij}) = -A_{ij}e^{-B_{ij}r_{ij}} + C_{ij}e^{-D_{ij}r_{ij}} + \frac{q_i q_j}{r_{ij}}, \quad (2.1)$$

where  $A_{ij}$ ,  $B_{ij}$ ,  $C_{ij}$  and  $D_{ij}$  (Table 2.3) describe the interactions between a particular pair of sites  $i$  and  $j$ ,  $q_i$  and  $q_j$  are the effective charges on a site and  $r_{ij}$  is the intermolecular site separation. The first term represents the attractive London or dispersion forces (Van der Waals forces), the second term represents the short range

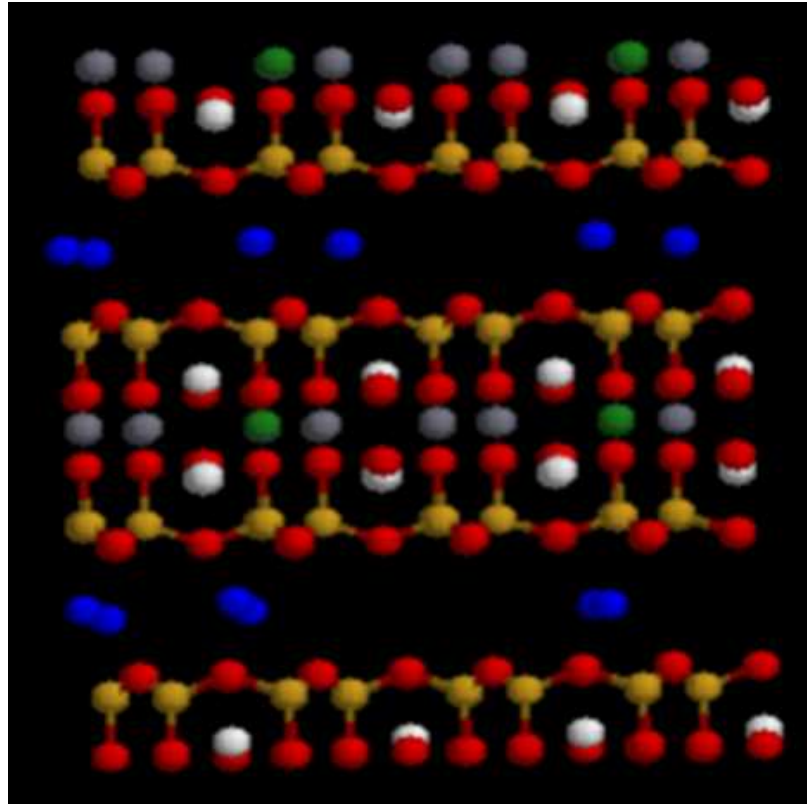


Figure 2.1. The stable structure from simulation run with no water molecules in the interlayer and a uniaxial stress of 1 Pa applied normal to the clay layers. The simulation model consists of two clay layers, each containing four unit-cells in the X direction and two unit-cells in the Y direction. Here the structure is shown in the X-Z plane. Equilibrium basal spacing (thickness of the clay layer and interlayer) of 10.323 Å was obtained. Gold represents *Si* atoms, white:*H*, red:*O*, green:*Mg*, blue:*Na* and grey:*Al*.

repulsions and the third term is the Coulomb force between charged sites. Skipper *et al.* (1995a) found that the MCY model is advantageous for modeling hydrated clay systems over the other most widely adopted and successful TIP4P form (Jorgensen *et al.*, 1983), as a large number of molecular configurations were considered to obtain the MCY potential function. The TIP4P model is strictly an empirical potential fitted only to experimental data for bulk liquid water. Therefore, it may not transfer readily

to more constrained water environments, such as those in clay mineral interlayers. The charges,  $q_i$  and  $q_j$  are taken from Teppen *et al.* (1997). The cation-cation interaction is purely ionic, and is modeled as a simple pairwise electrostatic interaction. The clay interaction parameters are from Skipper *et al.* (1991) and Park & Sposito (2003). The uncertainty of the potential functions were tested by comparing the basal spacing from simulations with experimental values. The basal spacing from simulations are at the most 2.7 % (Skipper *et al.*, 1995a) lower than the experimental values, however, the experimental resolution was about 2.5 % (Mooney *et al.*, 1952). de Pablo *et al.* (2004) conducted molecular simulations on Na-montmorillonite with different water contents at reservoir conditions, indicating the validity of the potential functions at higher stress and water contents. All the intermolecular potential functions were assumed to be valid and constant for all stress and water contents considered in this study.

Each of the atoms interact with the others through the effective potential functions described above. Clearly, if this system were to be studied in isolation, edge effects would be important. Periodic boundary conditions, therefore, are imposed so that the simulation cell is repeated infinitely in all directions. Every atom interacts with all other atoms in a cell and with their (infinite number of) periodic images, simulating a three dimensional clay mineral as would occur in nature, not two clay layers in isolation. The potential energy of a configuration of the periodically-repeated system is given by a sum over all atom pairs in the simulation cell and over all of their (infinite number of) periodic images (Equation 2.2):

$$U = \sum_{i=1}^{\infty} \sum_{j=1}^{\infty} V(r_{ij}) \quad (2.2)$$

where  $V(r_{ij})$  is given by Equation 2.1. To make this infinite sum manageable, we apply feasible cut-off distances to the potential energy (Allen & Tildesley, 1987). The choice of cut-off distances leads to an inaccuracy of less than 0.1% in the potential energy calculations (Skipper *et al.*, 1995a). The energy of the initial state is calculated and a chosen atom is moved a small distance ( $dr$ ). To reduce the chance of the atoms getting trapped in a local potential energy minimum, we set the condition  $dr > 0.01\text{\AA}$ . Moves involving a change in the z-dimension of the layer (basal spacing) are also allowed. According to the Metropolis sampling algorithm (Metropolis *et al.*, 1953), if the energy of the resulting state is lower than that of the initial one, the move is accepted with unit probability. Otherwise, the probability of acceptance ( $p$ ) is Equation 2.3 (Allen & Tildesley, 1987):

$$p = e^{\Delta E/k_B T} \quad (2.3)$$

if  $\Delta E < 0$ , where

$$\Delta E \equiv U_1 - U_2 - P\Delta V + Nk_B T \ln(V_1/V_2) \quad (2.4)$$

$k_B$  is the Boltzmann constant,  $U_1$  and  $U_2$  are the initial and final potential energies,  $N$  is the total number of atoms,  $P$  is the uniaxial stress,  $T$  is the temperature,  $V_1$  and  $V_2$  are the initial and final volumes and  $\Delta V \equiv V_1 - V_2$ . If the parameter,  $dr$  is too small then a large fraction of moves are accepted and the phase space is explored slowly, i.e. consecutive states are highly correlated. If  $dr$  is too large then nearly all the trial moves are rejected and again there is little movement through the phase space. So  $dr$  was adjusted during the simulation so that about half the trial moves

are rejected (Allen & Tildesley, 1987). Skipper *et al.* (1995a) found that increasing the separation between an atom and its nearest self-image had no significant effect on the calculated layer spacing, average potential energy, or the molecular structure.

An isothermal-isobaric ensemble of a system enabled us to study the equilibrium structures at constant temperature, stress and water content. The simulations were made at discrete uniaxial stresses (1 Pa to 10 GPa) applied normal to the clay sheets with varying number of water molecules (0 to 128) in the interlayer at a constant temperature (300 K).

Data were collected for averages after every 5000 attempted moves. The simulations were allowed to proceed till equilibration was reached, which was at least 500,000 moves. Equilibration was judged to have taken place when the average total potential energy of the system and z-dimension of the layer (basal spacing) had reasonably constant values (less than 1.8% variation). Since uniaxial stress was applied normal to the clay sheets and the trial moves were either within the simulation cell or involved a change only in the z-dimension of the layer (basal spacing), compressional modulus ( $M$ ) was calculated from the change in basal spacing with stress. Young's modulus ( $E$ ) was calculated from  $M$  (Equation 2.5):

$$E = \frac{M(1 + \nu)(1 - 2\nu)}{1 - \nu} \quad (2.5)$$

where  $\nu$  is the Poisson's ratio. An example input and raw output files are contained in Appendix A.

## 2.5 Results

The simulations captured equilibrium basal spacing (thickness of the clay layer and the interlayer) of montmorillonite as a function of stress and bound water in the interlayer with a maximum uncertainty of 1.8% (the largest standard deviation value in all the gathered data sets). Our simulated basal spacing at 0.1 MPa and 32 water molecules (12.27 Å) is in close agreement with experimental data (12.2-12.5 Å from Mooney *et al.* (1952)) and previous simulation data (12.1 Å from Skipper *et al.* (1995a)).

The basal spacing increases with increasing water content (Figure 2.2). The interlayer expands as the interlayer cations are attracted more to water than to the relatively small negative clay layer charge (Moore & Reynolds, 1989). At a constant hydration state, the basal spacing decreases with increasing uniaxial stress. This also implies that the clays de-water with increasing stresses, and can lead to over pressured zones in the earth. The simulated hydration induced expansion in montmorillonite under stress exhibits a separation in deformation behavior at about 1 MPa. Below 1 MPa (domain A), basal spacing changes with stress are of the order of uncertainty in simulation data. Stress can be ignored as a factor in the swelling of clays for shallow depths ( $\sim 100$  m)(Boek *et al.*, 1995). Between 1 MPa - 10 GPa (domain B), which encompasses deeper burial and the subduction zone, basal spacing shows maximum sensitivity to stress. The effect of stress also increases with higher water contents in domain B. The non-linear trend of basal spacing with stress at higher water contents is similar to the volume changes of water with pressure (Bowers, 1995). The relationship between applied stress and displacement of the interlayer is highly non-linear, in contrast to the linear behavior in pyrophyllite (Katti *et al.*, 2005b). This

difference occurs due to the interaction between the clay layers and the interlayer water and cations, that are absent in uncharged pyrophyllite (Table 1.1).

This study establishes that the swelling behavior of clays under stress cannot be simply explained by bulk liquid water properties, but is an intricate interplay of the siloxane surface, cation solvation effects and stress on the interlayer water. To investigate the interplay of the clay layers and cations with interlayer water, the simulated partial radial distribution functions (RDF) of the interlayer water molecules were compared with experimental results published by Soper *et al.* (1997), who studied bulk liquid water by isotope-difference neutron diffraction of  $D_2O/H_2O$  mixtures. Molecular mechanisms underlying the structural differences can be interpreted from the partial RDFs for H-O ( $g_{HO}(r)$ ), H-H ( $g_{HH}(r)$ ) and O-O ( $g_{OO}(r)$ ) spatial correlations (Sposito *et al.*, 1999a) as functions of water content (Figure 2.3) and stress (Figure 2.4). Partial RDFs in bulk water indicate the relative placement of water molecules about a reference molecule, with the first peak indicating the nearest neighbor position and the second, the position of next nearest neighbors and so on.

The partial radial distribution function  $g_{\alpha\beta}(r)$  is defined implicitly by the Equation 2.6 (Enderby & Neilson, 1981):

$$dn_{\alpha\beta} = 4\pi \frac{N_{\beta}}{V} g_{\alpha\beta}(r) r^2 dr \quad (2.6)$$

where,  $dn_{\alpha\beta}$  is the average number of  $\beta$ -species atoms within a spherical shell of radius  $r$  and thickness  $dr$  enclosing an  $\alpha$ -species atom which has been placed at  $r = 0$ , and  $N_{\beta}$  is the total number of  $\beta$  atoms in the system of volume  $V$ . Thus,  $g_{\alpha\beta}(r)$  is the relative probability that a  $\beta$  atom resides within  $dr$  at a radial distance  $r$  from an  $\alpha$  atom centered at the origin of coordinates (Allen & Tildesley, 1987).

The partial RDFs for H-H, O-O and H-O with increasing water contents in the interlayer show better defined peaks resembling that of bulk liquid water (Figure 2.3). However, the organization of the interlayer water molecules is significantly different from the local tetrahedral coordination that is characteristic of bulk liquid water. For example, strong H-O spatial correlations in interlayer water extend over greater distances than in liquid water, as the broad third neighbor peak near 5.4 Å for 128 water molecules is not seen in liquid water. The first peak in  $g_{HO}(r)$  and both first and second peaks in  $g_{HH}(r)$  are shifted to larger distances ( $r$ ) than in bulk water, indicating longer hydrogen bonds. Also, the second neighbor peak in  $g_{OO}(r)$  near 4.3 Å in bulk liquid is not clearly visible in interlayer water. Boek *et al.* (1995) noted that water molecules were organized primarily to accommodate the solvation requirements of  $\text{Na}^+$  cations bound in the clay mineral interlayer. Karaborni *et al.* (1996) commented that water protons were also attracted to surface oxygen ions near tetrahedral charge sites on the clay mineral to form hydrogen bonds whereas the oxygen atoms in water were attracted to the protons in the structural OH groups in the cavities of the clay mineral surface. This competition for adsorbed water molecules among the interlayer cations, surface oxygen ions and OH protons in the clay mineral surface would tend to disrupt the local tetrahedral coordination among water molecules that characterizes the bulk liquid.

The organization of the interlayer water molecules is disrupted with increasing uniaxial stresses, as indicated by the diminishing of the broad second peak in  $g_{OO}(r)$ , faintly visible for 1 Pa around 4.3 Å and the broadening of the third peak in  $g_{HO}(r)$  for 1 Pa at 5 Å (Figure 2.4). Spatial correlations exist over shorter distances, implying shorter hydrogen bonds at higher stresses. It is indicated by the shift of the second peak in  $g_{HO}(r)$  and both primary and secondary peaks in  $g_{HH}(r)$  towards lower  $r$



values, thus deviating from the bulk liquid behavior. The tenacity of the molecular structure of clays in the unexplored regions of the phase space are evident from our simulations.

The equilibrium structures under stress gave the elastic modulus of the interlayer. The clay layers were kept stiff in the simulation model, since most of the deformation occurs in the interlayer (Katti *et al.*, 2005b). Young's modulus was calculated assuming a constant Poisson's ratio ( $\nu$ ) of 0.144 (Woeber *et al.*, 1963) in Equation 2.5. The magnitude of the calculated Young's modulus will vary due to this constant value (16 GPa for  $\nu=0.11$  to 2 GPa for  $\nu=0.48$ ), but the behavior with water content and stress will remain the same. Young's modulus for Na-montmorillonite interlayer varies between 5 GPa to 16 GPa for varying amounts of water and stress. Figure 2.5 shows that Young's modulus increases as we move to the first water layer ( $\sim 32$  water molecules) from the dry state (interlayers with  $\text{Na}^+$  cations only). It drops after the first water layer formation is complete and then increases a bit again till 64 water molecules, which is the second water layer and so on. Thus, steps occur with the start of new water layers, but they subsequently become smaller and wider with successive water layers.

The elastic moduli are often expected to be proportional to density (Chen & Evans, 2006). The changes in modulus can be explained with density variations (Music *et al.*, 2003). The density  $\rho(N)$  of the interlayer water was calculated as a function of water content (Equation 2.7).

$$\rho(N) = \frac{Nm_{H_2O}}{V(N) - V(0)} \quad (2.7)$$

Here  $V(N) - V(0)$  is the volume difference between a montmorillonite containing N

water molecules and the anhydrous one and  $m_{H_2O}$  is the mass of a water molecule. Figure 2.6 shows that the density increases until the first water layer is completed ( $\sim 48$  water molecules). At this hydration stage, the water molecules are oriented coplanar with the clay layer (Boek *et al.*, 1995). The density then drops as the water molecules are more diffusely arranged in the interlayer at the beginning of the formation of the second layer. The density increases a bit again until the second water layer is completed. This sequence of steps repeats over successive water layers and they become smaller and broader due to the development of diffused ion swarm (Boek *et al.*, 1995). Similar trends are found for all the stresses: steps appear in the density profile with the start of new water layers. It may be expected that the density asymptotically approaches the bulk water density for higher water contents. And then the Young's modulus will also approach to that of bulk water.

## 2.6 Conclusions

Swelling in montmorillonite increases with water content in the interlayer and decreases with higher stress values. Our analyses of the molecular structure of montmorillonite at various stresses and hydration states show that swelling behaves nonlinearly with stress. This study establishes that the swelling behavior of clays under stress cannot be simply explained by bulk liquid water properties, but is an intricate interplay of the siloxane surface, cation solvation effects and stress on the interlayer water. With increase in water content in the interlayer, the partial RDFs for H-H, O-O and H-O show better defined peaks, resembling bulk water. However, the organization of the interlayer water molecules is significantly different from the local tetrahedral coordination that is characteristic of bulk liquid water. The organization

of the interlayer water molecules is disrupted with increasing uniaxial stresses.

Young's modulus for Na-montmorillonite interlayer varies between 5 GPa to 16 GPa. This is a significantly narrower range than the 0.15 GPa to 400 GPa range, previously reported in the literature. Steps occur in Young's modulus profile with the start of new water layers, but they subsequently become smaller and wider with successive water layers. These changes in modulus can be explained with density variations of the interlayer water, which are related to the arrangement of water molecules.

Table 2.2. Review table for clay hydration from molecular simulation

| System Chem-<br>istry  | Interlayer<br><br>Cation | Temp<br><br>(K) | Stress<br><br>(Pa)                                | Relative<br>humid-<br>ity/Water<br>(%)        | Basal<br>Spacing<br>(Å) | Reference                            |
|--|--------------------------|-----------------|---|---|-------------------------|--------------------------------------|
| Montmorillonite:<br>2 clay layers,<br>3.44 Å ini-<br>tial interlayer<br>spacing                      | Mg <sup>2+</sup>         | 300             | 10 <sup>6</sup>                                   | 0-(50-75)                                     | 11.1-14.7               | Skipper<br><i>et al.</i><br>(1991)   |
|  | Na <sup>+</sup>          | 300             | 10 <sup>6</sup>                                   | 0-(50-75)                                     | 9.8-14.2                | ”                                    |
| Montmorillonite  | Na <sup>+</sup>          | -               | -   | 0-3 lay-<br>ers                               | 9.7-18.3                | Karaborni<br><i>et al.</i><br>(1996) |
| Montmorillonite  | Uranyl(U)                | 300             | 100*10 <sup>3</sup>                               | 10-90<br>molecules                            | 12.23-<br>16.87         | Zaidan<br><i>et al.</i><br>(2003)    |
| Montmorillonite:<br>2 clay layers,<br>8 unit cells,<br>$NP_{zz}T$ ensem-<br>ble<br>$\mu VT$ ensemble | Na <sup>+</sup>          | 353             | 62.5*10 <sup>6</sup>                              | 32-256<br>per cell                            | 12.57-<br>31.10         | de Pablo<br><i>et al.</i><br>(2004)  |
|  | ”                        | ”               | 991.07-<br>182.45*10 <sup>6</sup><br>( $P_{zz}$ ) | 45.25-<br>160.75<br>per layer                 | 12-20.5                 | ”                                    |
| Montmorillonite  | Na <sup>+</sup>          | 298             | (-0.2)-<br>0.8*10 <sup>6</sup>                    | 25-67   | 12-15                   | Tambach<br><i>et al.</i><br>(2004)   |
| Montmorillonite:<br>2 clay layers  | Na <sup>+</sup>          | 300             | 0-<br>3.11*10 <sup>9</sup>                        | 0-96<br>molecules<br>(0-3<br>mono-<br>layers) | 10.8-15.5               | Katti <i>et al.</i><br>(2005a)       |
| Pyrophyllite: 2<br>clay layers, 3.44<br>Å initial inter-<br>layer spacing                            | none                     | 300             | 0-<br>1.65*10 <sup>9</sup>                        | 0   | 10.48-<br>9.98          | Katti <i>et al.</i><br>(2005b)       |

*Unit cell dimensions are  $21.12 \times 18.28 \times 6.56 \text{Å}$  for all simulation studies tabulated above*

Table 2.3. Parameters in the MCY potential function (Skipper *et al.*, 1995a).

| $i - j$ | $A_{ij}(\text{kcal/mole})$ | $B_{ij}(\text{\AA}^{-1})$ | $C_{ij}(\text{kcal/mole})$ | $D_{ij}(\text{\AA}^{-1})$ |
|---------|----------------------------|---------------------------|----------------------------|---------------------------|
| H-H     | 0.0                        | 0.0                       | 666.33                     | 2.76                      |
| H-O     | 273.59                     | 2.23                      | 1455.4                     | 2.96                      |
| O-O     | 0.0                        | 0.0                       | 1088213                    | 5.15                      |
| H-Na    | 884.23                     | 1.93                      | 2051.9                     | 2.36                      |
| O-Na    | 25.95                      | 0.77                      | 61888.0                    | 4.08                      |
| H-Si    | 2.14                       | 1.22                      | 577.23                     | 2.16                      |
| H-Al    | 2.14                       | 1.22                      | 577.23                     | 2.16                      |
| O-Si    | 1345.8                     | 2.26                      | 13061                      | 3.2                       |
| O-Al    | 1345.8                     | 2.26                      | 13061                      | 3.2                       |
| Si-Na   | 1505.4                     | 1.86                      | 2164.54                    | 2.12                      |
| Al-Na   | 1505.4                     | 1.86                      | 2164.54                    | 2.12                      |

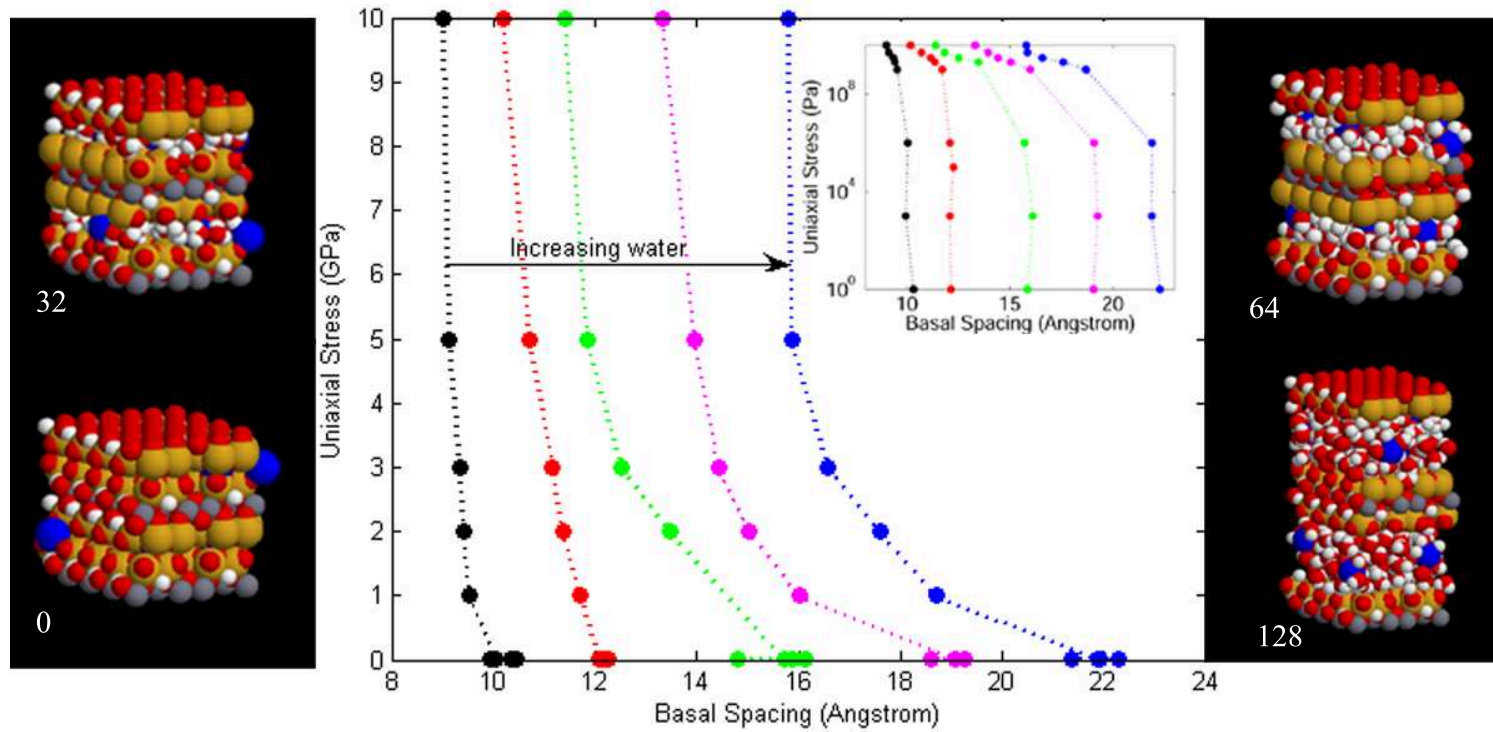


Figure 2.2. Hydration induced expansion in montmorillonite under stress. Effects of uniaxial stress, applied normal to the clay sheets, on basal spacing are shown with varying number of water molecules in the interlayer. The inset shows the same data with the stress plotted in logarithmic scale. Black represents 0 water molecules, red:32, green:64, magenta:96 and blue:128. Surrounding the plot, are the stable state structures obtained from our simulation runs for 0, 32, 64 and 128 water molecules in the interlayer at 1 GPa uniaxial stress. The simulation model consists of two clay layers, each containing four unit-cells in the X direction and two unit-cells in the Y direction. Gold represents *Si* atoms, white:*H*, red:*O*, green:*Mg*, blue:*Na* and grey:*Al*. Swelling increases with water content and decreases with uniaxial stress. At a constant hydration state, basal spacing changes are insignificant below 1 MPa; between 1 MPa and 10 GPa, it is effected by stress in a non-linear way.

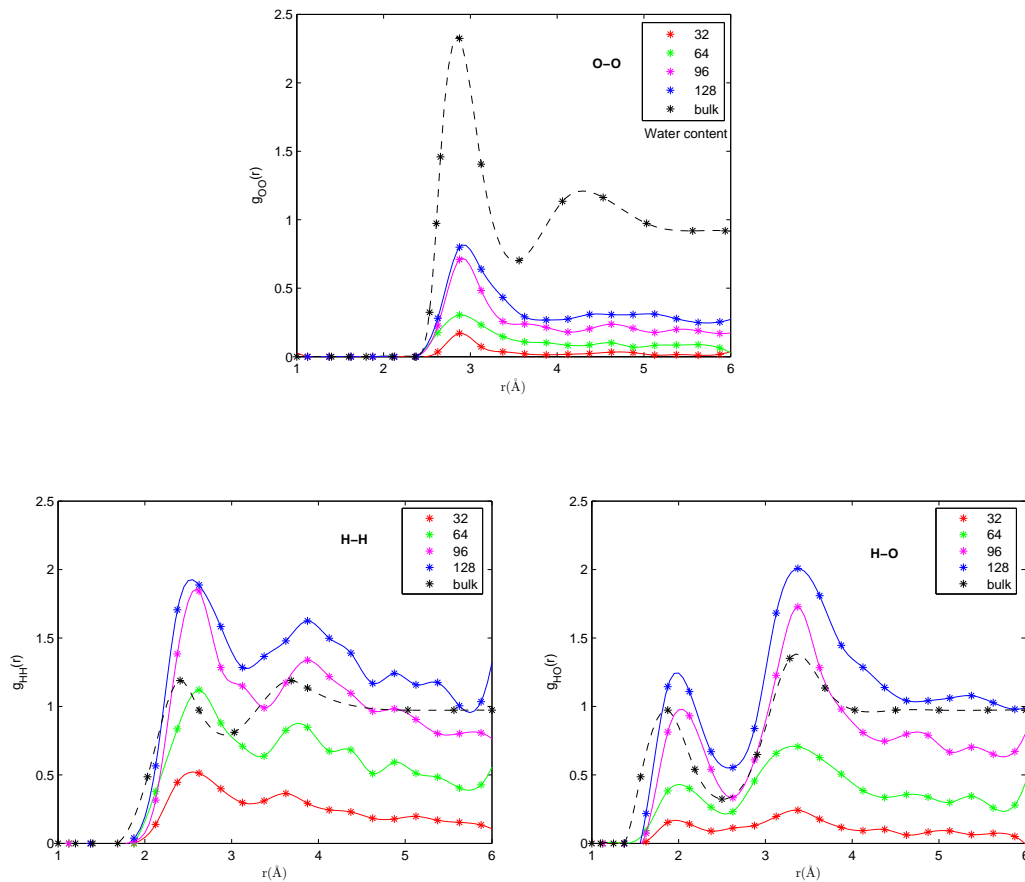


Figure 2.3. Simulated partial radial distribution functions (RDF) with varying water content for hydrated Na montmorillonite (solid lines), and for bulk water from neutron diffraction data (Soper *et al.*, 1997) (dashed lines). Partial RDF for spatial correlations ( $g_{ab}(r)$ ) are shown between any two atoms  $a$  and  $b$ . All the partial RDFs shown here correspond to a constant stress of 0.1 MPa. Partial RDFs for montmorillonite with 32, 64, 96 and 128 water molecules in the interlayer are shown for comparison. With increase in water content in the interlayer, the partial RDFs for H-H, O-O and H-O show better defined peaks. However, the organization of the interlayer water molecules is significantly different from the local tetrahedral coordination that is characteristic of bulk liquid water.

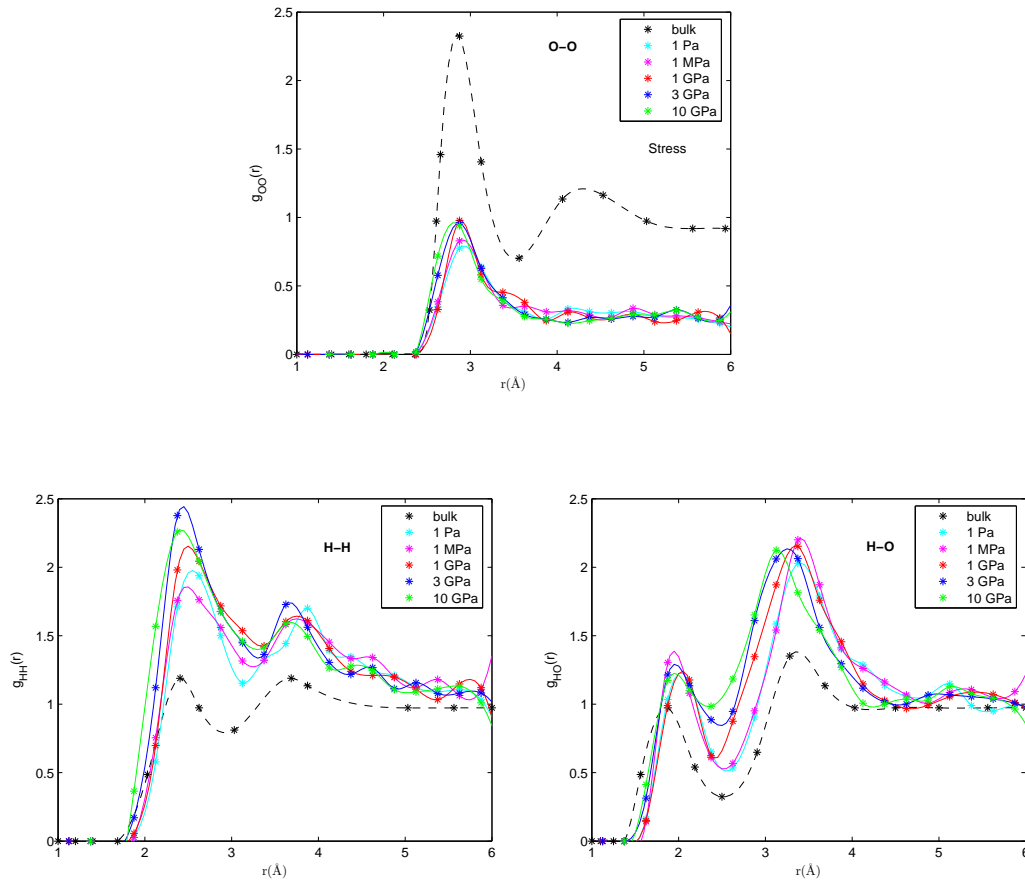


Figure 2.4. Simulated partial radial distribution functions (RDF) with varying stress for hydrated Na montmorillonite as calculated by simulations (solid lines), and for bulk water from neutron diffraction data (Soper *et al.*, 1997) (dashed lines). Partial RDF for spatial correlations ( $g_{ab}(r)$ ) are shown between any two atoms a and b. Partial RDF for bulk water correspond to a stress of 0.1 MPa. The partial RDFs for montmorillonite correspond to a constant 128 water molecules in the interlayer and uniaxial stress of 1 Pa, 1 MPa, 1 GPa, 3 GPa and 10 GPa. With increasing uniaxial stress, the organization of the interlayer water molecules is disrupted.



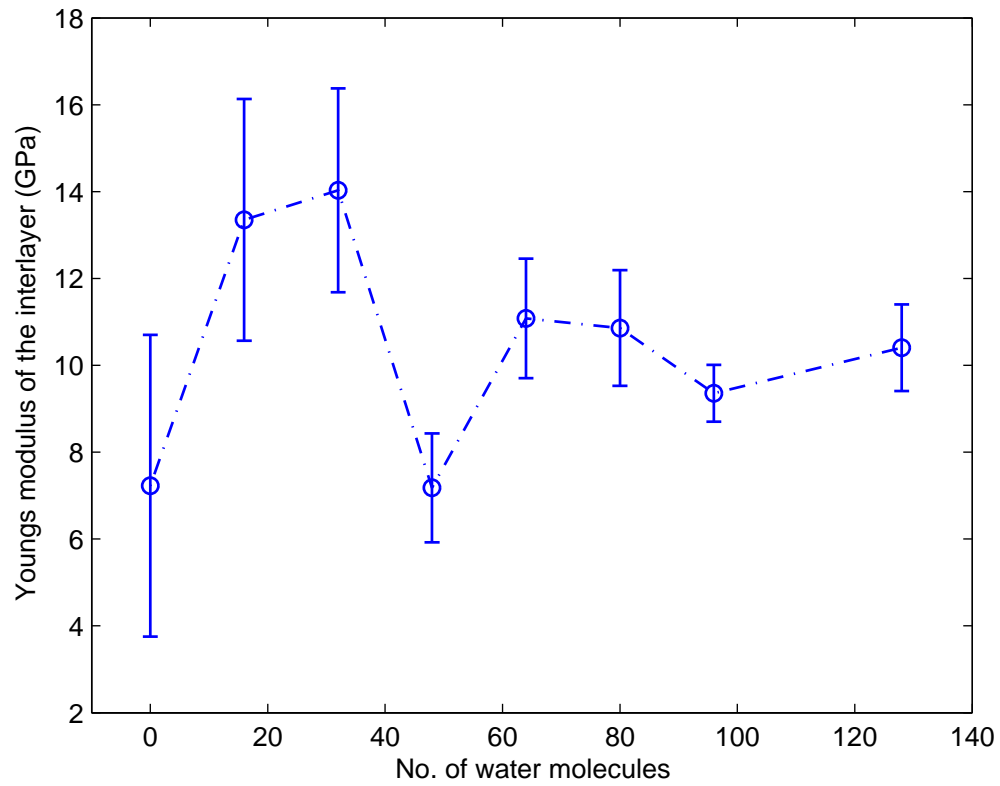


Figure 2.5. Young's modulus of the interlayer as a function of water molecules for a uniaxial stress difference of 1 GPa. The errorbars are due to propagation of uncertainty in Young's modulus calculation from basal spacing (directly measured from simulation). Steps occur in Young's modulus profile with the start of new water layers, but they subsequently become smaller and wider with successive water layers.

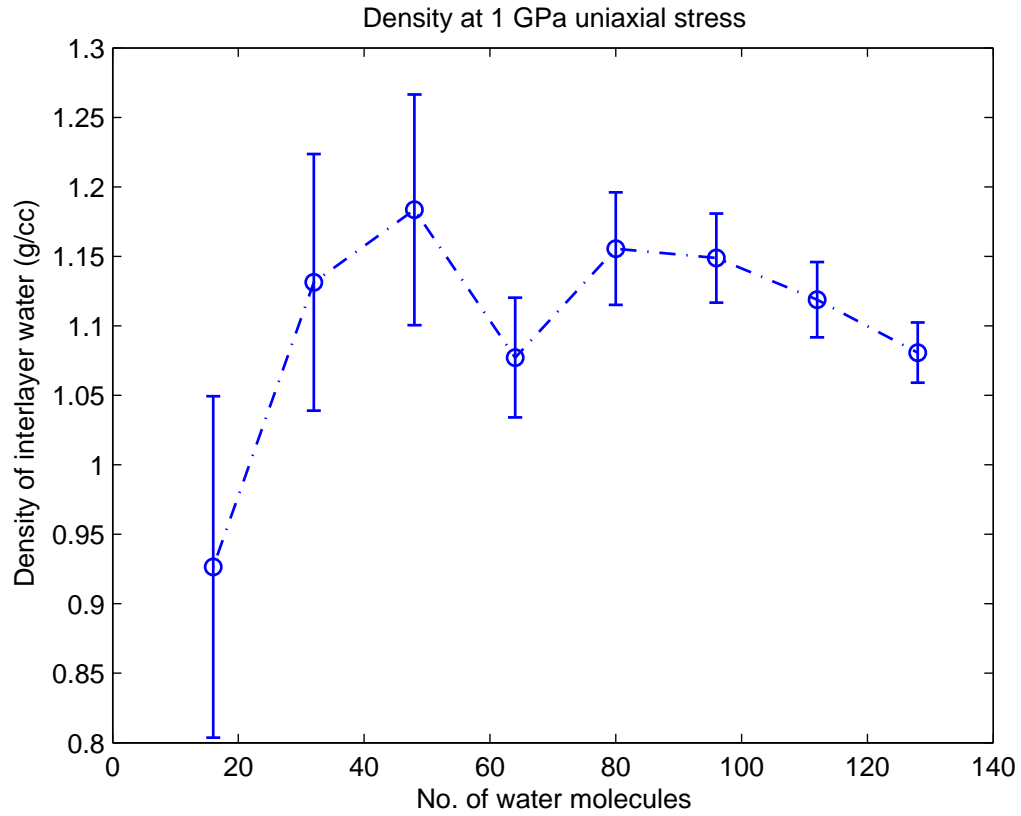


Figure 2.6. Density of the interlayer water as a function of water molecules at a uniaxial stress of 1 GPa. The errorbars are due to propagation of uncertainty in density calculation from basal spacing (directly measured from simulation). Steps occur in the density profile with the start of new water layers and the density gradually converges towards that of bulk water.

## Chapter 3

### NANOINDENTATION

#### 3.1 Summary

Clays are used to enhance polymer properties, but their own properties are poorly understood. In most cases, the elastic modulus of mica is used in the design of advanced polymers as they have a similar structure to clays and direct measurements have been performed on mica.

We developed sample preparation techniques and an analysis method for the nanoindentation measurements that worked very well with clays. The greatest challenge was achieving a good contact between the indenter tip and the clay sample. This was overcome by taking larger grain sizes, a harder mineral and making the surface of the sample as smooth and free of impurities as possible. We measured Young's modulus of kaolinite as 2.59 GPa to 2.6 GPa. Young's modulus of 4 GPa to 14 GPa were obtained for two different types of natural reference montmorillonite (Otay SCa 3 and Wyoming SWy 2) with different water contents.

#### 3.2 Methodology

The elastic moduli of a sample can be determined by investigating the sample's behavior under applied stress. The Nanoindenter XP from MTS (Mechanical Testing and Simulation) Systems is an instrument that uses a magnetic assembly for loading a

sharp diamond indenter into a sample (Figure 3.1). This device directly measures the displacement into the sample with a capacitance gage. The details of the instrument and the following underlying theory are provided in Oliver & Pharr (1992). In addition to load and displacement data, the instrument provides a continuous measurement of the contact stiffness via a superimposed AC signal during loading, which results in a displacement oscillation of specified amplitude and frequency. The continuous stiffness measurement (CSM) option allows continuous measurement of the elastic and plastic response of the material during loading and not just at the point of initial unload. The CSM option is especially useful for evaluating thin films on substrates, as the mechanical properties change as a function of surface penetration. The ratio of the load amplitude,  $P_0$ , to the displacement amplitude,  $h_0$ , is related to the contact stiffness,  $S$ , as shown in Equation 3.1,

$$\frac{P_0}{h_0} = \sqrt{(S + k_s - m\omega^2)^2 + \omega^2 D^2} \quad (3.1)$$

where  $k_s$  is the static spring constant of the leaf springs which hold the center plate in position,  $m$  is the spring mass that includes the weight of the indenter and the load shaft,  $\omega$  is the excitation frequency of the displacement oscillation, and  $D$  is the damping coefficient that depends on the position of the center plate within the gap. The phase angle,  $\phi$ , between the dynamic load and the displacement signals is given by Equation 3.2,

$$\tan\phi = \frac{D\omega}{S + k_s - m\omega^2} \quad (3.2)$$

The general expressions for the reduced modulus,  $E^*$ , is given by Equation 3.3,

$$E^* = S \frac{\sqrt{\pi}}{2\beta\sqrt{A_c}} \quad (3.3)$$

where  $A_c$  is the contact area and  $\beta$  is the geometric constant.  $\beta$  is equal to 1.034 for pyramidal indenters, such as the Berkovich indenter used in all of the experiments. The contact area is quantified with a calibrated indenter area function (Figure 3.2). Fused silica was used for calibrating the variation in contact area with contact depth. Then the Young's modulus of the sample is evaluated using Equation 3.4,

$$E^* = \left\{ \frac{1 - \nu_{sample}^2}{E_{sample}} + \frac{1 - \nu_{indenter}^2}{E_{indenter}} \right\}^{-1} \quad (3.4)$$

where  $E$  represents Young's modulus and  $\nu$  represents Poisson's ratio.

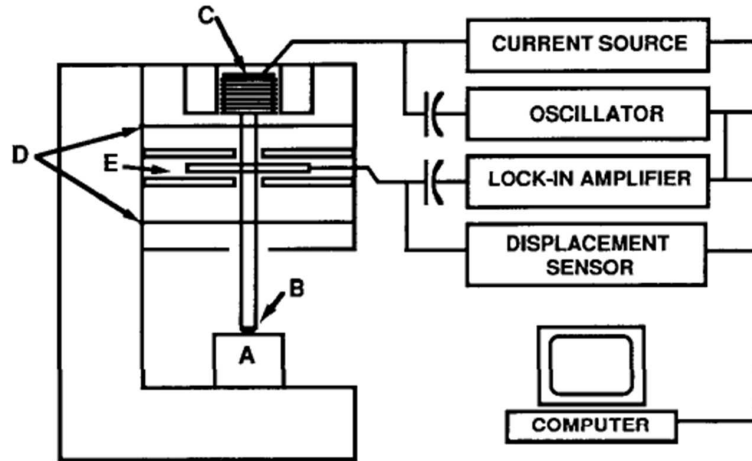


Figure 3.1. A schematic representation of the experimental apparatus used to perform the nanoindentation experiments: (A)sample; (B)indenter; (C)load application coil; (D)indentation column guide springs; and (E)capacitive displacement sensor.

The difficulty in making accurate measurements of the contact area during in-

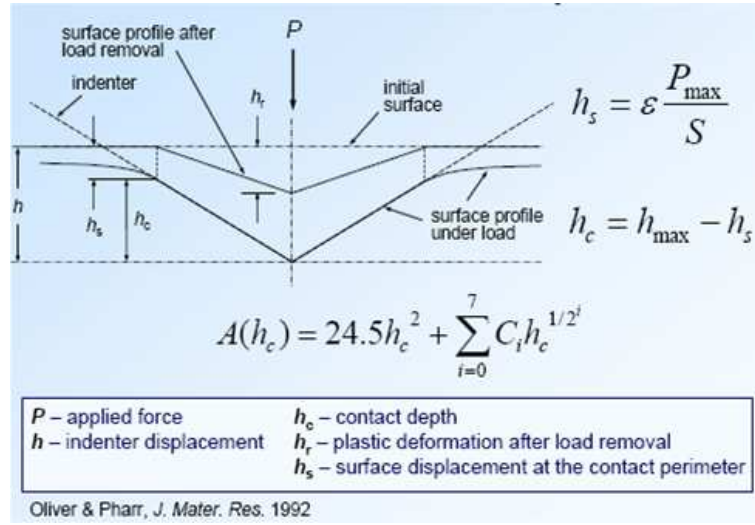


Figure 3.2. Calibration of contact area variation with contact depth (Oliver & Pharr, 1992).

dentation limits the accuracy of data analysis (Figure 3.3) in a significant manner. The tendency of annealed materials to sink-in contributes to an overestimation of contact area calculated from a tip-area function; the tendency of cold-worked materials to pile-up around the indenter causes an underestimation of the contact area. However, assuming elastic homogeneity of the material indented, the contact area can be normalized out of the relative plastic and elastic response (Joslin & Oliver, 1990) as follows. The indentation hardness,  $H$ , is defined as in Equation 3.5,

$$H = \frac{P}{A_c} \quad (3.5)$$

where  $P$  is the load. Dividing the load by the square of the contact stiffness results in an expression independent of the contact area and is therefore a material characteristic (Equation 3.6),

$$\frac{P}{S^2} = \frac{H}{E^{*2}} \frac{\pi}{4\beta^2} \quad (3.6)$$

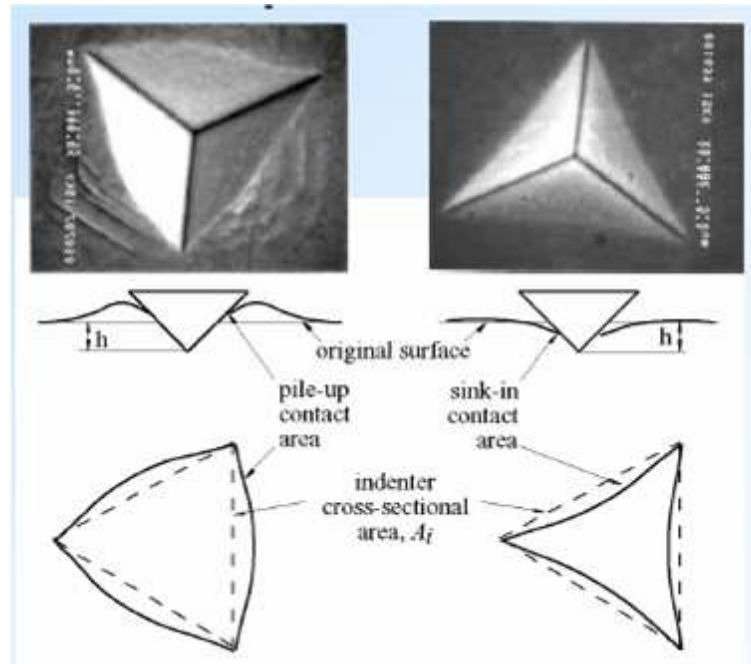


Figure 3.3. Pile-up and sink-in leads to inaccurate contact area measurements (Oliver & Pharr, 1992).

Saha & Nix (2002) examined the effects of the substrate on the determination of mechanical properties of thin films by nanoindentation. By studying both soft films on hard substrates and hard films on soft substrates they were able to assess the effects of elastic and plastic inhomogeneity, as well as material pile-up, on the nanoindentation response. Their study of the material characteristic due to the differences in film and substrate properties allowed us to formulate our sequence for the analysis of clay nanoindentation measurements. First, the load curve with indentation depth is monitored for any discontinuities or plasticity (pop-ins) to avoid analyzing data in the plastic regime. Then the range where the material characteristic is constant with indentation depth is picked. Young's modulus and hardness values are calculated to represent the true material properties in this range.

### 3.3 Sample Characterization

Nanoindentation studies were done on fused silica, glass substrate and muscovite mica, kaolinite (KGa 1b) of different grain sizes, and montmorillonites (SWy 2, SCa 3) deposited on the glass substrate. The clay minerals were obtained from the Source Clays Repository of the Clay Minerals Society. The precise water content was quantified with Thermal Gravimetric Analysis. The samples were characterized further with Scanning Electron Microscope and Optical Profiler.

#### 3.3.1 Sample Preparation

The samples (KGa 1b and SWy 2) in powdered form were first mixed with distilled water and centrifuged to restrict the grain size of the clay minerals. They were then deposited as thin films on glass substrates and left in a covered case for 48 hours to dry. This preparation method forced the clay minerals to align with their c-axis normal to the glass slide. A small and smooth piece of SCa 3 (as received) was chosen and glued directly on a glass substrate.

#### 3.3.2 Scanning Electron Microscope

The orientation of the clay platelets in the clay films was checked with an environmental scanning electron microscope (ESEM). The layered atomic structure of clays leads to anisotropy such as that seen in mica, whose elastic moduli in the perpendicular direction to the c-axis ( $C_{11}$ ,  $C_{22}$ ) is 3.5 times that along the c-axis ( $C_{33}$ ) (Habelitz *et al.*, 1997). Since elastic moduli are dependent on the direction of measurement with respect to the orientation of clay platelets, this study was essential.

Figure 3.4 and Figure 3.5 are ESEM photos of KGa 1b and SWy 2 respectively,



showing that the clay platelets lie flat on the glass slide. ESEM works on low vacuum, so the process does not remove all the absorbed water, which is important for montmorillonite as they always contain water.

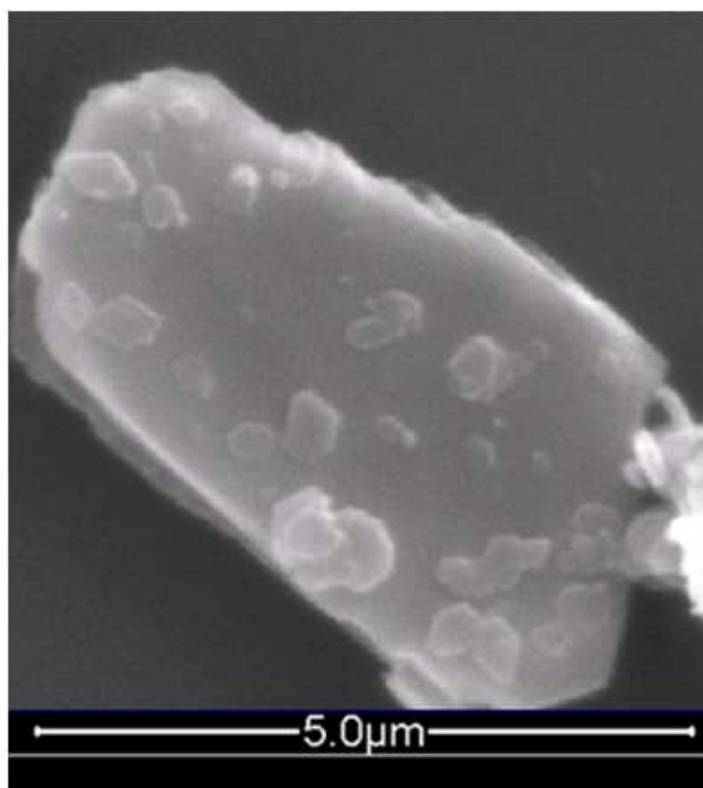


Figure 3.4. Environmental scanning electron microscope graph of kaolinite (KGa 1b) shows the orientation of clay platelets.

### 3.3.3 Thermal Analysis

Water content was measured with thermal gravimetric analysis (TGA) for both the montmorillonites. Montmorillonites can have varied amounts of water attached. One of our goals was to see the changes in the elastic properties with water content, if any. The samples were slowly heated at a constant rate of  $10^{\circ}\text{C}$  per minute, under

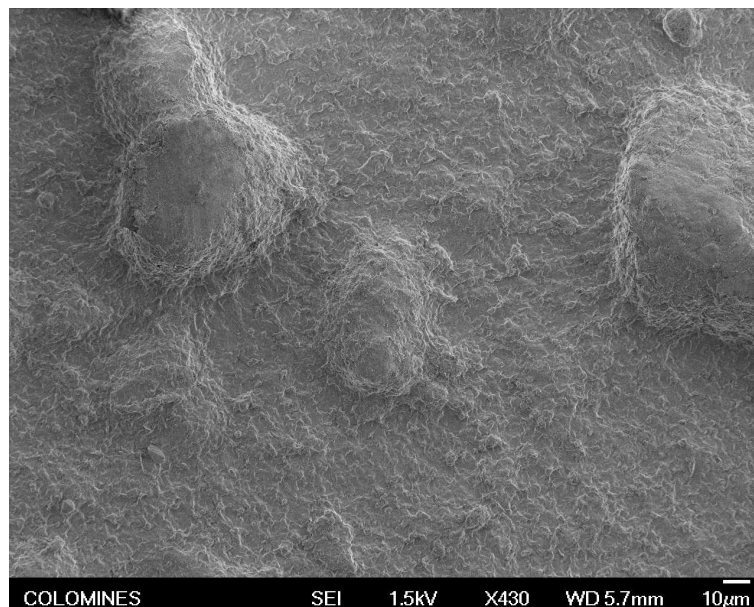


Figure 3.5. Environmental scanning electron microscope graph of montmorillonite (SWy 2) shows the orientation of clay platelets.

helium flow from  $30^{\circ}\text{C}$  to  $800^{\circ}\text{C}$ . The response of materials during thermal analysis is strongly influenced by the humidity surrounding the sample at the time of the experiment. Hence, the atmosphere surrounding the sample was purged with helium. TGA gives the amount of weight lost due to heating. The water content in the samples is found by assuming that all the weight loss is due to the loss of water content. SWy 2 sample (as prepared) had 50% water by weight (Figure 3.6) and SCa 3 sample had 18% (Figure 3.7). 64 water molecules in the interlayer is typically equivalent to 185 mg/g of clay, which is equivalent to 2 water layers (Skipper *et al.*, 1991). The SWy 2 sample had a little less than 5 water layers and the SCa 3 sample had a little less than 2 water layers, as some water resides as free water on the surface of clays. The amount of water in samples is also a function of relative humidity which was not controlled in the nanoindentation experiments. Since both the samples were

kept in the same environment, we can assume that the water lost or absorbed by both samples was equal. This implies that our prepared SWy 2 sample had more interlayer water content than the SCa 3 sample.

The derivative of the TGA curve, the derivative thermal gravimetric analysis (DTG) curve, shows changes in the TGA slope that may not be obvious from the TGA curve. Thus, the DTG curve may show reactions that involve weight and enthalpy changes, such as desorption, dehydration and dehydroxylation reactions. DTG, in green curve, shows two distinct peaks for SCa 3 (as received) (Figure 3.7) and SWy 2 (as received) (Figure 3.8). The first peak spans the interval between  $30^{\circ}\text{C}$  and  $100^{\circ}\text{C}$  in SWy 2 and between  $30^{\circ}\text{C}$  and  $300^{\circ}\text{C}$  in SCa 3. The second peak spans the interval between  $550^{\circ}\text{C}$  and  $750^{\circ}\text{C}$  in both the samples. The first peak represents desorption (free water release) and dehydration (interlayer water release) and the second peak represents dehydroxylation (structural water release) and dehydration (interlayer water release) (Guggenheim & Koster Van Groos, 2001). On heating, there is loss of hydroxyl groups in the presence of water and is called deprotonation of hydroxyl groups or dehydroxylation. The amount of water content in the clay changes the clay structure as seen in molecular simulation and may lead to variations in elastic properties.

### 3.3.4 Optical Profiler

Hardness and elastic modulus profiles determined using the Oliver-Pharr method (Oliver & Pharr, 1992) from the load/unload curves is valid only when a very low degree of asperity is present (lower than 30 nm). If a rough surface is present, errors can occur in determination of the zero tip-surface contact point and, as a consequence, the surface hardness and elastic modulus profiles are drastically altered resulting

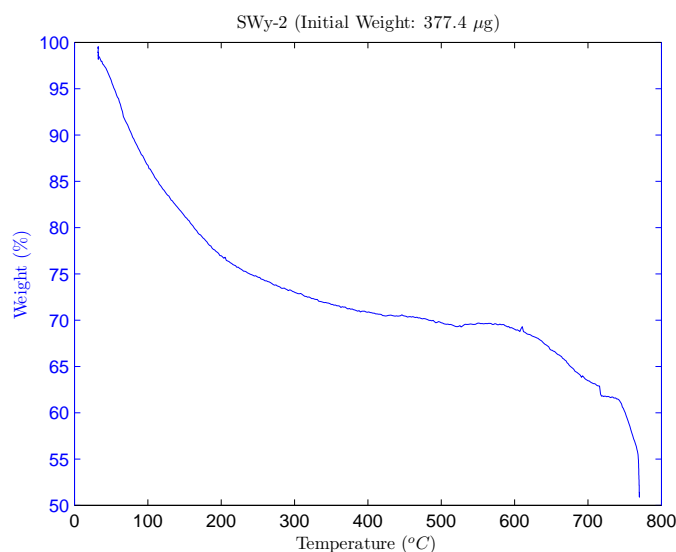


Figure 3.6. Water content in SWy 2 sample (as prepared) was 50% from thermal gravimetric analysis (TGA).

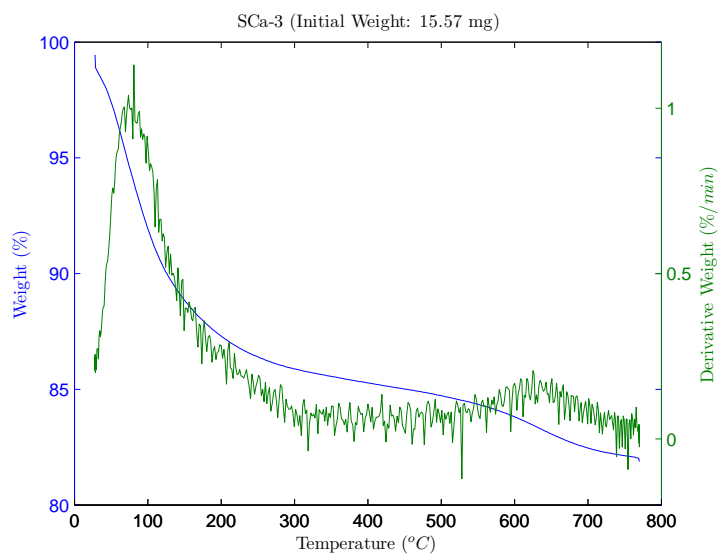


Figure 3.7. Water content in SCa 3 sample (as received) was 18% from thermal gravimetric analysis, TGA, shown in blue. Derivative thermal gravimetric analysis (DTG), in green, shows two distinct peaks.

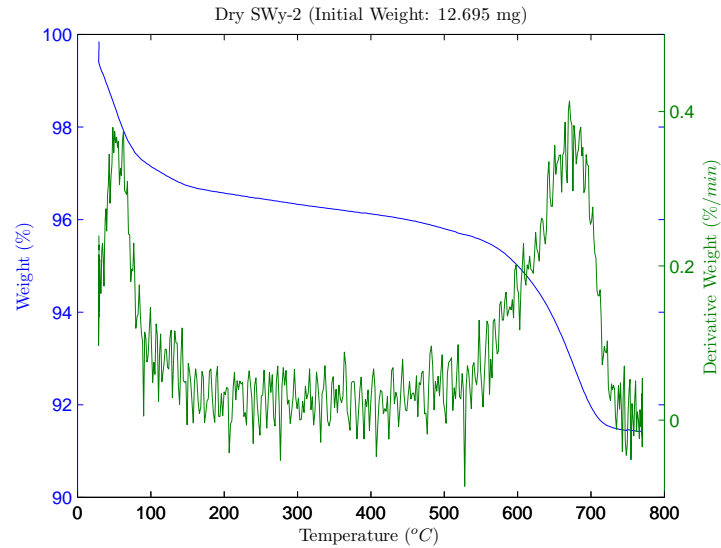


Figure 3.8. Thermal gravimetric analysis (TGA) on SWy 2 sample (as received). Derivative thermal gravimetric analysis (DTG), in green, shows two distinct peaks.

in under evaluated values (Souza *et al.*, 2006). This was the initial motivation for determining the sample thickness and roughness. It was realized later that the CSM option overcomes the surface roughness. The surface topography of the samples was then used to better characterize them.

The clay films were characterized with the Wyko optical profiler, which is based on the interferometry principle. Interferometry is a versatile measurement technology for examining surface topography with very high precision. An interferometer is an optical device that splits a beam of light exiting a single source into two separate beams and then recombines them. The resulting interference phenomena are subsequently recorded in the form of an interferogram. An interferogram carries a wealth of information about the profile of an object under test and its material characteristics. Commonly, interferometers employ a system where one beam is reflected from the object under test and the other beam is reflected from a reference mirror. The beams

are recombined to create bright and dark bands called fringes that make up the interferogram. Fringes, like lines on a topographic map, represent the topography of the object. The interferogram is registered and forwarded to the computer for processing using interferometric phase-mapping programs (Hariharan, 1996). The benefits of optical surface profilometry include the ability to perform non-contact measurements of delicate surfaces, increased height resolution, and high measurement speed.

The average roughness of the glass substrate measured using the Wyko optical profiler was 9 nm (Figure 3.9). The muscovite sample was  $39.76 \pm 1.75 \mu\text{m}$  thick (Figure 3.10) and the average roughness was  $2.25 \mu\text{m}$  (Figure 3.11). The kaolinite sample was  $3.2 \pm 0.28 \mu\text{m}$  thick and the average roughness was 48.76 nm (Figure 3.12). The montmorillonite (SWy 2) sample was  $6 \mu\text{m}$  thick (Figure 3.13) and the average roughness was  $1.36 \mu\text{m}$  (Figure 3.14).

### 3.4 Results

The mechanical properties of fused silica were characterized using the Nano XP as part of the calibration procedure (Figure 3.15). The variation in the data is characterized by one standard deviation from the mean for the range of indentation depth where the material characteristic was found to be stable. We obtained Young's modulus of  $74 \pm 2 \text{ GPa}$  and hardness of  $9.5 \pm 0.45 \text{ GPa}$  for fused silica. Our values matched reasonably well with 69 GPa for Young's modulus reported by Oliver & Pharr (1992).  $P/S^2$  or the material characteristic converges to an approximately constant value after indentation depth of 150 nm, implying that the mechanical properties are that of a bulk homogeneous material. Young's modulus and hardness also reach a plateau of approximately constant value after indentation to a depth of 150 nm, when

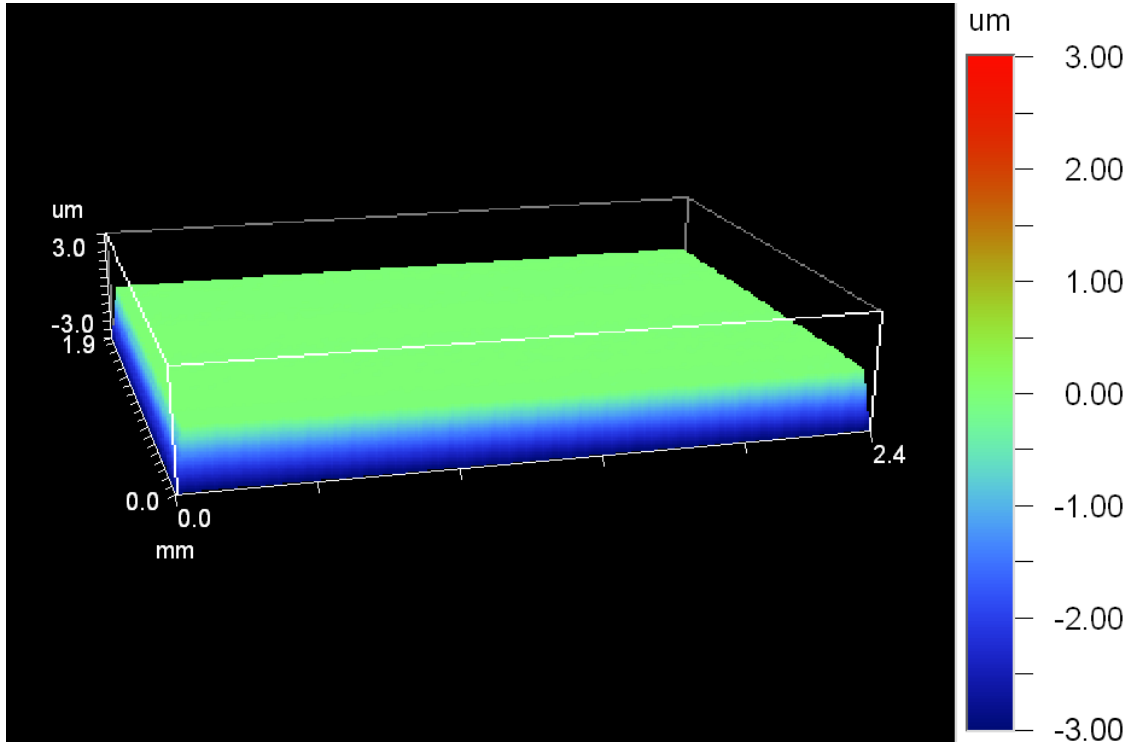


Figure 3.9. Average roughness of the glass substrate measured using the Wyko optical profiler was  $9 \text{ nm}$ .

the indentation size effects or initial noise subside. Our Young's modulus of  $77 \pm 1 \text{ GPa}$  and hardness of  $6.67 \pm 0.1 \text{ GPa}$  for glass substrate matched reasonably well with Young's modulus of  $73 \text{ GPa}$  and hardness of  $6.8 \text{ GPa}$  reported by Saha & Nix (2002).

Young's modulus and hardness for muscovite film on glass substrate (Figure 3.16) reaches a plateau of approximately constant value after indentation to a depth of  $100 \text{ nm}$ .  $P/S^2$  converges to an approximately constant value as the substrate and film properties are similar, although the material is a heterogeneous system with many muscovite layers stacked on top of the glass substrate. The load increases with depth of penetration without any discontinuities indicating that we are not in the plastic regime. We obtained Young's modulus of  $61 \pm 1 \text{ GPa}$  and hardness of  $6.2 \pm 0.2 \text{ GPa}$  for

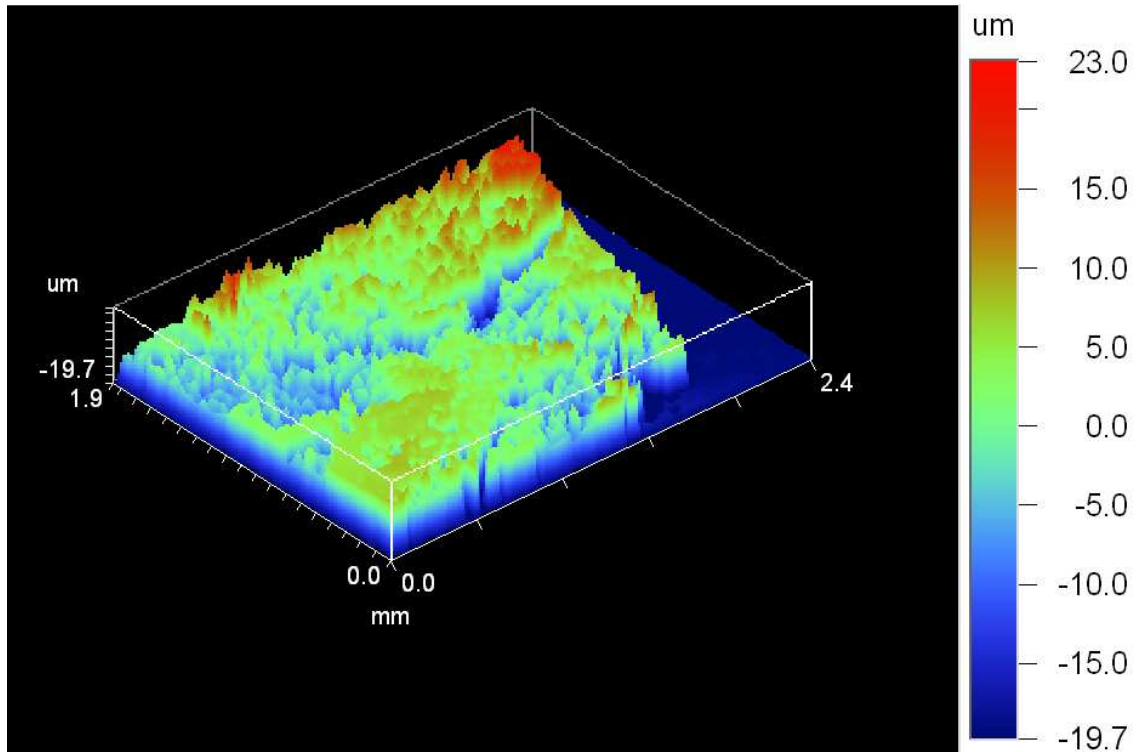


Figure 3.10. Thickness of muscovite sample measured using the Wyko optical profiler was  $39.76 \pm 1.75 \mu\text{m}$ .

muscovite. The Young's modulus values agreed with 61 GPa (Mcneil & Grimsditch, 1993) using Brillouin scattering measurements.

For kaolinite (KGa 1b sample), the substrate and film properties are very different leading to a heterogeneous system with many kaolinite layers stacked on glass substrate. The shifting of clay platelets result in the measurement of void spaces between clay platelets. This leads to near zero values until about 2000 nm of indentation depth in the case of smaller grain sizes of clay ( $1\text{-}2 \mu\text{m}$ ) (Figure 3.17). After 2000 nm, the harder substrate starts influencing the composite results and we see an increase in Young's modulus, hardness and load. Larger grain sizes ( $5\text{-}8 \mu\text{m}$ ) of kaolinite help in achieving a better contact with the indenter tip, thereby giving Young's modulus



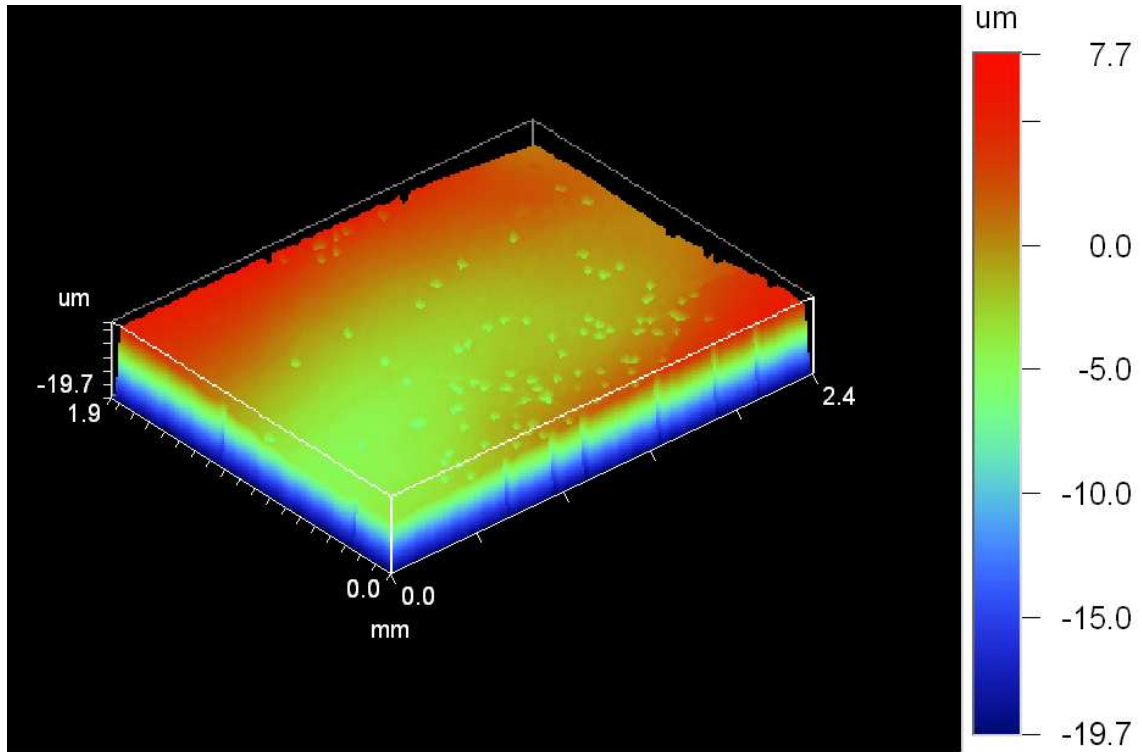


Figure 3.11. Average roughness of muscovite sample measured using the Wyko optical profiler was  $2.25 \mu\text{m}$ .

of  $2.59 \pm 0.08$  GPa and hardness of  $0.0093 \pm 0.0005$  GPa (Figure 3.18) from one of our measurements. Table 3.1 presents all the measurements for Young's modulus and hardness for the KGa 1b sample in the elastic regime. Young's modulus of  $6.2 \pm 2.5$  GPa for dickite, that belongs to the same kaolin subgroup as kaolinite, was reported by Prasad *et al.* (2002) using Atomic Force Acoustic Microscopy (AFAM). In AFAM, Young's modulus is determined by measuring the difference of the cantilever contact resonance frequencies relative to its free resonances. Young's modulus of  $1.3 \pm 0.5$  GPa and hardness of  $0.042 \pm 0.0006$  GPa for kaolinite macrocrystals from the kaolin mineral was reported by Mikowski *et al.* (2007) using nanoindentation which is comparable to our data.

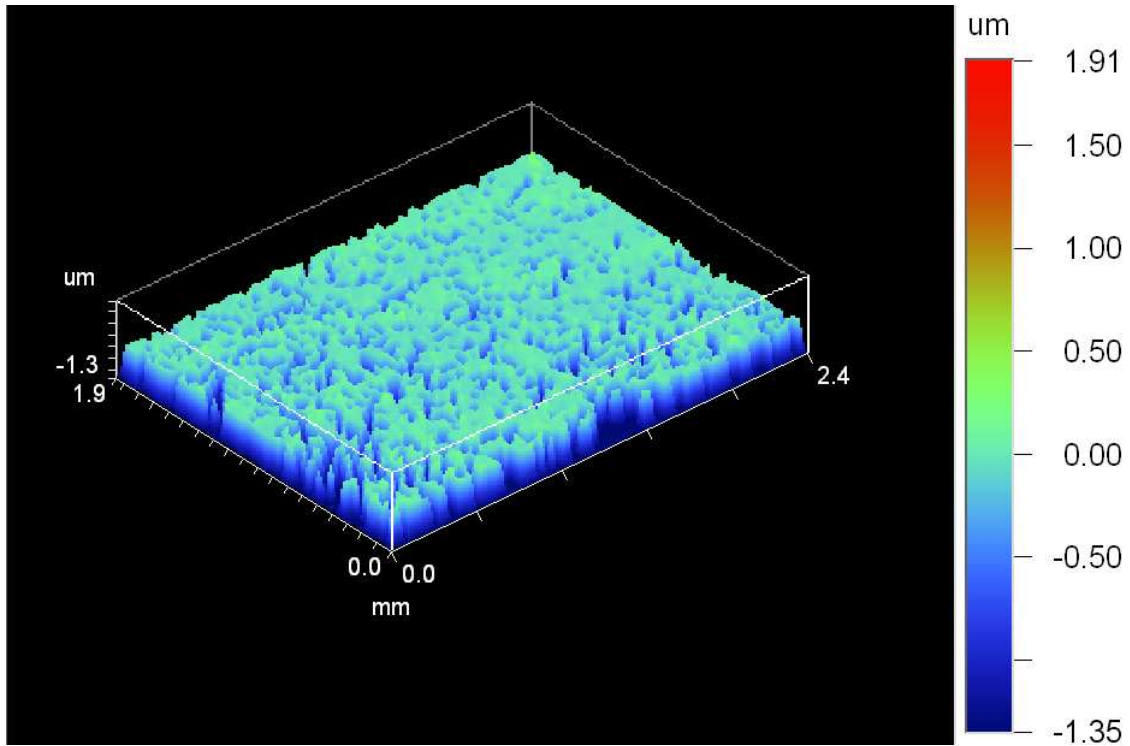


Figure 3.12. Average roughness of kaolinite sample measured using the Wyko optical profiler was  $48.76nm$ .

Young's modulus of 4.07 GPa to 12.1 GPa were obtained for Wyoming montmorillonite, SWy 2 (Table 3.2). And Young's modulus of 6.98 GPa to 14.32 GPa were obtained for Otay montmorillonite, SCa 3 (Table 3.3). The results from one of the measurements for SCa 3 are shown in Figure 3.19. Montmorillonite with larger hardness than kaolinite, helped in achieving a better contact of the sample with the indenter tip, leading to superior convergence in the results (Figure 3.19). The strain rate was also reduced to delay the effect of the substrate. Nanoindentation measurements could not resolve the small changes in Young's modulus due to interlayer water content, leading to similar values for SCa 3 and SWy 2, although they had different water contents.

Table 3.1. Nanoindentation measurements on KGa 1b

|                    | Young's modulus   | Hardness            |
|--------------------|-------------------|---------------------|
|                    | GPa               | GPa                 |
|                    | $2.59 \pm 0.085$  | $0.0093 \pm 0.0005$ |
|                    | $2.585 \pm 0.065$ | $0.023 \pm 0.0002$  |
|                    | $2.6 \pm 0.12$    | $0.026 \pm 0.0016$  |
| Mean               | 2.59              | 0.019               |
| Standard Deviation | 0.008             | 0.009               |

Table 3.2. Nanoindentation measurements on SWy 2

|                    | Young's modulus   | Hardness           |
|--------------------|-------------------|--------------------|
|                    | GPa               | GPa                |
|                    | $4.07 \pm 0.15$   | $0.081 \pm 0.0049$ |
|                    | $6.76 \pm 0.28$   | $0.14 \pm 0.0042$  |
|                    | $4.81 \pm 0.1025$ | $0.06 \pm 0.003$   |
|                    | $12.1 \pm 0.36$   | $0.35 \pm 0.02$    |
|                    | $8.02 \pm 0.4$    | $0.207 \pm 0.014$  |
|                    | $11.12 \pm 0.256$ | $0.25 \pm 0.0049$  |
| Mean               | 7.81              | 0.18               |
| Standard Deviation | 3.27              | 0.11               |

Table 3.3. Nanoindentation measurements on SCa 3

|                    | Young's modulus  | Hardness           |
|--------------------|------------------|--------------------|
|                    | GPa              | GPa                |
|                    | $6.98 \pm 0.33$  | $0.18 \pm 0.129$   |
|                    | $13.44 \pm 0.76$ | $0.33 \pm 0.03$    |
|                    | $7.28 \pm 0.27$  | $0.159 \pm 0.0103$ |
|                    | $14.32 \pm 0.46$ | $0.3 \pm 0.067$    |
|                    | $7.268 \pm 0.74$ | $0.13 \pm 0.035$   |
|                    | $14.14 \pm 0.35$ | $0.36 \pm 0.02$    |
| Mean               | 10.57            | 0.24               |
| Standard Deviation | 3.73             | 0.1                |

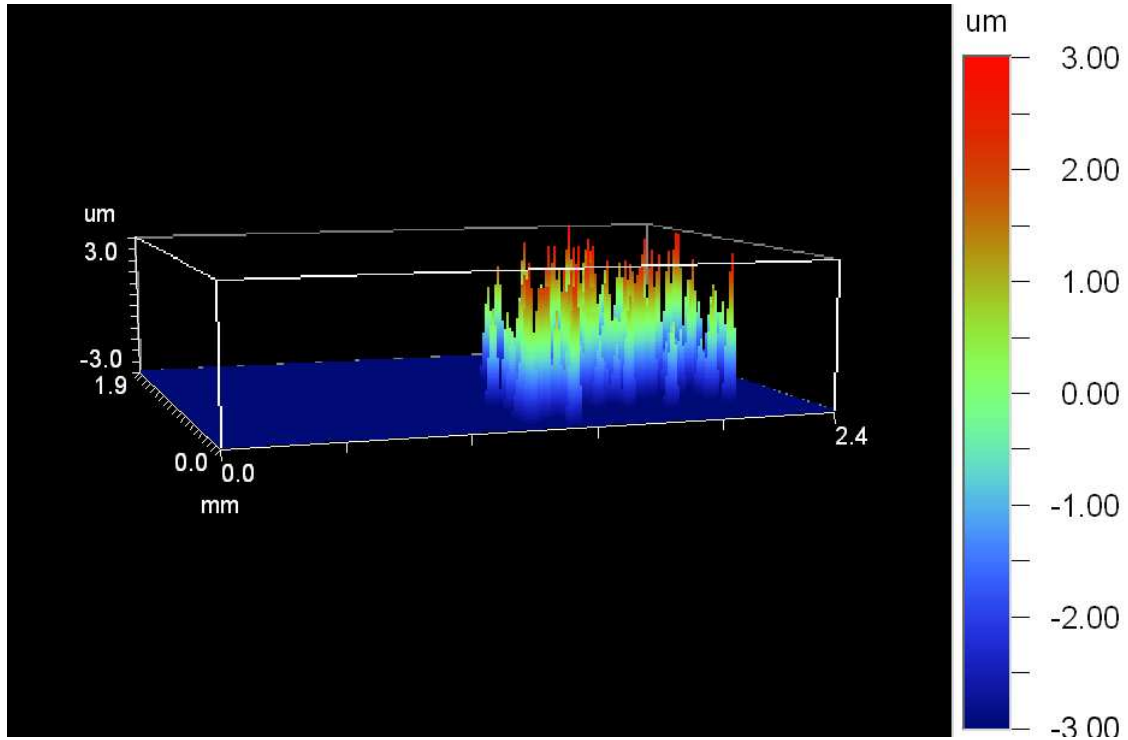


Figure 3.13. Thickness of SWy 2 sample measured using the Wyko optical profiler was  $6\text{ }\mu\text{m}$ .

The greatest challenge of achieving a good contact between the indenter tip and the sample was overcome by taking larger grain sizes, harder mineral and making the surface of the sample as smooth and free of impurities as possible. Although, the samples were pure clay minerals, they had minor amounts of impurities like quartz and feldspar (Chipera & Bish, 2001). One of the reasons for variation in our measurement values within each sample (Table 3.2 and Table 3.3) could be the indenter tip contacting the impurities, although the samples (KGa 1b and SWy 2) were centrifuged to exclude the larger size impurities and each of the indentation spots were carefully chosen. A microscope with better resolution linked to the nanoindenter might be helpful in guiding the indenter tip to avoid the impurities with more certainty. Another

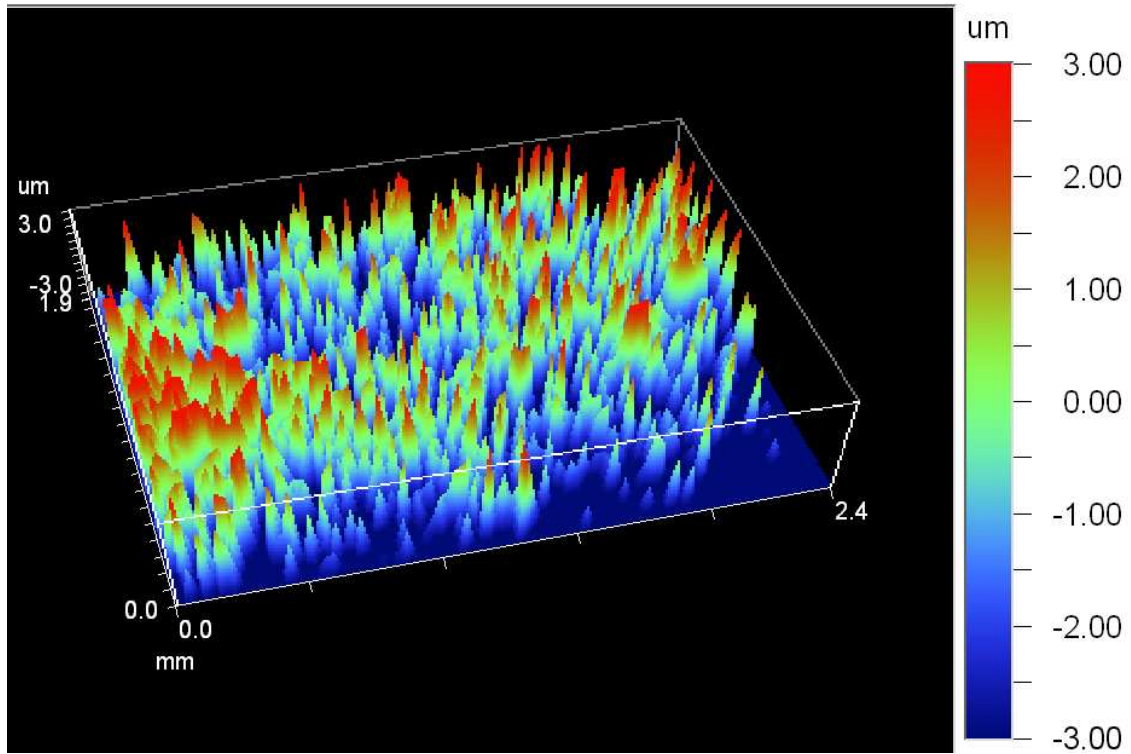


Figure 3.14. Average roughness of SWy 2 sample measured using the Wyko optical profiler was  $1.38 \mu\text{m}$ .

reason for the variations in our measurement values could be the change in humidity in the environment around the samples during the measurements. Controlled relative humidity measurements might improve the resolution in the data, although the humidity might adversely affect the high precision nanoindenter apparatus. Environmental scanning electron microscope (ESEM) showed only the orientation of the top clay platelets in the prepared clay film sample. It is possible that all the clay platelets are not oriented in the same way as the top ones leading to differences in the measured values due to anisotropy.

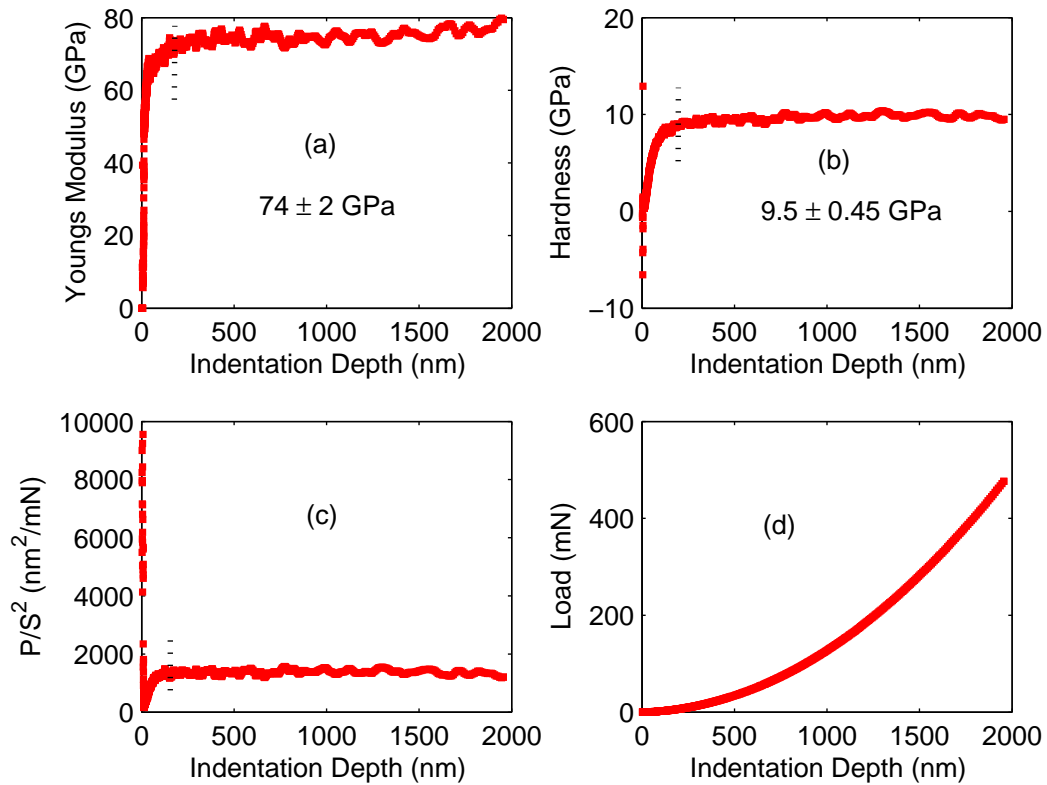


Figure 3.15. Nanoindentation measurements on fused silica. The four panels show (a) Young's modulus; (b) hardness; (c)  $P/S^2$  (material characteristic) is approximately constant from 150 nm of indentation depth, shown by dotted lines and (d) load as a function of indentation depth.

### 3.5 Conclusions

The methodology developed for the analysis of elastic properties of soft thin films on hard substrate worked very well with the clay samples. In kaolinite, Young's modulus of 2.59 GPa to 2.6 GPa was obtained. A larger grain size helped in achieving a better contact with the indenter.

Young's moduli of 4 GPa to 14 GPa were obtained for two different types of natural reference montmorillonite (Otay Sca 3 and Wyoming SWy 2). They match very

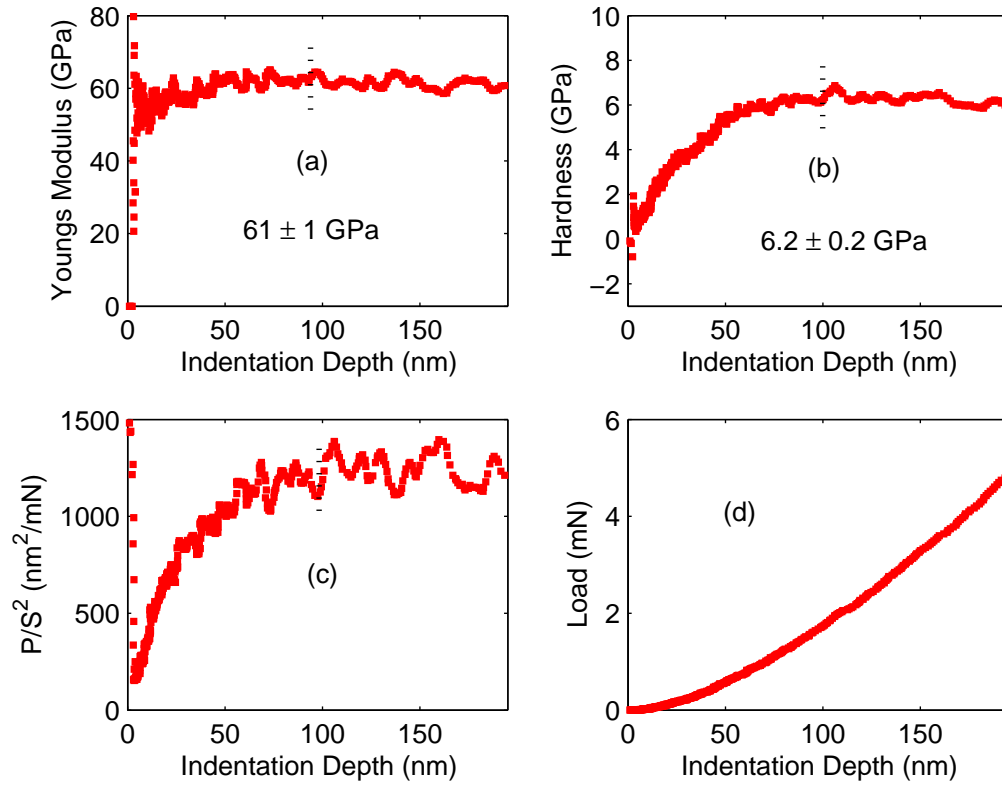


Figure 3.16. Nanoindentation measurements on muscovite film over glass substrate. (a) Young's modulus with indentation depth; (b) Hardness with indentation depth; (c) Material characteristic is approximately constant from 100 nm of indentation depth, shown by dotted lines and (d) Load with indentation depth. Young's modulus of  $61 \pm 1$  GPa and hardness of  $6.2 \pm 0.2$  GPa were obtained. Muscovite and glass having similar properties lead to correct determination of the mechanical properties of muscovite film.

well with our molecular simulation results (5 GPa to 16 GPa) for Young's modulus of Wyoming montmorillonite. This is a significantly narrower range than the 0.15 GPa to 400 GPa range previously reported in the literature. Any sensitivity of Young's modulus to interlayer water content was not evident from the experiments.

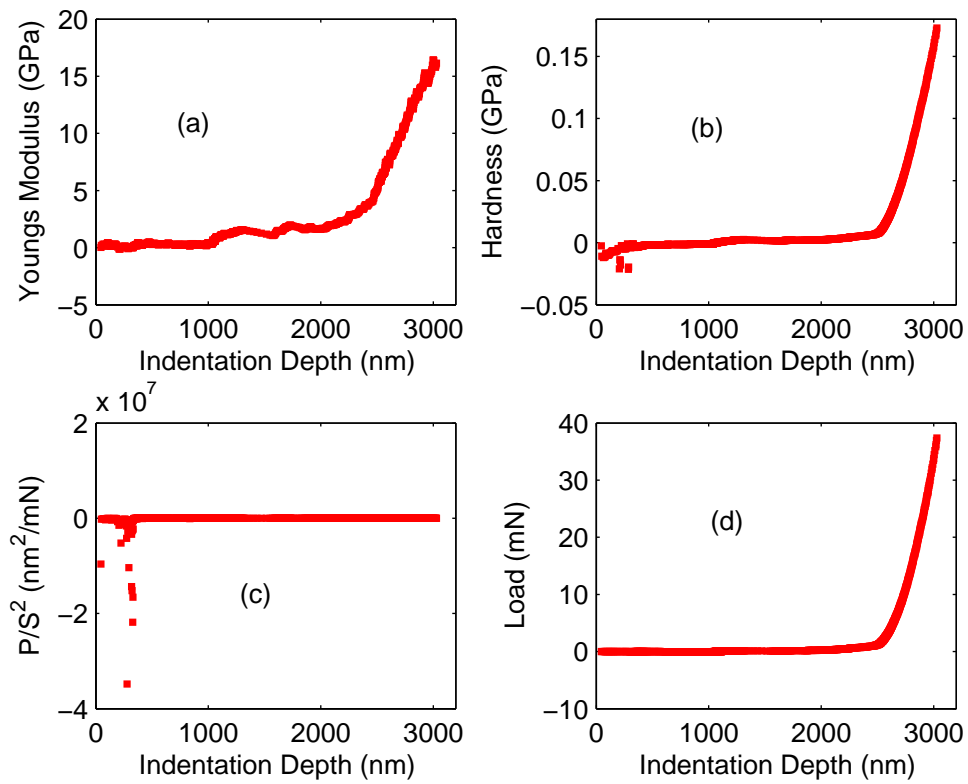


Figure 3.17. Nanoindentation measurements on kaolinite (smaller grain sizes) (KGa 1b) over glass substrate. (a) Young's modulus with indentation depth; (b) Hardness with indentation depth; (c) Material characteristic and (d) Load with indentation depth. Adhesion forces and/or shifting of clay platelets obscure the true mechanical properties of the film.



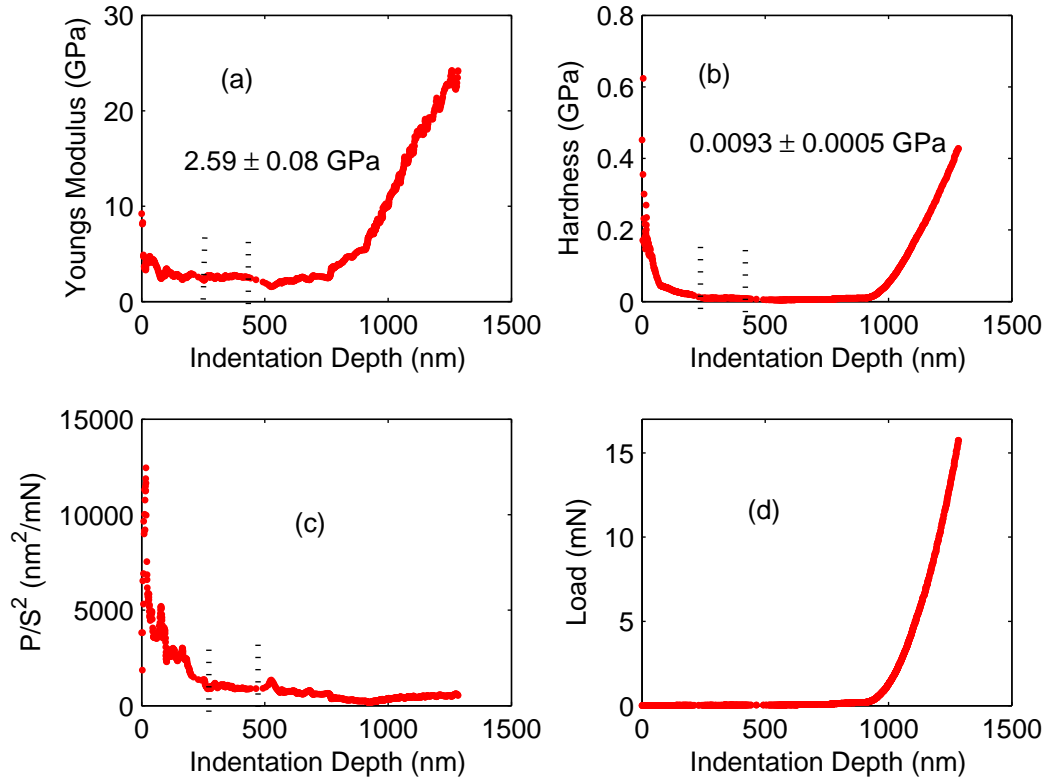


Figure 3.18. Nanoindentation measurements on kaolinite film over glass substrate. (a) Young's modulus with indentation depth; (b) Hardness with indentation depth; (c) Material characteristic is almost constant from 259-435 nm of indentation depth, shown by dotted lines and (d) Load with indentation depth. Effect of substrate is seen after 1000 nm of indentation depth. Larger grain sizes ( $5-8 \mu\text{m}$ ) of kaolinite help in achieving a better contact with the indenter tip, thereby giving Young's modulus of  $2.59 \pm 0.08$  GPa and hardness of  $0.0093 \pm 0.0005$  GPa.

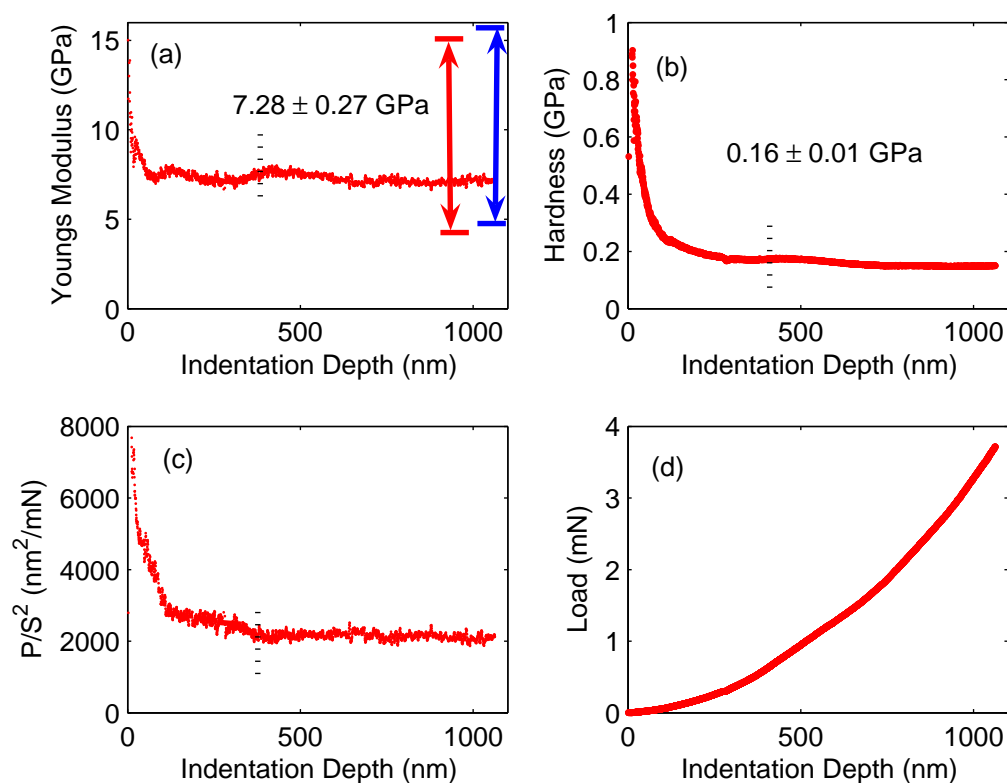


Figure 3.19. Nanoindentation measurements on montmorillonite (SCa 3) over glass substrate. (a) Young's modulus with indentation depth; (b) Hardness with indentation depth; (c) Material characteristic is almost constant from 400 nm of indentation depth till the end of data acquisition, shown by dotted line and (d) Load with indentation depth. Young's modulus of  $7.28 \pm 0.27$  GPa and hardness of  $0.16 \pm 0.01$  GPa were obtained from one of the measurements. The red arrow shows the full range of Young's modulus for montmorillonite obtained from all the nanoindentation measurements and the blue arrow shows the same from molecular simulation for montmorillonites. The hardness of this clay mineral being more than kaolinite helped in achieving a better contact of the sample with the indenter tip, leading to superior convergence in the results.

## Chapter 4

### AN EXPERIMENTAL STUDY OF THE DILATION FACTOR

#### 4.1 Summary

Dilation factor ( $R$ ) is defined as the ratio of the relative change in velocity to the relative change in deformation (strain).  $R$  has significant implications for time-lapse(4D) seismic studies where it can be used to infer reservoir or overburden thickness changes from seismic changes.

We conducted deformation and ultrasonic experiments to study the effect of stress on the dilation factor. Measured absolute  $R$  values ranged from 6 to 91 in sandstones and from 6 to 11 in shale.

$R$  values are dependent on the deformation mechanisms causing the strain. The dynamic Young's modulus (low amplitude) is generally higher than the static Young's modulus (high amplitude) as they correspond to different deformation mechanisms. Hence, theoretical models that use the same mechanisms to describe both wave propagation and macroscopic deformation are not valid. The ratio of dynamic to static moduli depends on the direction of stress applied with respect to the density and placement of cracks.

$R$  values are different for P and S waves, especially in the presence of fluids.  $R$  values were also found to be strongly dependent on the stress state, implying that using a constant value of  $R$  from the seafloor to the reservoir depth should be avoided. This study shows that absolute  $R$  values increase for sandstones and decrease for

shales with decreasing confining pressure, which explains the low  $R$  values from 4D seismic data. Our data not only offers insight into the behavior of  $R$  values with different rock types, stress and fluid but they can also be used to constrain modeling calculations.

## 4.2 Introduction

Dilation factor is defined as the ratio of the relative change in velocity to the strain, where the relative velocity change is the ratio of the change in velocity to the initial velocity. It is used in 4D seismic studies to infer reservoir or overburden thickness changes from time-lapse travel time shifts. Detecting geomechanical changes to predict well failure or borehole stability and monitor reservoir depletion opens up new ways of using 4D data.

Time-lapse seismic monitoring of pressure-induced changes in depleting North Sea gas fields has revealed that detectable differences in seismic arrival times are observed above the reservoir interval. Geomechanical models of depleting reservoirs predict that, as a result of reservoir compaction due to pressure depletion, changes in stress and strain fields occur in the rocks bounding the reservoir (Hatchell *et al.*, 2003).

Hatchell & Bourne (2005b) constructed forward models of time-lapse time shifts from stress and strain fields computed using geomechanical models and a stress-strain-dependent seismic velocity. Based on observations of time-lapse seismic data from several locations around the world, they found that a simple linear model relating seismic velocity with vertical normal strain works well in all their cases. Time shifts were computed as the product of vertical normal strain and velocity-strain coupling

coefficient(-R). Their observations also show that the velocity-strain dependence is larger for rock elongation than for rock contraction. The former is about 5 and the latter is less than half this value. They obtained theoretical estimates of -R values in the range of 1-3 from empirical velocity-porosity trends and in the range of 2-10 using crack models.

Carcione *et al.* (2007) used two different petro-elastic models (Asperity Deformation and Hertz-Mindlin) at varying effective pressures to show that the fractional changes in layer thickness,  $\frac{\Delta L}{L}$ , and seismic velocity,  $\frac{\Delta V}{V}$ , are linearly related. Dilation factor (R) is negative and its absolute value is predicted to decrease for shale or increase for sandstone with increasing layer thickness or decreasing effective pressure.

Various investigations have documented the change in velocities with stress. Wylie *et al.* (1958) examined the factors that affect the velocity of ultrasonic signals in porous media. They compared and discussed the data obtained when three cores from the same rock were uniformly compressed, axially compressed, and circumferentially compressed. They found that velocity increases with increasing differential pressure. The increase is at first rapid and then decreases with increasing differential pressure until an approximately constant, terminal velocity is attained. Compressional ( $V_p$ ) and shear ( $V_s$ ) velocities were measured by Ball & Batzle (1994) on five sandstone samples as a function of triaxial stress.  $V_p$  was found to be primarily controlled by the stress applied parallel to the direction of propagation. Both axial and lateral or normal stresses were found to have a strong influence on  $V_s$ . Vega (2003) obtained similar results on unconsolidated sands.

However, the sample deformations occurring during these measurements are rarely reported. But, we can estimate the static strains from dynamic velocities, by ignoring the differences between the static and dynamic elastic properties. Ta-

ble 4.1 presents the  $R$  values directly reported or extracted from the data given in previous studies. The major inconsistencies in  $R$  values from 4D seismic studies, theoretical models and core analysis are not well understood as indicated by Janssen *et al.* (2006).

This is the first laboratory study to directly report  $R$  values for sandstones and shale. We conducted ultrasonic experiments to study the effect of stress on the dilation factor as stress paths are a dominant factor in controlling acoustic velocities and strain. We examined both sandstones and shale, which constitute most traditional reservoir rocks and overburden respectively. Cylindrical samples were subjected to differential pressure radially while being subjected to axial stress. Acoustic velocities and strains were measured parallel and normal to the axial stress direction. Uniaxial stress data was measured by increasing the axial stress at various constant differential pressure values. The effect of saturation was studied by comparing dry and brine-saturated samples in sandstones. Data in this study correspond to the downloading cycle of confining pressure to simulate reservoir conditions during production. Our results will help constrain modeling calculations.

### 4.3 Sample Description

Table 4.2 presents the petrological data of all the samples used in this study. X-ray diffraction and scanning electron microscope analyses were performed by Core Laboratories, Inc. for Berea and Lyons sandstone, by GeoSystems LLP for Foxhill sandstone and by Chevron-HETC for the shale. Plug porosity, air permeability (sandstones) and grain density (sandstones) were measured in the laboratory (University of Houston and Center for Rock Abuse, Colorado School of Mines). Permeability for

Table 4.1. Review table for dilation factor (R)

| -R      | Data             | Stress (MPa)                             | Method                                    | Lithology                   | Reference                     |
|---------|------------------|--|---|-----------------------------|-------------------------------|
| 4:6     | R                | in situ                                  | 4D seismic                                | Shale                       | Hatchell & Bourne (2005b)     |
| 1:3     | "                | "  | "   | Sandstone or carbonate      | "                             |
| 1:3     | "                | -  | Velocity-porosity model                   | -                           | "                             |
| 2:10    | "                | -  | Microcrack model                          | -                           | "                             |
| 4.4:5.4 | R                | 5:40 (Differential)                      | Asperity-deformation model                | Shale                       | Carcione <i>et al.</i> (2007) |
| 2:2.3   | "                | "  | Hertz-mindlin model                       | "                           | "                             |
| 4.25:5  | "                | "  | "   | Sandstone                   | "                             |
| 1.5     | R                | in situ                                  | 4D seismic (Valhall Field)                | Sandstone                   | Røste <i>et al.</i> (2005)    |
| 2.6     | "                | "  | "   | Shale                       | "                             |
| 304     | Velocity, strain | 2.4:8.2 (Uniaxial)                       | Laboratory uniaxial strain                | Finest-grained sands        | Vega (2003)                   |
| 283     | "                | 4.3:10.3                                 | "   | Fine-grained                | "                             |
| 147     | "                | 2.6:8.1                                  | "   | Coarse-grained              | "                             |
| 729     | Velocity         | 0:7 (Uniaxial)                           | Laboratory uniaxial stress                | Dry Berea sandstone block   | Sarkar <i>et al.</i> (2003)   |
| 45:40   | Velocity         | 7:14 (Differential)                      | Laboratory hydrostatic stress (North sea) | Brine-saturated shale cores | Wang (2002)                   |
| 10:30   | R                | Various                                  | Laboratory (Ekofisk field)                | Chalk cores                 | Janssen <i>et al.</i> (2006)  |
| 2       | "                | in situ                                  | 4D seismic (Ekofisk field)                | Chalk                       | "                             |
| 4:6     | "                | "  | "   | Shale                       | "                             |
| 6:91    | R                | 63:7 (Differential) and 7:56 (Uniaxial)  | Laboratory ultrasonic and deformation     | Sandstones                  | Present study                 |
| 6:11    | R                | 49:7 (Differential) and 3.5:7 (Uniaxial) | "   | Shale                       | "                             |

shale is from Horsrud *et al.* (1998) and grain density from Chevron-HETC. All samples were prepared with bedding plane normal to the axial direction. Sample lengths were around 9 cm and diameters around 3.75 cm. The shale sample was shorter (4.6 cm) to reduce fluid flow time.

Table 4.2. Sample properties

| Sample Name     | Mineral Constituents  | Plug Porosity | Air Permeability | Grain Density |
|-----------------|---|---------------|------------------|---------------|
| Units           | (%)   | (%)           |                  | gm/cc         |
| Lyons           | Quartz(98)<br>Feldspar(2)   | 7.06          | 0.014 mD         | 2.48          |
| Berea           | Quartz(84.4)<br>Clay(5.2)<br>Feldspar(4.8)<br>Ankerite(4.8)<br>Siderite(0.4)<br>Calcite(0.3)<br>Mica(0.1)                         | 19            | 200 mD           | 2.65          |
| Foxhill         | Quartz(73)<br>Tridymite(12)<br>Clay(10)<br>K-Feldspar(2)<br>Plagioclase(2)<br>Almandite garnet(1)                                 | 24            | 100 mD           | 2.48          |
| North Sea Shale | 2:1 Clay+Mica(51)<br>Kaolinite(16)<br>Opal(16)<br>Quartz(9)<br>Halite(3)<br>Feldspar(2)<br>Pyrite(1)<br>Calcite(1)<br>Siderite(1) | 19            | 1 nD             | 2.68          |



#### **4.3.1 Lyons Sandstone**

This sandstone is a Permian aeolian deposit composed of rounded grains with a grain size of about 0.2 mm and is well cemented. The grains do not show microcracks, and grain boundaries are not obvious in scanning electron microscope images.

#### **4.3.2 Berea Sandstone**

This sandstone is fine-grained and weakly laminated. It has a predominantly quartzose framework. The microporosity is associated with authigenic kaolinite and constitutes 10.5% of the total porosity (19%).

#### **4.3.3 Foxhill Sandstone**

This sandstone is fine to medium-grained and has a mean grain size of 0.21 mm. Grains are subangular to rounded and moderately well-sorted. This sandstone has moderate amounts of quartz in the framework. Authigenic clay is the dominant clay and is a mixture of kaolinite, chlorite and smectite. The microporosity constitutes 33% of the total porosity.

#### **4.3.4 North Sea Shale**

This shale is very fine grained and compacted with a laminated texture. Appropriate procedures for sample handling were developed to maximize the preservation of the shale in its natural state. For example exposure to air was minimized by keeping the core immersed in mineral oil. The mineral oil was used as a coolant to avoid contact with water-based fluids which may cause unwanted physico-chemical reactions during sample preparation (drilling, grinding). A schematic diagram of the shale

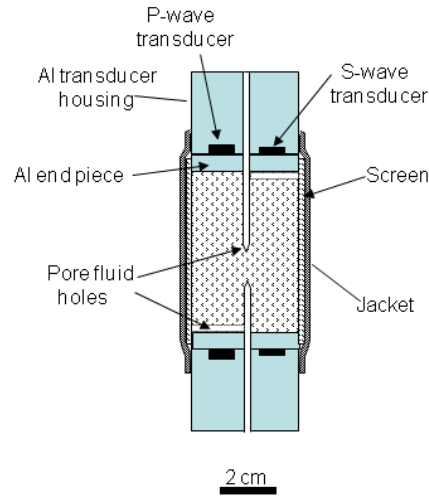


Figure 4.1. Schematic diagram of the shale sample prepared. Mesh screens were placed on the sample to improve fluid flow and attain faster equilibrium. Strain gages and transducers to measure deformation and velocities were also attached.

sample prepared is shown in Figure 4.1. The low permeability of shale extended the time taken for the fluid and the rock to equilibrate at the different stress conditions. Hence, mesh screens were placed on the sample to improve fluid flow.

#### 4.3.5 Rock Strength

The approximate strength of the rock samples was calculated and stress regimes were developed to ensure that the applied stresses did not lead to the failure of the sample. The maximum uniaxial stress and the differential pressure were constrained by the uniaxial compressive and crushing strength of the rock samples respectively.

The generalized rock failure envelopes for sandstones were calculated using Jizba's relation (Jizba, 1991), as shown in Equation 4.1,

$$\tau = 37 (0.36 - \phi)^{1.05} \sigma_n^{0.6} \quad (4.1)$$

where  $\tau$  and  $\sigma_n$  are the shear and normal stresses at failure and  $\phi$  is the porosity. Uniaxial compressive strength,  $C_o$ , was calculated using Jizba's relations, Dobereiner and DeFreitas critical porosity value of 0.42 (Dobereiner & DeFreitas, 1986) for weak sandstone and the formulation of Hoek & Brown (1980) (Batzle *et al.*, 2006) (Equation 4.2),

$$C_o = -25m + 25[m^2 + 2520(0.42 - \phi)^{2.8}]^{1/2} \quad (4.2)$$

where  $m$  is a parameter dependent on lithology ( $m=15$  for sandstones). The equation 4.2 was verified on the Foxhill sample, which failed as the axial stress reached this rock's uniaxial compressive strength of 16.87 MPa. The crushing strength,  $C_c$ , was calculated using Zhang's relations (Zhang, 1991) in Equation 4.3 for sands with a grain size of 0.2 mm.

$$C_c = \frac{13.9}{\phi} \quad (4.3)$$

The generalized rock failure envelope for shale was calculated using Equation 4.4 (Dewhurst *et al.*, 2007).

$$\tau = 1.54 + 0.38\sigma_n \quad (4.4)$$

Note that Equation 4.4 is for North Sea shale with bedding parallel to the axial direction. This equation overestimated the strength as our shale sample had bedding normal to the axial direction. Uniaxial compressive strength,  $C_o$ , was calculated using Equation 4.5 (Horsrud, 2001) for North Sea shale. No relation was found for calculating the crushing strength,  $C_c$  for shale, however we expect this value to be

significantly lower than  $C_c$  for sandstones.

$$C_o = 243.6(\phi)^{-0.96} \quad (4.5)$$

Table 4.3 presents calculated  $C_o$  and  $C_c$  for all the samples used in this study using Equations 4.2, 4.3 and 4.5.

Table 4.3. Sample strength

| Sample Name     | $C_o$ | $C_c$ |
|-----------------|-------|-------|
| Units           | (MPa) | (MPa) |
| Lyons           | 97.8  | 197   |
| Berea           | 32.8  | 73    |
| Foxhill         | 16.87 | 57.92 |
| North Sea Shale | 7.5   | -     |

#### 4.4 Method

The experimental equipment consisted of a confining pressure vessel, an axial stress controller, a pressure pump and transfer vessel for controlling pore pressure, a digital oscilloscope, a pulse generator, and ultrasonic transducers attached at the top, bottom and sides of the sample, a data acquisition device and a computer. Resistive strain gages were used to measure deformation (Figure 4.2).

Velocities were measured in each sample at ultrasonic frequencies (1 MHz) using the pulse transmission technique (Birch, 1960). Flexible epoxy was cast around the sample to prevent the invasion of hydraulic oil into the sample.

Figure 4.2 shows the axial and radial directions, where stresses were applied and measurements were made. Hydrostatic data were measured when the axial stress

and differential pressures were equal. Uniaxial stress measurements were made while increasing axial stress at various constant differential pressures. For Berea, only the velocities and strain parallel to the axial stress direction were measured, whereas for other samples, the velocities and strain parallel and normal to the axial stress direction were measured. The axial ( $V_{s\parallel}$ ) and radial ( $V_{s\perp}$ ) shear velocities were both polarized radially. The direction parallel to the axial stress direction is also referred to as axial and the normal direction is also referred to as radial. The data used in this study were measured during the downloading cycle of confining pressure.

Figure 4.3 shows the measurement space over which the data were collected for each sample. The stress space is different for the samples due to the difference in their strengths, as shown in the previous section. The confining pressure was decreased from 63 MPa (Berea, Lyons) and 49 MPa (Foxhill, Shale) to 7 MPa. At each confining pressure, the axial stress values were varied from the confining pressure value to 63 MPa for Berea and 49 MPa for Foxhill and Shale.  $K$  refers to a constant ratio of differential pressure to axial stress. To account for pore pressure in the brine-saturated cases, differential pressure ( $P_d = P_c - P_p$ ) and differential axial stress ( $P_a - P_p$ ) were used where,  $P_c$  is the confining pressure,  $P_p$  is the pore pressure,  $P_a$  is the axial stress and  $P_d$  is the differential pressure. Since  $P_p$  is zero for the dry cases, confining pressure is the same as differential pressure and axial stress is the same as differential axial stress. For shale, only brine-saturated data were collected, as special care was taken to keep the sample in its natural state as far as possible. Note that this stress-state matrix is a more general acquisition method and allows analyses along arbitrary stress paths (with  $P_a > P_c$ ) as compared to most studies which collect data only along specific stress paths.

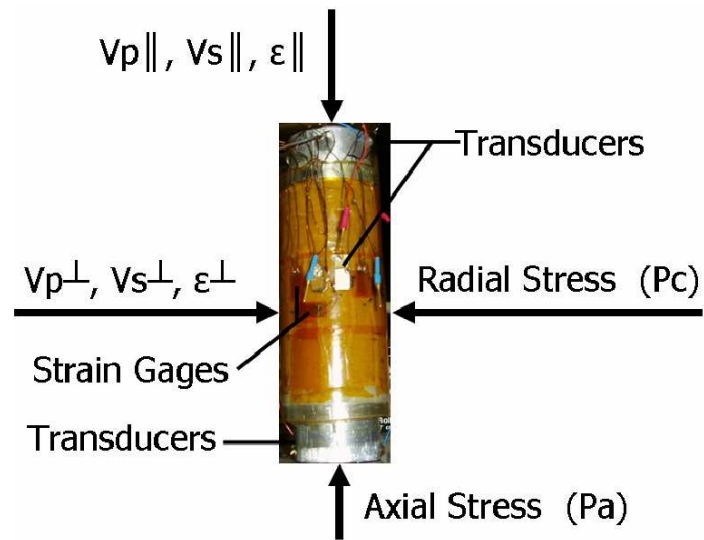


Figure 4.2. Photograph of the Foxhill sample with strain gages and transducers attached to measure the deformation and velocities.  $V_{p\parallel}, V_{s\parallel}, \epsilon_{\parallel}$  and  $V_{p\perp}, V_{s\perp}, \epsilon_{\perp}$  are with respect to the axial stress direction.

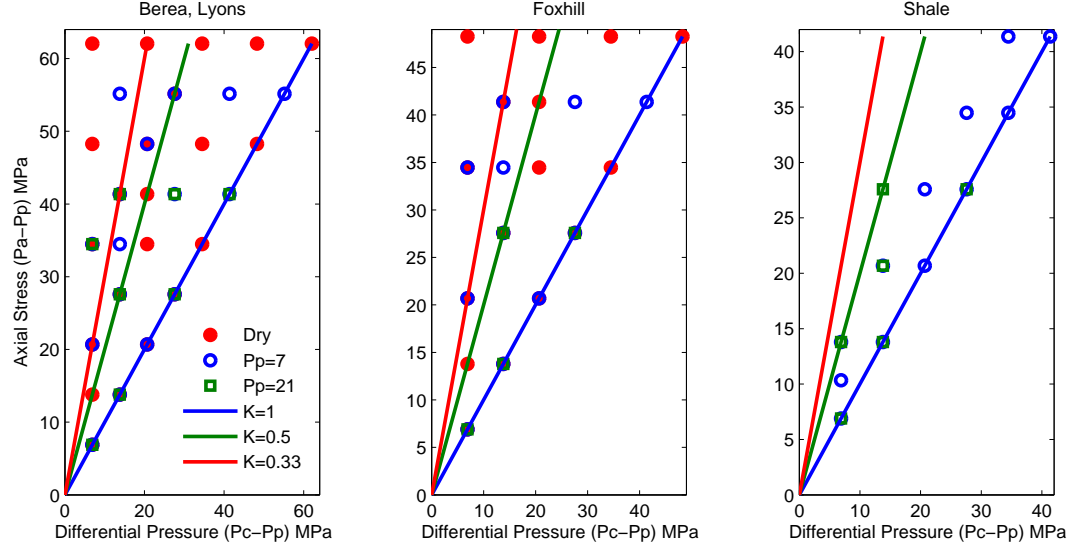


Figure 4.3. Measurement states where each point represents a location in stress space where velocities were measured. Deformation in the sample was continuously recorded throughout the experiment.  $K$  refers to a constant ratio of differential pressure to axial stress. The hydrostatic line for equal stresses with  $K=1$  is shown in blue. Nonhydrostatic lines with  $K = 0.5$  (green) and  $K = 0.33$  (red) are also shown.

#### 4.4.1 Theory

Length changes were measured by the foil-resistance strain gages attached to the sample in the axial and radial directions. The Wheatstone bridge principle was used for more accurate measurements of the length changes. The calibrated micro strain value was computed using Equation 4.6,

$$\mu\epsilon_{cal} = \left[ \frac{1}{G.F.} \right] * \left[ \frac{R_g}{R_{cal} + R_g} \right] * 10^6 \quad (4.6)$$

where,  $\mu\epsilon_{cal}$  = calibrated micro strain;  $G.F.$  = gage factor;  $R_g$  = gage resistance and  $R_{cal}$  = shunt resistance (Micro-Measurements, Product Bulletin PB-105; Measurements-Group, Tech Notes). The measured change in voltage was calibrated to obtain the

micro strain data using Equation 4.7,

$$\mu\epsilon = \left[ \frac{\mu\epsilon_{cal}}{\Delta vol_{cal}} \right] * \Delta vol \quad (4.7)$$

where,  $\mu\epsilon$  = micro strain;  $\mu\epsilon_{cal}$  = calibrated micro strain;  $\Delta vol_{cal}$  = calibrated change in voltage;  $\Delta vol$  = change in voltage.

The velocities and Young's modulus were measured on an aluminum sample to calibrate the equipment setup. Each reading was taken after the strain values had stabilized (about 10 minutes in sandstones and 2 hours in shale). The samples were saturated under pressure for 12 hours with 30,000 ppm NaCl for sandstones and for 48 hours with 50,000 ppm KCL for shale.

Velocity was computed as the quotient of the length of the sample and the travel time. Dilation factor (R) was calculated by finding the ratio of the change in velocity over initial velocity to strain (Equation 4.8),

$$R = \frac{\frac{\Delta V}{V}}{\epsilon} \quad (4.8)$$

where  $V$  is velocity and  $\epsilon$  is strain in the direction of velocity measurement. Strain is the dimensionless ratio of change in length with respect to original length  $\left[ \frac{\Delta L}{L} \right]$  and is considered to be negative for compression/compaction and positive for tension/elongation in this study. Note that R value is always negative as velocity decrease is associated with sample elongation and velocity increase is associated with sample compaction.

Static Young's modulus was obtained from uniaxial stress data, where the axial stress was increased at constant differential pressures. Young's modulus,  $E_s$ , is the



slope of the stress strain curve (Equation 4.9),

$$E_s = \frac{d\sigma_{zz}}{d\epsilon_{zz}} \quad (4.9)$$

where  $d\sigma_{zz}$  is the incremental uniaxial stress and  $d\epsilon_{zz}$  is the strain change along the same direction as the uniaxial stress. In our study,  $d\sigma_{zz}$  refers to  $[P_a - P_c]$  and  $d\epsilon_{zz}$  refers to  $[\epsilon_{\parallel P_a > P_c} - \epsilon_{\parallel P_a = P_c}]$ .

Dynamic Young's modulus was computed using Equation 4.10,

$$E_d = \frac{\rho V_s^2 [3V_p^2 - 4V_s^2]}{V_p^2 - V_s^2} \quad (4.10)$$

where  $\rho$  is the density of the rock and  $V_p$ ,  $V_s$  are the compressional and shear velocities. In our study,  $V_p$ ,  $V_s$  refer to  $V_{p\parallel}$ ,  $V_{s\parallel}$  respectively, as those are parallel to the axial stress direction.

Thomsen (1986) anisotropic parameters  $\varepsilon$  and  $\gamma$  (Equation 4.11 and 4.12) are defined as,

$$\varepsilon \approx \frac{V_{p\parallel} - V_{p\perp}}{V_{p\perp}} \quad (4.11)$$

$$\gamma \approx \frac{V_{s\parallel} - V_{s\perp}}{V_{s\perp}} \quad (4.12)$$

where  $V_{p\perp}$  is the compressional and  $V_{s\perp}$  is the shear velocity normal to the axial stress direction,  $V_{p\parallel}$  is the compressional velocity parallel to the axial stress direction and  $V_{s\parallel}$  is the shear velocity parallel to the axial stress direction and polarized parallel to the bedding plane.

#### 4.4.2 Uncertainty Analysis

Equation 4.13 for propagation of uncertainty, was used to find the uncertainties in velocity and strain measurements,

$$\delta q = \sqrt{\left[\frac{\partial q}{\partial x}\delta x\right]^2 + \dots + \left[\frac{\partial q}{\partial z}\delta z\right]^2} \quad (4.13)$$

where  $x, \dots, z$  are measured with uncertainties  $\delta x, \dots, \delta z$  (which are independent, random and small), and the measured values used to compute the function  $q(x, \dots, z)$  with uncertainty  $\delta q$  (Taylor, 1939). The relative uncertainty is defined as the ratio of uncertainty in a measured value with respect to the measured value ( $\frac{\delta x}{x}$ ).

Relative uncertainty involved in hand-picking first arrival travel times was found to be  $\pm 1\%$ . The relative uncertainty in length was assumed to be the strain value measured to account for the corrections in velocity due to change in length. Applying Equation 4.13, uncertainty in velocity was calculated and plotted as error bars in Figure 4.4.

The relative uncertainty in strain was calculated to be  $\pm 0.5\%$  by applying Equation 4.13 on Equation 4.6. The relative uncertainty in dilation factor (R) was the same as the relative uncertainty in strain, since the uncertainties in the velocities compensate each other (Equation 4.8). The error bars are contained in the size of the symbols for R.

Note that these are measurement uncertainties and they do not include systematic errors or biases due to sample heterogeneity, bad gage mounting etc. But those errors were assumed to be negligible in our experiments due to the calibration procedure on aluminum sample and averaging of strains at the opposite ends of the rock

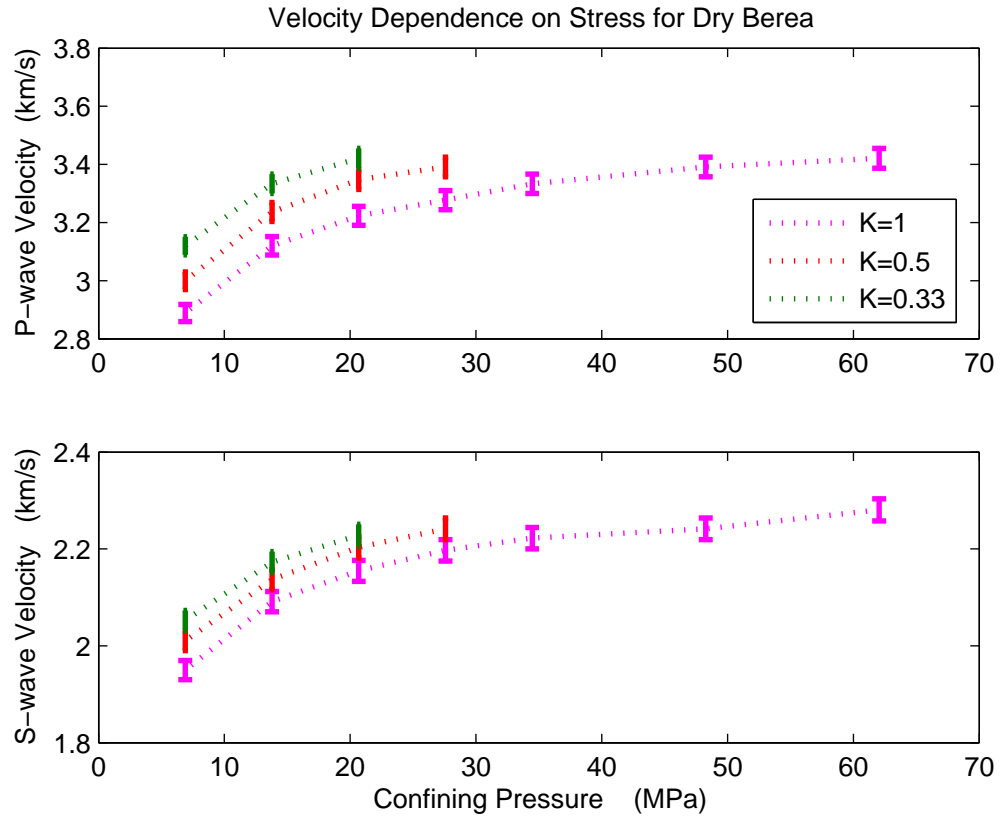


Figure 4.4. Velocity paths under hydrostatic and nonhydrostatic stresses for dry Berea sandstone.  $K$  refers to a constant ratio of confining stress to axial stress. For example  $K=1$  implies a hydrostatic stress state. The uncertainties in measurement of velocity are plotted as error bars. The velocity paths are different for hydrostatic and both nonhydrostatic conditions.

samples.

## 4.5 Results

This section describes the components of dilation factor like ultrasonic velocities; attributes calculated from the components like static and dynamic moduli, anisotropy parameters; and the dilation factor. The dilation factor and its components are discussed separately to better understand the dependence of dilation factor on different rock types, fluid and stress as they complement and/or validate each other.

### 4.5.1 Static vs. Dynamic

Static (macroscopic and isothermal) elastic moduli are equal or lower than the dynamic (adiabatic) moduli (Simmons & Brace, 1965; Jizba *et al.*, 1990; Zimmer, 2003; Olsen *et al.*, 2008). The difference between static and dynamic moduli is related more to the amplitude of the measurement than to the frequency. The very low amplitude ultrasonic waves are not expected to cause motion or frictional sliding along grain boundaries and therefore only sense open pore space compliance. Static measurements cause completely different deformation mechanisms, such as grain rotation and sliding, and therefore the rock appears more compliant. Thus, no model employing a single deformation mechanism can predict this static-dynamic ratio.

The ratio of dynamic bulk moduli to static bulk moduli is strongly dependent on confining pressure (Jizba, 1991; Zimmer, 2003). The ratio of dynamic bulk moduli to static bulk moduli in tight gas sandstones varies from 1 to 3 (Jizba, 1991) depending on shale content and confining pressure. The ratio of dynamic to static Young's modulus for reservoir chalks varies from 1.3 to 5 (Olsen *et al.*, 2008). Our ratio of dy-

dynamic to static Young's modulus also varied from 1 to 3.1 for sandstones (Figure 4.5). The ratio of dynamic to static Young's modulus remains approximately constant for Berea and Lyons. However, this ratio increases dramatically with increase in uniaxial stress for Foxhill. The modulus ratio is a function of the change in crack content with stress. We define 'cracks' as compliant pores, which can be described as having lower aspect ratio. Aspect ratio is the ratio of minor to the major axis of an elliptical pore. Thus, thin open pore spaces between distributed grain boundaries are also referred as cracks in this study. Increase of uniaxial stress in Foxhill generates more open cracks since the strength of this high porosity sandstone is much lower than the other two sandstones (Table 4.3). An increase in stiffness due to decrease in porosity in the different samples is evident from Figure 4.6. Increasing stiffness at higher confining pressures is also seen in all the sandstone samples in Figure 4.6 due to the closure of cracks.

Static Young's modulus obtained for our North Sea Shale varied from 2.6 GPa to 5 GPa. Static Young's modulus of fresh Ashfield Shale varied from 2.7 GPa to 4.9 GPa (Ghafoori *et al.*, 1993) using direct shear, triaxial and UCS tests, which are in close agreement with our values. Values of static Young's modulus for North Sea Shales from various depths ranged from 0.8 to 12.2 GPa (Horsrud *et al.*, 1998), using undrained triaxial tests. Our values fall within the above range.

#### 4.5.2 Velocity

The velocity increase with pressure shows the typical rapid increase at low pressures followed by a flattening of the curve at higher pressures (Wyllie *et al.*, 1958; Ball & Batzle, 1994; Zimmer, 2003). Presumably, cracks are closed at higher pressure and velocities approach a relatively constant velocity. The data collected along K

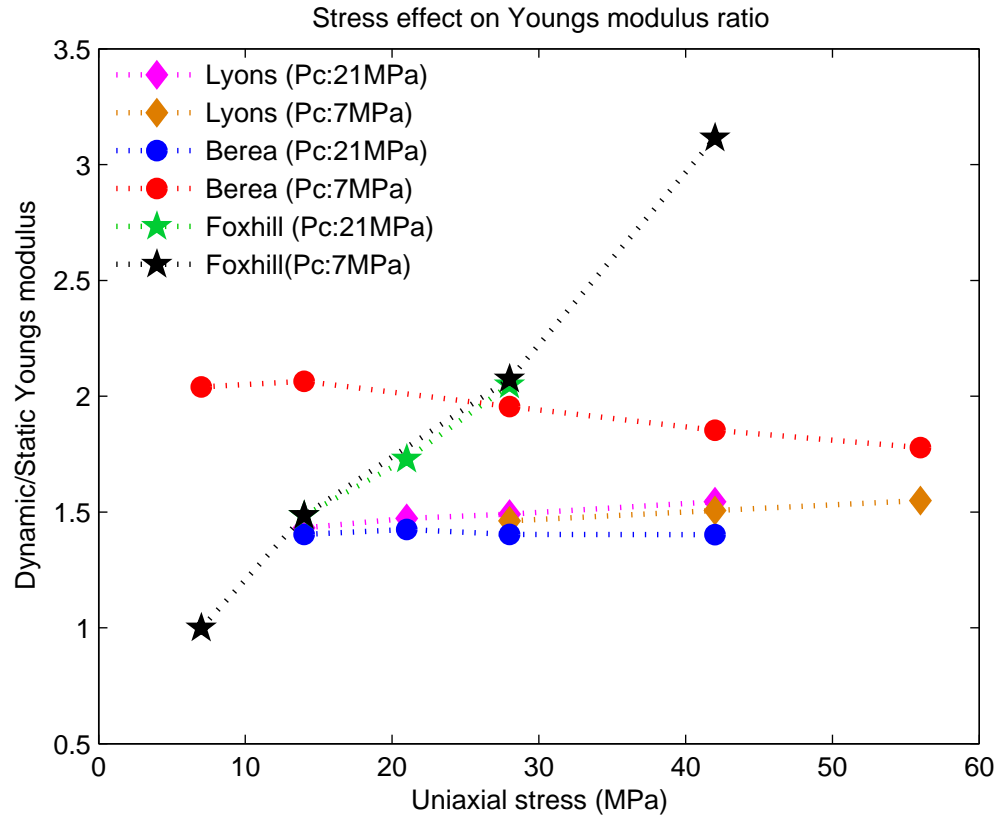


Figure 4.5. Dynamic/Static Young's modulus. The ratio of dynamic to static Young's modulus varies from 1 to 3.1 for sandstones and remains approximately constant for Berea and Lyons. However, this ratio increases dramatically with increase in uniaxial stress for Foxhill. The modulus ratio is a function of the change in crack content with stress.

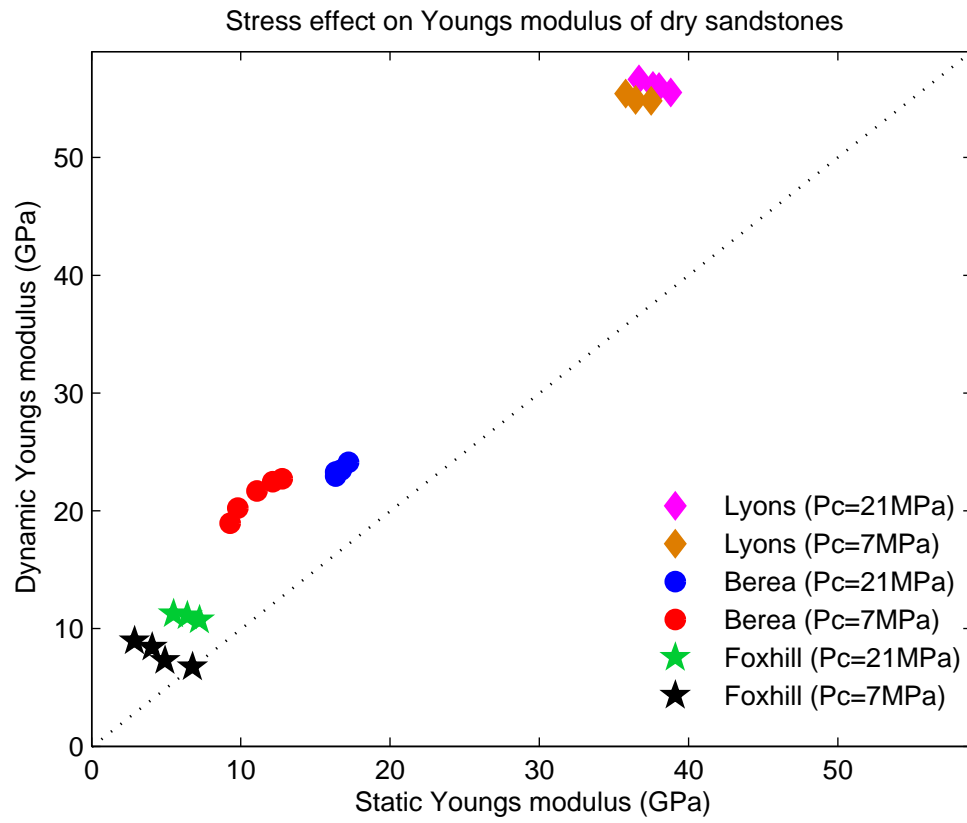


Figure 4.6. Static versus Dynamic Young's modulus. Increasing stiffness with lower porosity and higher confining pressure ( $P_c$ ) is evident.

$= 1$  (hydrostatic or equal stresses,  $P_a = P_c$ ),  $K = 0.5$  (nonhydrostatic,  $P_a = 2P_c$ ) and  $K = 0.33$  (nonhydrostatic,  $P_a = 3P_c$ ), when plotted as a function of confining pressure show that the velocity paths are different for hydrostatic and both nonhydrostatic conditions (Figure 4.4). This is true for all the samples in dry as well as brine-saturated cases, but only the dry Berea case is shown in Figure 4.4.

The magnitude of change in velocity with change in hydrostatic pressure is a qualitative measure of the amount of cracks. This is consistent with the fact that the crack content in Foxhill is highest among the sandstones, which makes it more stress sensitive than Berea or Lyons (Figure 4.7).

Velocity surfaces were calculated from the matrix of velocities measured over axial and differential pressure conditions (Figure 4.3). Contours of equal velocity were then plotted in Figures 4.8, 4.9 and 4.10. These contours make it easier to see the contrasting dependence on stresses for  $V_p$  and  $V_s$ . Note that the shear velocity drops dramatically with saturation, more than can be explained by the density increase. Some form of chemical frame softening is indicated (Adam *et al.*, 2006).

### 4.5.3 Anisotropy

For dry Berea, the P-wave velocity contours (Figure 4.8) show that the axial  $V_p$  is more sensitive to the axial stress than to confining or differential pressure. This may be due to horizontal bedding in our Berea sample. And this sensitivity of  $V_p$  to axial stress is reduced in the brine-saturated cases in comparison to the dry case. This is probably due to the cracks being filled with less compressible fluid which makes the velocities more isotropic.

For dry Foxhill, the P-wave velocity contours (Figure 4.9), show that the radial  $V_p$  is more sensitive to the confining pressure than axial  $V_p$ . This is consistent with



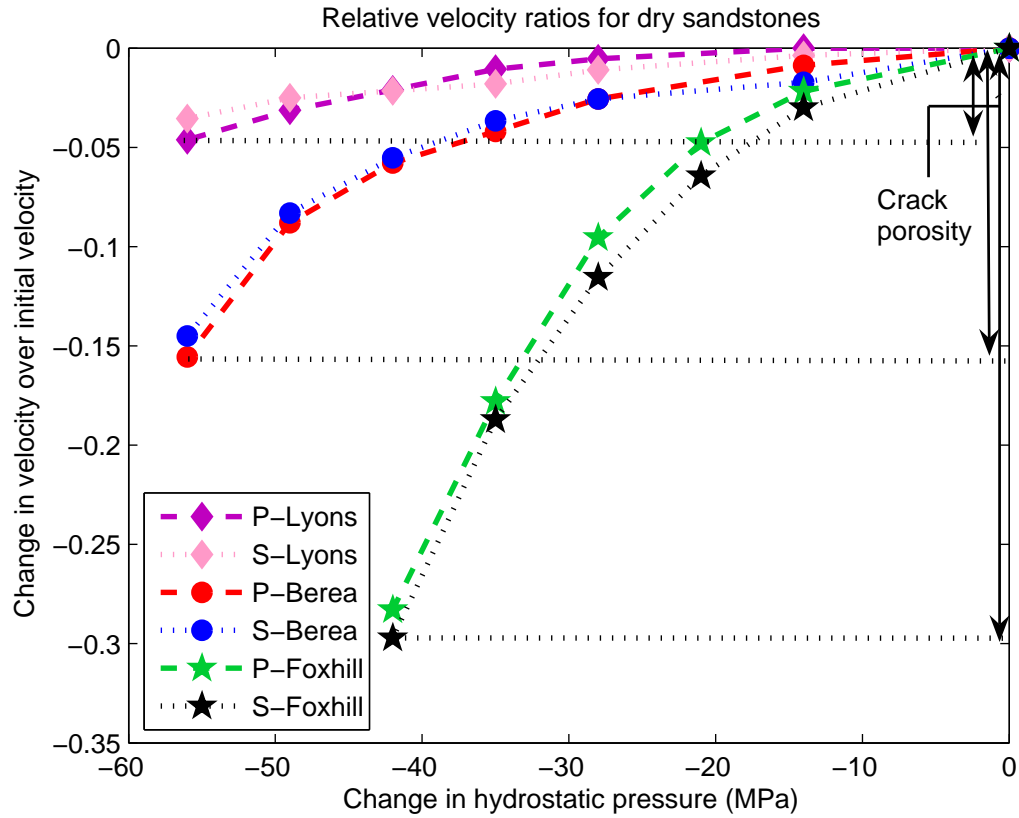


Figure 4.7. Changes in velocities over initial velocity are plotted against change in hydrostatic pressure to find the qualitative influence of crack porosity in sandstones. The crack content in Foxhill is highest among the sandstones, which makes it more stress sensitive than Berea or Lyons.

a wave being most sensitive to cracks when its direction of propagation or direction of polarization is normal to the crack faces. Hatchell & Bourne (2005b) show that vertical P-wave velocity is four times more sensitive to the presence of horizontal than vertical cracks (Figure 4.11) using a theoretical crack model (Sayers & Kachanov, 1995). This implies our Foxhill sample may have a larger population of axially oriented cracks. Sensitivity of axial  $V_s$  (polarized normal to the axial cracks) to confining pressure in brine-saturated case is less compared to the dry case (Figure 4.10).

The Thomsen (1986) anisotropy parameters  $\varepsilon$  and  $\gamma$  showed that crack induced anisotropy increases with axial stress, and this increase is more pronounced at lower confined stress states (Figure 4.12). Sarkar *et al.* (2003) and Fuck *et al.* (2007) also demonstrated that the time-lapse changes of anisotropy can provide useful information about temporal variations in the stress field.

#### 4.5.4 Dilation Factor

A hydrostatic pressure decrease results in a decrease in all velocities. The magnitude of velocity change increases due to increased stress sensitivity of the velocity, owing to larger number of open cracks at low pressures. These cracks result in smaller strains in comparison to the change in velocities at low pressures in sandstones. Hence, the absolute R values are higher at lower pressures as seen in Figure 4.13 for all sandstones. Shales mostly have cracks and few high aspect ratio pores. R values were found to decrease with decreasing confining pressure for shale. The shale sample shows significantly larger deformation in comparison to the sandstones (Figure 4.14). The deformations in shale are larger than the velocity changes at lower confining pressures leading to lower R values. At higher confining pressures, velocity changes are greater than strain, as shales lack high aspect ratio pores. This behavior is also

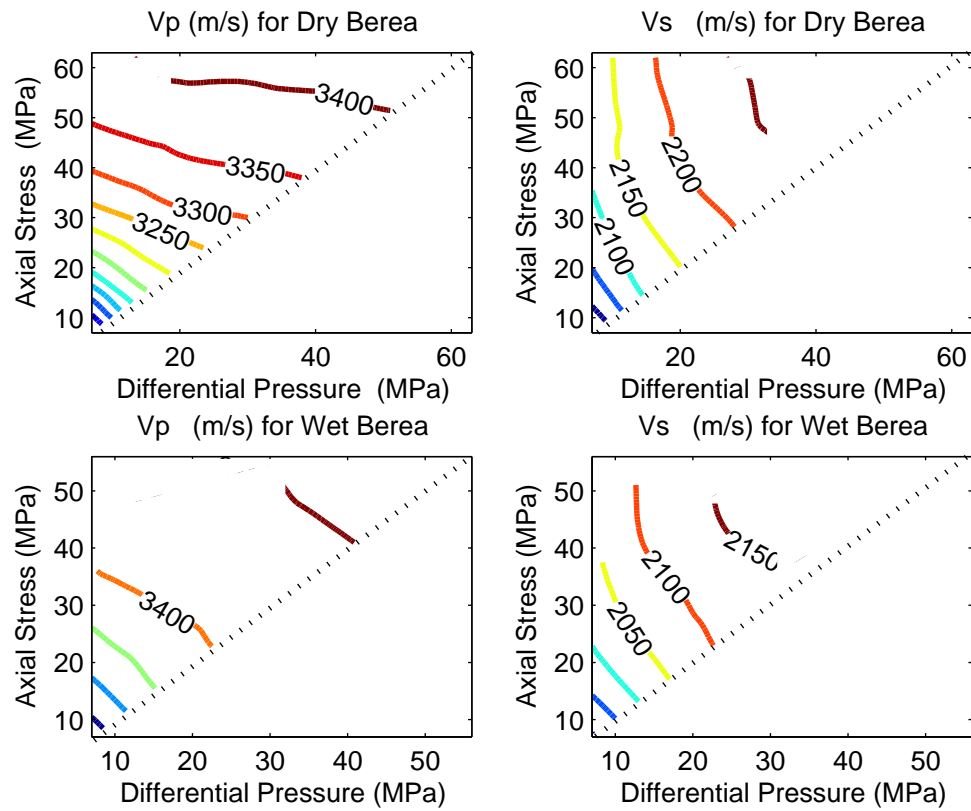


Figure 4.8. Axial velocity contours for dry and brine-saturated Berea. The axial  $V_p$  is more sensitive to the axial stress than to confining pressure in dry P wave velocity contours. See Figure 4.3 for the specific points of measurement.

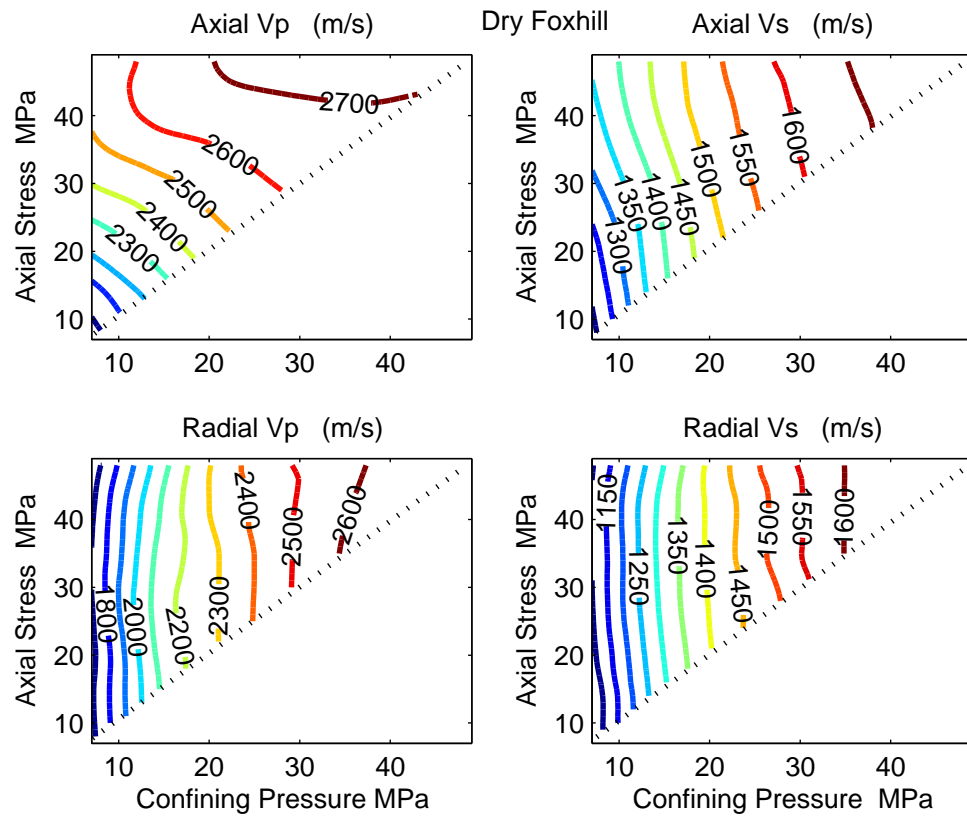


Figure 4.9. Axial and radial velocity contours for dry Foxhill. Radial P-wave velocity is more sensitive to confining pressure than to axial stress.

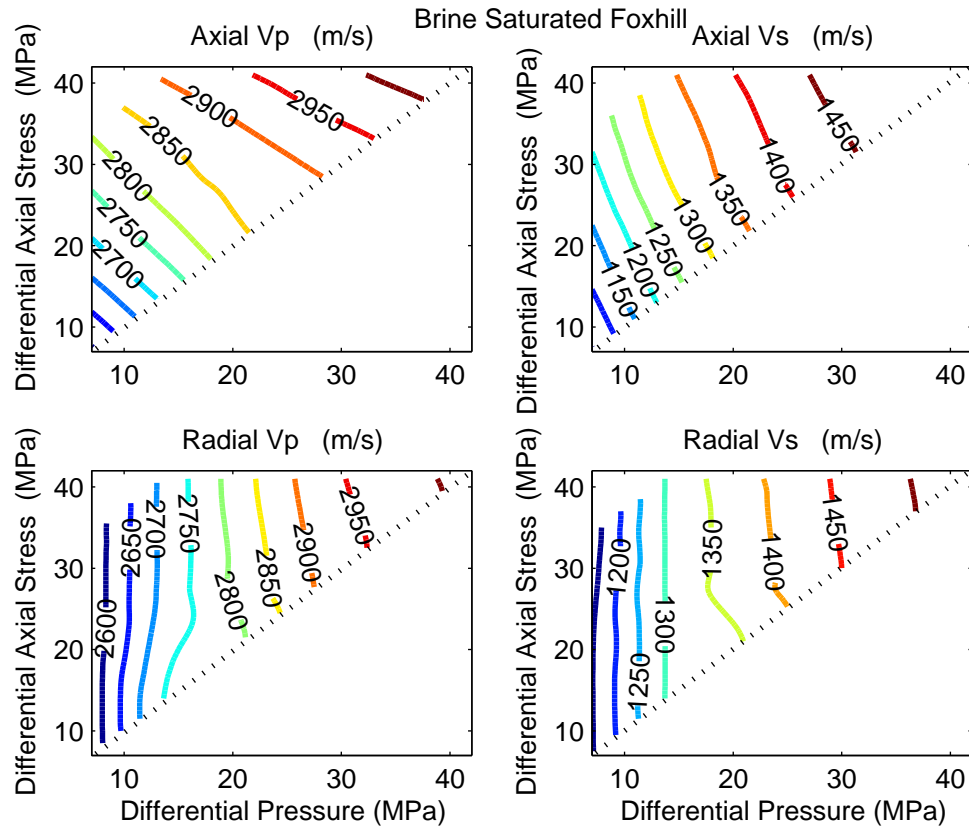


Figure 4.10. Axial and radial velocity contours for brine-saturated Foxhill. Axial  $V_s$  in brine-saturated case is less sensitive to confining pressure compared to the dry case.

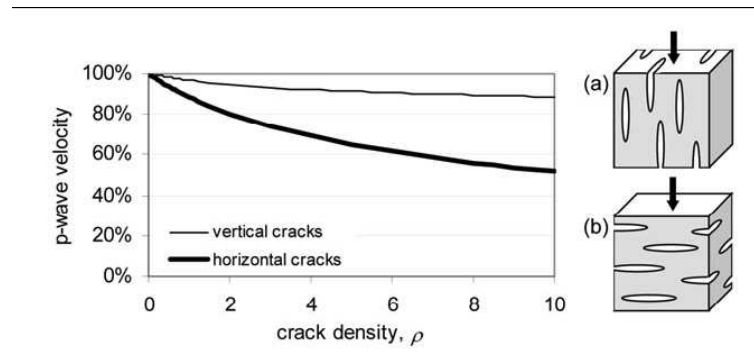


Figure 4.11. Modeled P-wave velocity as a function of crack density and alignment, assuming the pore fluid is incompressible by Hatchell & Bourne (2005b).

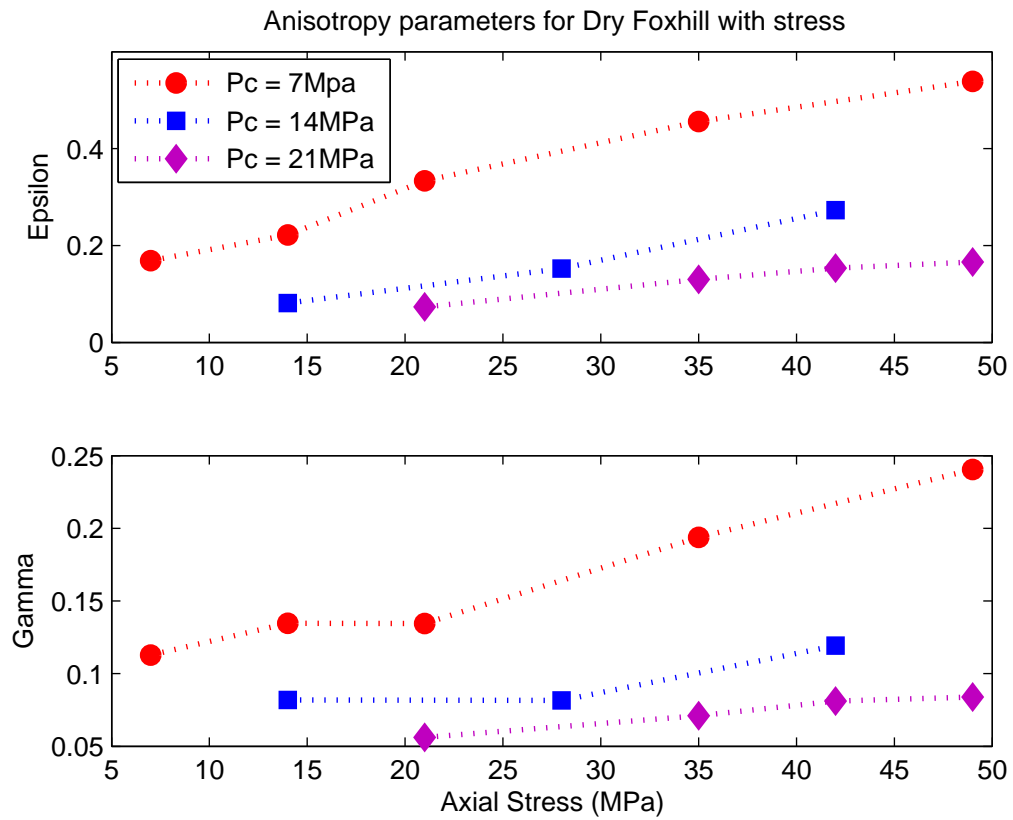


Figure 4.12. Anisotropy parameters plotted as a function of the axial stress. Crack-induced anisotropy increases with axial stress, and this increase is much more at lower confined stress states.

supported by model calculations (Carcione *et al.*, 2007; Holt *et al.*, 2005) as shown in Figure 4.15.

The absolute R value for P-waves is lower for the saturated case than for the dry case (Figure 4.16). This is because brine-saturated (less compressible) rock is stiffer than dry rock. This makes the brine-saturated rock less stress sensitive. Greater stress sensitivity at lower differential pressures leading to higher absolute R values are also seen in Figure 4.16.

Figure 4.18 shows the numerator of R i.e., change in velocity over initial velocity changes, versus uniaxial stress increments. The velocity increase in the direction parallel to axial stress is probably due to crack closure and increases with uniaxial stress. There is velocity decrease due to elongation in the direction normal to the axial stress direction, but it is almost constant. Figure 4.19 shows strain changes versus uniaxial stress increments. Negative strains parallel to the axial stress direction represent compaction, which increases with uniaxial stress. There is elongation in the direction normal to axial stress direction in Foxhill sandstone. Elongation also increases with uniaxial stress. A uniaxial stress increase results in a decrease in absolute R values of the waves propagating (or being polarized for shear waves) along the applied stress direction. The absolute R values of the waves propagating (or being polarized for shear waves) normal to this direction also reduce as seen in Figure 4.17. This is probably because a compressive stress component normal to a crack face may close the crack, thus increasing the velocities, but the length changes are larger than velocity changes. However, if large shear stress is applied, then new cracks primarily aligned with the maximum principal stress might be generated. Here again length changes are larger than velocity changes. Holt *et al.* (2005) also supported this behavior using model calculations as shown in Figure 4.15.

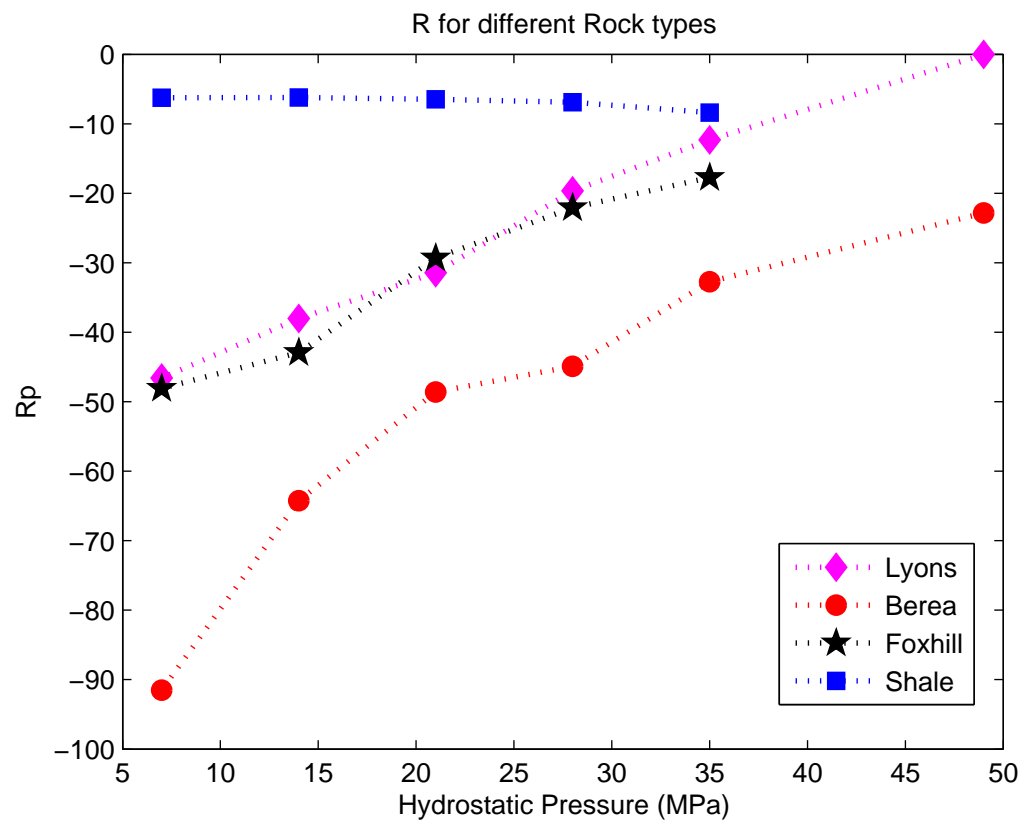


Figure 4.13. R values are plotted as a function of hydrostatic pressure. Absolute R value is at its highest for sandstones at low hydrostatic pressure. Absolute R value is at its lowest for shale at low hydrostatic pressure.



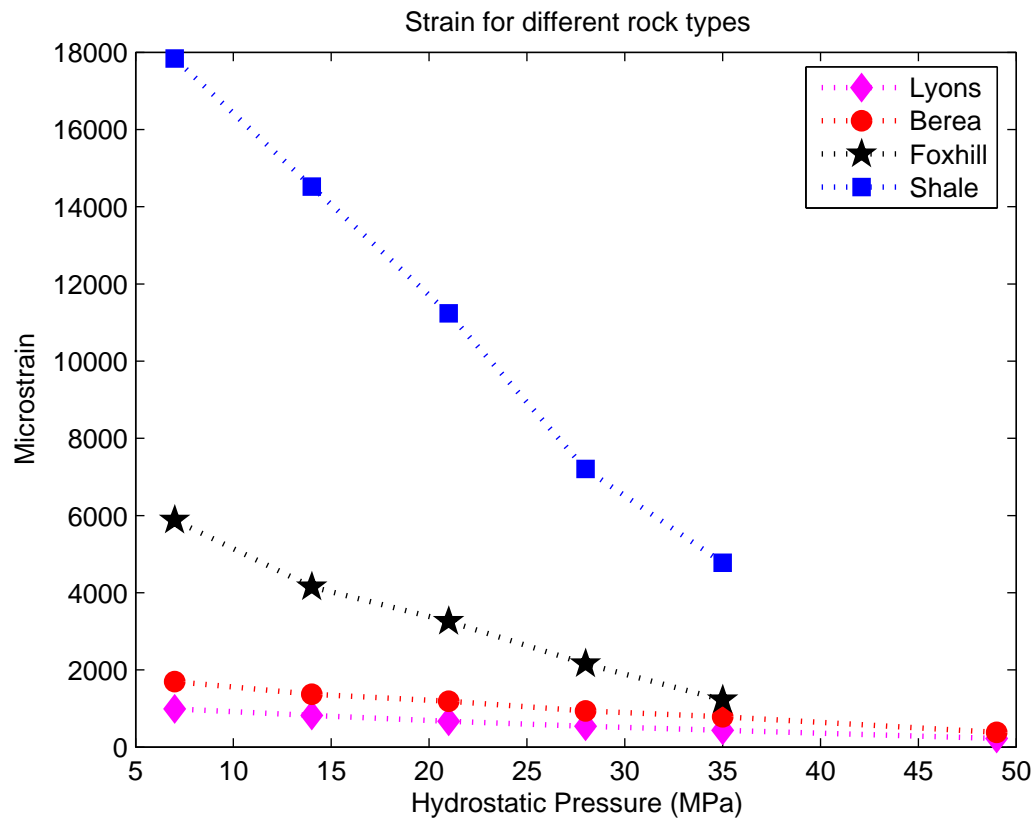


Figure 4.14. Strain as a function of hydrostatic pressure. Samples increase in size as the hydrostatic pressure is decreased. The shale sample shows significantly larger deformations, in comparison to the sandstones.

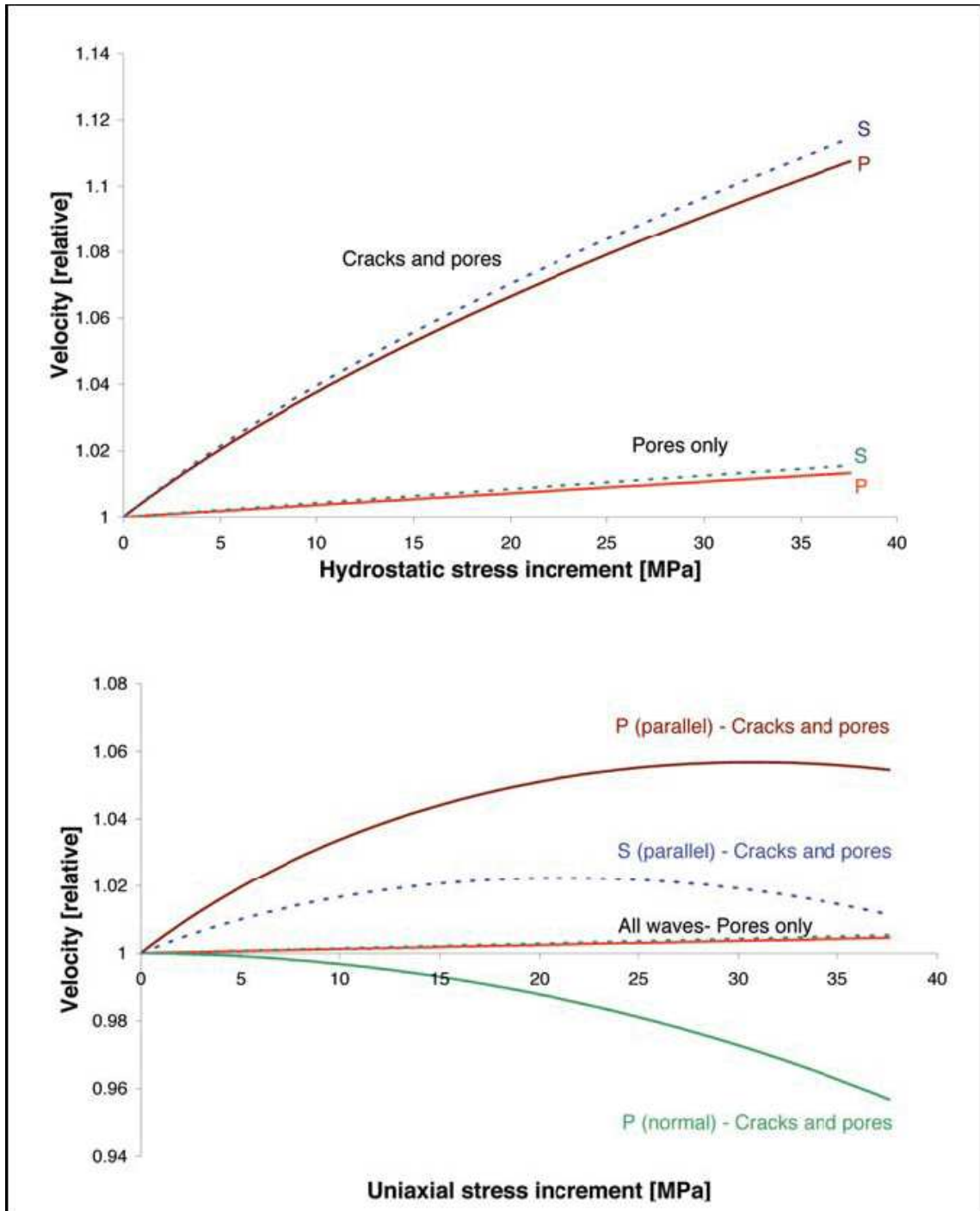


Figure 4.15. Model calculations, illustrating the impact of flat cracks and spherical pores on the stress sensitivity of the wave velocities. Initial crack distribution is isotropic. Stress-induced anisotropy is observed in the uniaxial case on the crack model by Holt *et al.* (2005). Parallel refers to propagation in the direction of uniaxial stress and normal refers to propagation normal to the uniaxial stress.

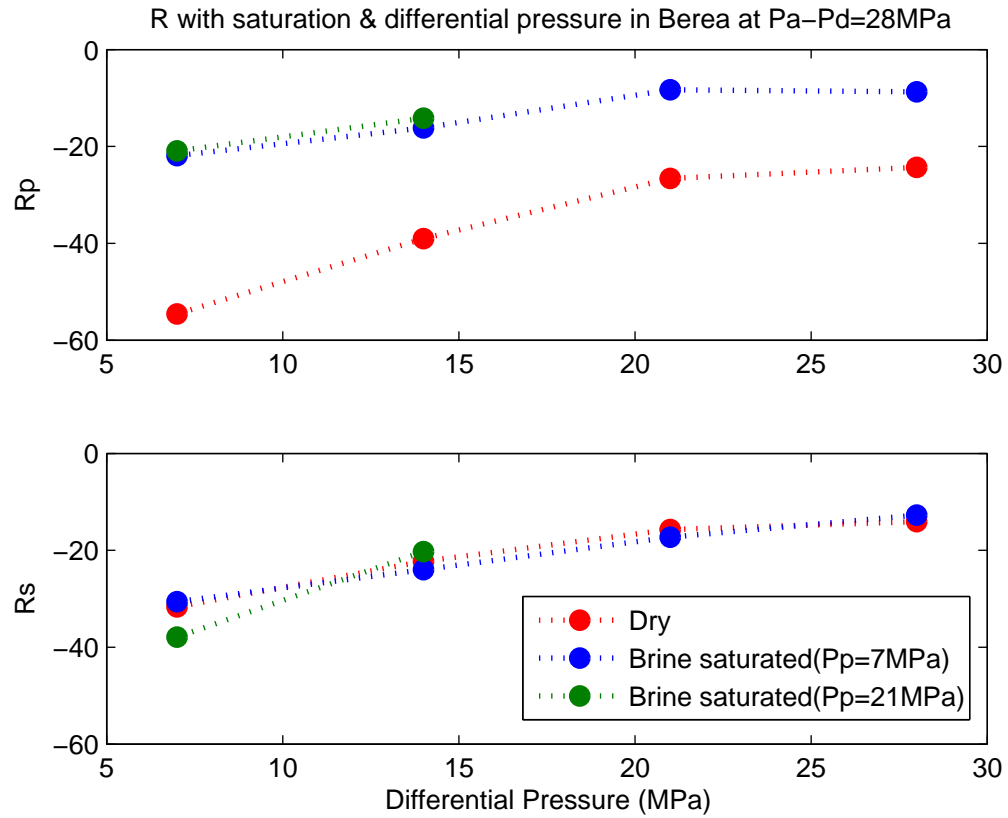


Figure 4.16. Sensitivity of  $R$  to fluid saturation and differential pressure at a constant difference between the axial stress and the differential pressure in Berea sandstone. Absolute  $R_p$  value decreases with fluid saturation and increasing differential pressure.  $R_s$  is insensitive to fluid saturation.

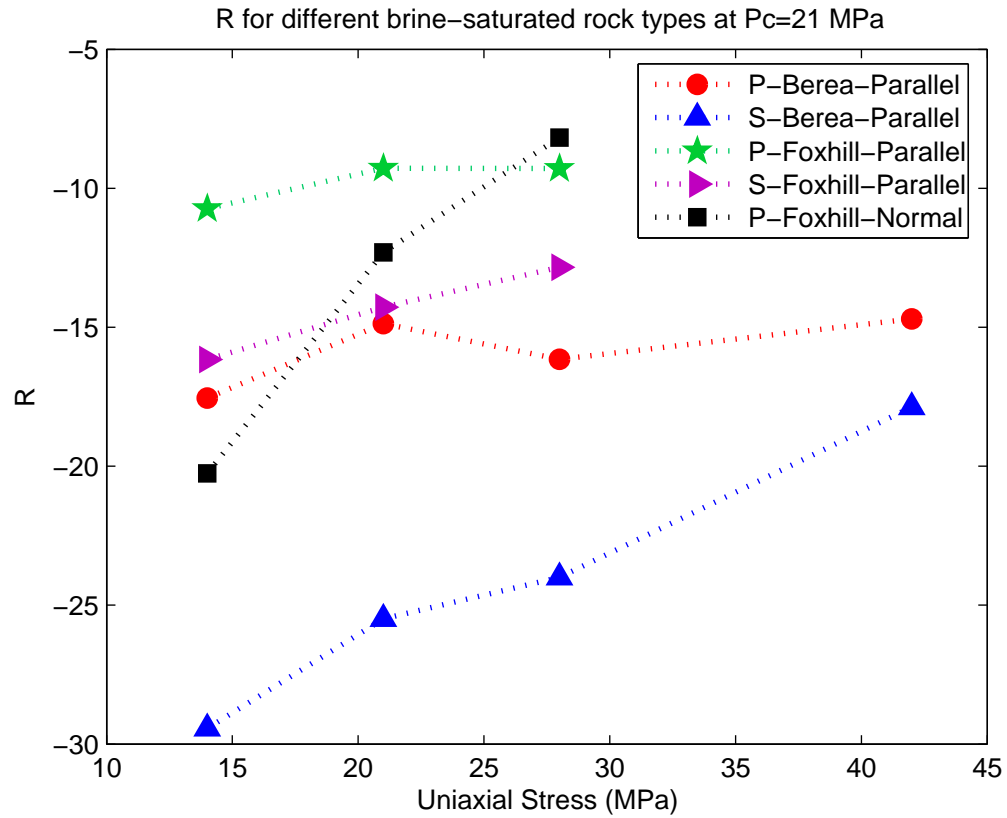


Figure 4.17.  $R$  values are plotted against uniaxial stress at a constant differential pressure  $P_d$  of 14 MPa ( $= 21(P_c) - 7(P_p)$ ). Parallel and normal are with respect to the axial stress direction. Notice the large crack-induced anisotropy in  $R$  values for Foxhill.

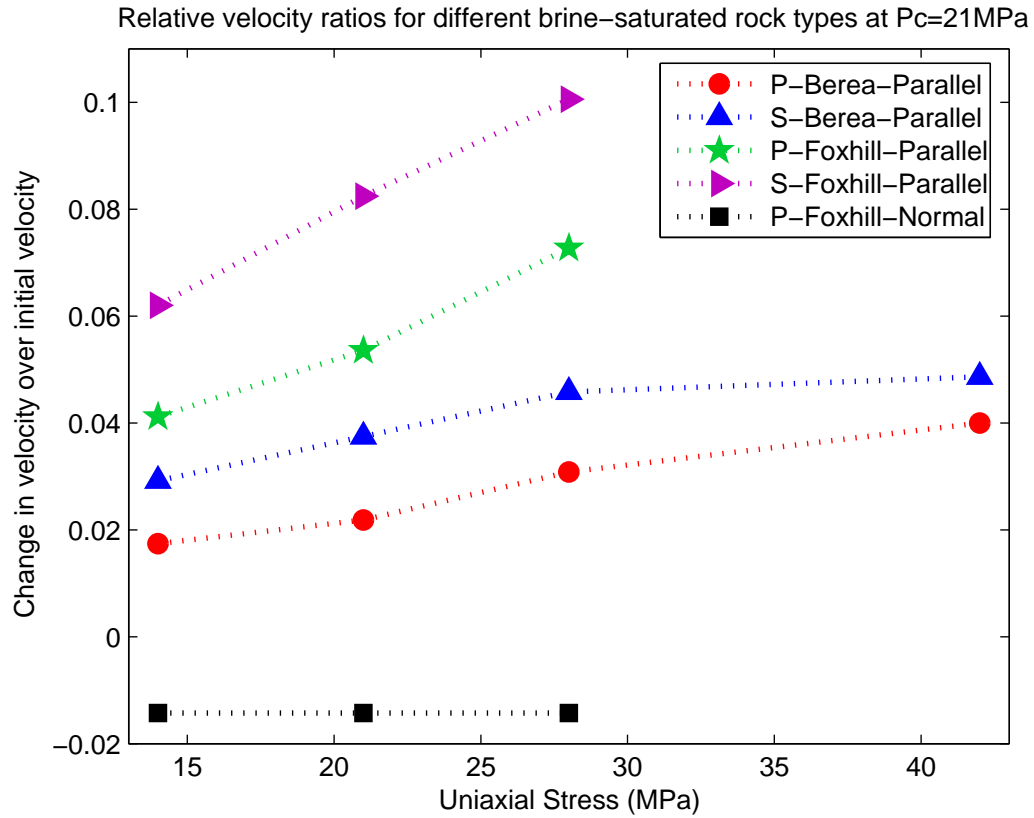


Figure 4.18. Change in velocities over initial velocity as a function of uniaxial stress. Velocity increases in the direction parallel to uniaxial stress probably due to crack closure and its magnitude increases with uniaxial stress. Velocity decreases due to elongation in the direction normal to the axial stress direction, but its magnitude is insensitive to the increase in uniaxial stress.

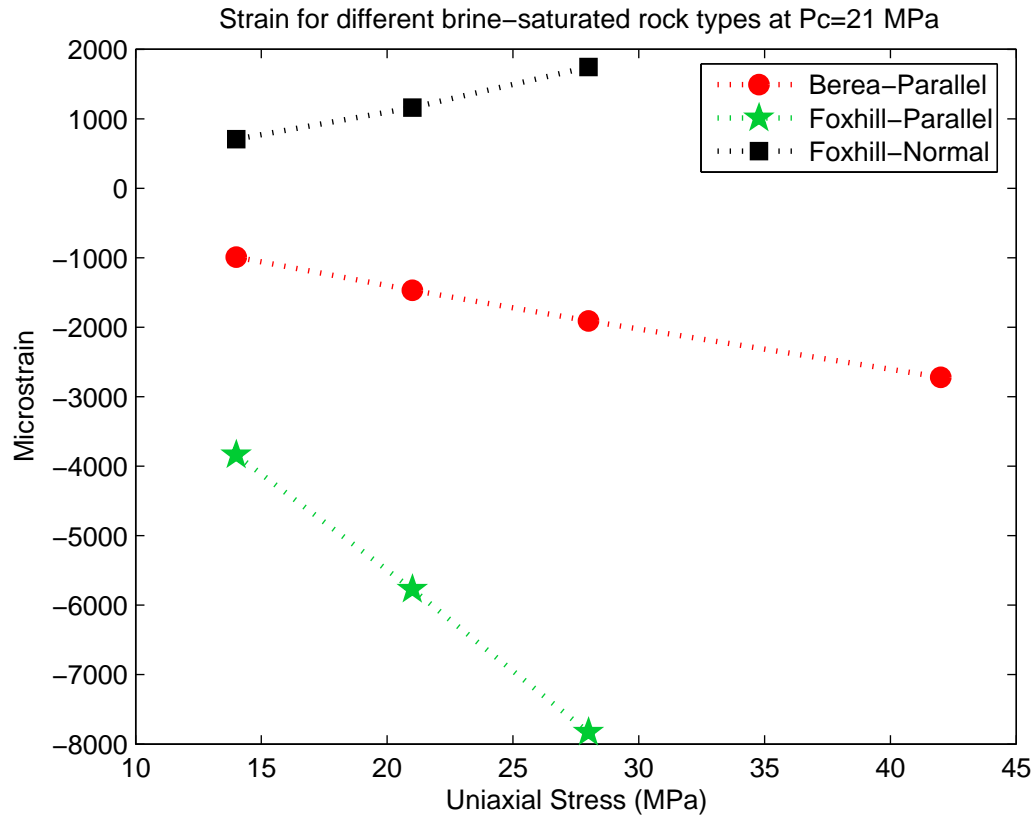


Figure 4.19. Strain versus uniaxial stress. Negative strains parallel to the axial direction represent compaction, which increases with uniaxial stress. There is elongation in the direction normal to axial direction in Foxhill sandstone. Elongation also increases with uniaxial stress.

#### 4.5.5 R Value Comparison

Janssen *et al.* (2006) presented a comparison of  $R$  values calculated from 4D seismic data, velocity porosity trends and core analysis. Their core experiments from the Ekofisk reservoir, which is mostly chalk ( $-R = 10$  to  $30$ ), also show much larger stress sensitivity of  $R$ , than what is observed in seismic data or is predicted from rock physics trends.

In time-lapse seismic data (Equation 4.14), the velocities correspond to the dynamic mechanism, while strain is inferred from static mechanisms, such as sea floor subsidence and reservoir compaction (Hatchell & Bourne, 2005a; R  ste *et al.*, 2005):

$$\Delta t = (1 - R)\epsilon_{zz}t \quad (4.14)$$

where,  $\Delta t$  = time-lapse time shifts,  $\epsilon_{zz}$  = vertical strain,  $t$  = travel time for normal incidence vertical P-wave and  $R$  = dilation factor. Theoretical models that use rock properties trends, derived from velocity-porosity regression, microcrack model, asperity-deformation model and Hertz-Mindlin model (R  ste *et al.*, 2005; Hatchell & Bourne, 2005b; Carcione *et al.*, 2007) use the same dynamic mechanism to calculate the change in velocities as well as strains. Hence comparing those modeled  $R$  values with the 4D seismic data is inconsistent and new models need to be developed.

Numerous other investigations have documented the change in velocities with increasing stress. However, the sample deformations occurring during these measurements are rarely reported. But, we can estimate the static strains from dynamic velocities, by ignoring the differences between the static and dynamic elastic properties. We have calculated  $R$  values from dynamic measurements using the following procedure. The dynamic Young's modulus values were calculated from the acoustic

velocities using Equation 4.10. The strain was calculated using Equation 4.9, assuming that the static and dynamic Young's moduli are the same.  $R$  was then computed using Equation 4.8. For example, an estimated  $R$  value of -739 was extracted when a block of Berea sandstone was subjected to a uniaxial stress of 6 MPa parallel to the bedding plane, in an unconfined and dry condition (Sarkar *et al.*, 2003). This is compared with our  $R$  value of -100 (dynamic strain) and -58 (static strain) for a uniaxial stress increase of 7 MPa in Berea sample. Since the uniaxial stress was applied normal to the bedding plane in our study, we saw much higher strains and therefore lower  $R$  values. The difference in  $R$  values can also be explained by the fact that the Berea block of Sarkar *et al.* (2003) was subjected to uniaxial stress in an unconfined state, whereas our sample was subjected to uniaxial stress at 7 MPa confined stress.

Our  $R$  values for North Sea shale varied from -8.5 to -6 with hydrostatic pressure decrease and -11 to -6 with uniaxial stress increments. The dynamic  $R$  values extracted from (Wang, 2002) are higher than our  $R$  values for shales. Since shales mostly have lower aspect ratio pores, we expect that the dynamic mechanism does not correctly represent them.

## 4.6 Conclusions

$R$  values are strongly dependent on the stress state, hence using a constant value of  $R$  from the seafloor (unconfined stress state) to the reservoir depth (higher confined stress state) should be avoided. Reduced stress sensitivities of velocities at higher confining pressures and greater strains (due to higher aspect ratio pores closing) lead to lower absolute values of  $R$  in sandstones. The absolute  $R$  values for P-waves are lower for fluid-filled rocks because the presence of fluid makes the



rock stiffer.  $R$  values are different for P and S waves, especially in the presence of fluids. As PS converted waves are used in 4D monitoring, using the same value of  $R$  for P and S waves can lead to errors in assessing production related changes.  $R$  values depend on the density of cracks and their alignment with respect to the stress direction. Intrinsic anisotropy and stress-induced crack anisotropy play an important role in the understanding of  $R$  values, though crack-induced anisotropy is lower at higher confining pressures and in fluid-filled rocks.

Dynamic Young's modulus is generally higher than static Young's modulus as they correspond to different deformation mechanisms. The ratio of dynamic to static modulus increases in crack-dominated rocks at lower confining pressures. For high aspect ratio pore-dominated rocks, the ratio of dynamic to static Young's modulus almost remains constant with increasing uniaxial stress. In rocks with a higher density of cracks parallel to the axial stress direction, this ratio increases with uniaxial stress increments. This ratio should decrease if there is a higher density of cracks normal to the axial stress direction.  $R$  values are dependent on the deformation mechanisms controlling the strain. Hence comparing the theoretical models based on rock properties trends with 4D seismic data is inconsistent as none of the models calculate the strain from static deformation mechanism.

This study shows that absolute  $R$  values increase for sandstones and decrease for shales with decreasing confining pressure. These trends matched with modeled  $R$  values for both sandstones and shales (Carcione *et al.*, 2007). Lower values of  $R$  from 4D seismic data can be explained by the fact that 4D seismic data sees the combined effect of the overburden (shales) and reservoir (sandstones) rocks. Fluid filled reservoir rocks, buried deep in the earth (higher confining pressures) lead to lower absolute values of  $R$ . Overburden occupies a larger area than the reservoir

leading to a dominant role. Lowering of the  $R$  values for shales with decreasing confining pressure reduces  $R$  values further as we move up to the sea floor from just above the reservoir. Our data not only offers insight into the behavior of  $R$  values with different rock types, stress and fluid but they can also be used to constrain models.

## Chapter 5

### CONCLUSIONS

#### 5.1 Introduction

In this dissertation, the elastic properties of clays have been studied using various methods. At the end of every chapter, conclusions have been presented related to the particular method. Here, an attempt is made to provide general conclusions from the overall work conducted, and to propose suggestions for future work that can supplement and advance these investigations.

#### 5.2 Conclusions

A multi-method approach to obtain and understand the elastic properties of clays was adopted consisting of modeling and experiments so that they complement and validate each other. Clay interlayer properties were modeled using Monte-Carlo molecular simulation for different stress values and number of water molecules. Our analyses of the equilibrium molecular structure of montmorillonite at various stresses and hydration states show that swelling behaves in a non-linear way with stress. The swelling behavior of clays under stress cannot be simply explained by bulk liquid water properties, but is an intricate interplay of the siloxane surface, cation solvation effects and stress on the interlayer water.

Nanoindentation studies were performed on fused silica, glass substrate alone, a

thin film of muscovite mica deposited on glass substrate, kaolinite film with different grain sizes and different montmorillonites on glass substrate. The orientation and water content in our samples were confirmed to reduce the number of unknown parameters. Nanoindentation measurements of muscovite film on glass substrate showed that contact area can be estimated correctly and easily if the film and substrate have similar elastic properties. The greatest challenge of working with delicate thin films like clays was achieving a good contact between the indenter tip and the sample. Adhesion forces and shifting of clay platelets cause measurement of void spaces between clay platelets leading to near zero values in case of smaller grain sizes of clay (1-2  $\mu\text{m}$ ). Larger grain sizes (5-8  $\mu\text{m}$ ) of clays help in achieving a better contact with the indenter tip. Lower strain rates and harder material like montmorillonite gave us more stable results than kaolinite. Working with sensitive and delicate thin films will improve from the experiences gained from this study in the areas of sample preparation, measurement technique, and analysis scheme development.

On a larger scale, the deformation of a shale sample was also examined. Experiments to study dilation factor under different stress conditions on sandstones and shale were performed. Dilation factor (R) is defined as the ratio of relative change in velocity to relative change in deformation. R has significant implications for time-lapse(4D) seismic studies where it can be used to infer reservoir or overburden thickness changes from seismic data, but there is a lot of uncertainty regarding their values. R values were found to be strongly dependent on stress; compliant pore content and their placements; and the presence of fluids. This study shows that absolute R values increase for sandstones and decrease for shales with decreasing confining pressure. These trends matched with modeled R values for sandstones and shale (Carcione *et al.*, 2007). Lower values of R from 4D seismic data can be explained

by the fact that 4D seismic data sees the combined effect of the overburden (shales) and reservoir (sandstones) rocks. Fluid filled reservoir rocks, buried deep in the earth (higher confining pressures) lead to lower absolute values of  $R$ . Lowering of  $R$  values for shales with decreasing confining pressure reduces the  $R$  values further as we move up to the sea floor from just above the reservoir. Our data not only offers insight into the behavior of  $R$  values with different rock types, stress and fluid but they can also be used to constrain model calculations.

Simulation results (5 GPa to 16 GPa) matched very well with experimental results (4 GPa to 14 GPa) for Young's modulus of montmorillonite. This agreement between the independent modeling and experimental approaches validates our results. Nanoindentation measures a composite of clay and interlayer properties. Molecular simulation models the interlayer property alone, as the clay layers are kept stiff, since most of the deformation occurs in the interlayer (Katti *et al.*, 2005b). Being the softer component, the interlayer is responsible for most of the deformation and dominates the clay mechanical properties. In montmorillonite, or other swelling clays, the volume fraction of the interlayer can be higher than the clay layer in the presence of water, thus making it even more prominent. Molecular simulation shows that steps occur in Young's modulus profile with the formation of new water layers, but they subsequently become smaller and wider with successive water layers. These changes in modulus can be explained with density variations (Music *et al.*, 2003) of the interlayer water. The density variations are related to the arrangement of water molecules in the interlayer Boek *et al.* (1995). Nanoindentation measurements for Young's modulus could not resolve those small steps leading to similar values for SCa 3 and SWy 2, although they had different interlayer water contents. The strain in the samples due to different stress states in the rock physics measurements for dilation

factor give us the static elastic modulus. Static Young's modulus obtained for our North Sea Shale varied from 2.6 GPa to 5 GPa.

Different kinds of measurements at different scales showing overlap is very encouraging and points to the importance of individual clay components in the composition of shale. This work defines the clay mineral modulus from molecular modeling, verified and complemented by experimental truth from nanoindentation. Elastic modulus of clays can finally be used in the design of advanced polymers instead of approximating them with mica modulus. This clay mineral modulus can be directly used to find the effective elastic properties of shale for pore fluid substitution, using Gassmann's equations (Gassmann, 1951), in contact models for clay-rich rocks (Dvorkin & Nur, 1996) and for calculating the acoustic properties with clay content for sand-clay mixtures (Marion *et al.*, 1992). The direct application of clay mineral modulus is seen in the effective elastic modulus of shale, measured from our dilation factor experiments.

This dissertation answers a number of research questions, but opens up doors for more questions to be addressed.

### 5.3 Suggestions for Future Work

There is always scope for performing the measurements at different scales, either higher or lower than those presented in this thesis. It would be very interesting and challenging to determine the modulus of a single lamella of a clay mineral (Piner *et al.*, 2003), independent of its interlayer properties, at one end. Methodology to remove the chemicals used to extract a single lamella of clay mineral will need to be developed. On the other end, indentation can be performed on shales and then statistical analysis used to estimate the elastic properties of clays (Bobko & Ulm,

2008).

Future researchers can also extend these measurements to study modulus variation with different orientations of clay platelets, which will give us the true Poisson's ratio for these highly anisotropic minerals. Care must be taken to prepare the sample so that a good contact between the indenter tip and the sample is achieved.

A microscope with better resolution can be linked to the nanoindenter, which might be helpful in forcing the indenter tip to avoid the impurities in the clay sample with more certainty. Nanoindentation measurements with controlled relative humidity might improve the resolution in the present data, although the humidity might adversely affect the high precision nanoindenter apparatus, so it needs to be designed so that only the sample is at constant relative humidity.

Molecular simulation has numerous possibilities. Different clay models, different cations, different orientation and different materials in the interlayer can be simulated. The simulation can be extended by making the clay layers flexible.

Dilation factor and static Young's modulus measurements can be performed on other varieties of shales with different clay contents and types.

Another area that requires further investigation is upscaling. Since there is data from the molecular level to the bulk level in this dissertation, one can use them to constrain models for shales (Hornby *et al.*, 1994), to be directly used in seismic studies.

## REFERENCES

- Adam, L., Batzle, M., & Brevik, I. 2006. Gassmann's fluid substitution and shear modulus variability in carbonates at laboratory seismic and ultrasonic frequencies. *Geophysics*, **71**(6), F173–F183.
- Allen, M.P., & Tildesley, D.J. 1987. *Computer Simulation of Liquids*. Oxford, UK: Oxford University Press.
- Aston, S.D., Challis, R.E., & Yiasemides, G.P. 2002. The dependence of the elastic properties of silica/alumina materials on the conditions used for firing. *Journal of the European Ceramic Society*, **22**, 1119–1127.
- Ball, Vaughn., & Batzle, M. 1994. Contrasting stress dependence of compressional and shear velocities : Implications for laboratory, logging, and seismic measurements. *Annual International Meeting, SEG Expanded Abstracts*, **13**, 1065–1068.
- Barsoum, M.W., Murugaiah, A., Kalidindi, S.R., & Zhen, T. 2004. Kinking non linear elastic solids, nanoindentations, and Geology. *Physical Review Letters*, **92**(25), 255508 1–255508 4.
- Batzle, M.L., Han, D.H., & Hofmann, R. 2006. *Rock properties, in: Petroleum Engineering Handbook*. Vol. I. SPE. Pages 571–685.
- Birch, F. 1960. The velocity of compressional waves in rocks to 10 kilo bars, Part 1. *J. Geophys. Res*, **65**, 1083–1102.
- Bobko, C., & Ulm, F.-J. 2008. The nano-mechanical morphology of shale. *Mechanics of Materials*, **40**, 318–337.
- Boek, E.S., Coveney, P.V., & Skipper, N.T. 1995. Monte Carlo Molecular Modeling Studies of Hydrated Li-, Na-, and K-Smectites: Understanding the Role of Potassium as a Clay Swelling Inhibitor. *J. Am. Chem. Soc.*, **117**(50), 12608–12617.
- Bowers, T.S. 1995. *Pressure-Volume-Temperature properties of H<sub>2</sub>O – CO<sub>2</sub> fluids, in Rock Physics and Phase Relations: A Handbook of Physical Constants*. Vol. 3. Washington, D. C.: AGU.
- Bradley, W.F., Grim, R.E., & Clark, G.F. 1937. A study of the behavior of montmorillonite on wetting. *Z. Kristallogr.*, **97**, 260–270.



- Carcione, J., Landrø, M., Gangi, A.F., & Cavallini, F. 2007. Determining the dilation factor in 4D monitoring of compacting reservoirs by rock-physics models. *Geophysical Prospecting*, **55**(6), 793–804.
- Chen, B., & Evans, J.R.G. 2006. Elastic moduli of clay platelets. *Scripta Materialia*, **54**, 1581–1585.
- Chilingar, George V., & Knight, Larry. 1960. Relationship between pressure and moisture content of kaolinite, illite and montmorillonite clays. *Bulletin of the American Association of Petroleum Geologists*, **44**(1), 101–106.
- Chipera, S.J., & Bish, D.L. 2001. Baseline studies of the Clay Minerals Society source clays: Powder Xray diffraction analyses. *Clays and Clay Minerals*, **49**(5), 398–409.
- Colten-Bradley, Virginia A. 1987. Role of pressure in smectite dehydration-Effects on geopressure and smectite-to-illite transformation. *Bulletin of the American Association of Petroleum Geologists*, **71**(11), 1414–1427.
- de Pablo, L., Chavez, M.L., Sum, A.K., & de Pablo, J.J. 2004. Monte Carlo molecular simulation of the hydration of Na montmorillonite at reservoir conditions. *J. Chem. Phys.*, **120**(2), 939–946.
- Dewhurst, D.N., Siggins, A.F., Clennell, M.B., Raven, M.D., & Nordgård-Bolås, H.M. 2007. The ultrasonic response of North Sea shale to undrained loading. *Annual International Meeting, SEG Expanded Abstracts*, **26**, 1525–1529.
- Dobereiner, L., & DeFreitas, M.H. 1986. Geotechnical properties of weak sandstones. *Geotechnique*, **36**, 79–94.
- Dvorkin, J., & Nur, A. 1996. Elasticity of high-porosity sandstones: Theory for two North Sea datasets. *Geophysics*, **61**, 1363–1370.
- Enderby, J.E., & Neilson, G.W. 1981. The structure of electrolyte solutions. *Reports on Progress in Physics*, **44**, 593–653.
- Faust, J., & Knittle, E. 1994. The equation of state, amorphization, and high-pressure phase diagram of muscovite. *J. Gephys. Res.*, **99**, 19785–19792.
- Ferris, Dr. James P. 1993. Montmorillonite Catalysis of RNA oligomer Formation in Aqueous Solution. A model for the Prebiotic Formation of RNA. *J. Am. Chem. Soc.*, **115**(11), 12270–12275.
- Frenkel, D., & Smit, B. 2002. *Understanding molecular simulation*. Academic Press.

Fuck, R.F., Bakulin, A., & Tsvankin, I. 2007. Theory of traveltimes shifts around compacting reservoirs: 3D solutions for prestack data. *Annual International Meeting, SEG Expanded Abstracts*, **26**, 2929–2933.

Gassmann, F. 1951. Über die Elastizität poröser Medien. *Vier. der Natur. Gesellschaft in Zürich*, **96**, 1–23.

Ghafoori, M., Mastropasqua, M., Carter, J.P., & Airey, D.W. 1993. Engineering properties of ashfield shale, Australia. *Bulletin of Engineering Geology and the Environment*, **48**(1), 43–58.

Grygar, Tomas, Bezdicka, Peter, Hradil, David, Hruskova, Michaela, Novotna, Katrina, Kadlec, Jaroslav, Pruner, Peter, & Oberhansli, Hedi. 2005. Characterization of expandable Clay Minerals in Lake Baikal sediments by Thermal Dehydration and cation exchange. *Clays and Clay Minerals*, **53**(4), 389–400.

Guggenheim, S., & Koster Van Groos, A.F. 2001. Baseline studies of the Clay Minerals Society source clays: Thermal Analysis. *Clays and Clay Minerals*, **49**(5), 433–443.

Habelitz, S., Carl, G., & Russel, C. 1997. Mechanical Properties of oriented mica glass ceramics. *J. Non-Cryst. Solids*, **220**, 291–298.

Han, D.H., Nur, A., & Morgan, D. 1986. Effects of Porosity and Clay Content on wave velocities in Sandstones. *Geophysics*, **51**, 2093–2107.

Hariharan, P. 1996. *Interferometers in Handbook of Optics*. New York: McGraw-Hill Companies, Inc.

Hatchell, P. J., Beukel, A. van den., Molenaar, M. M., Maron, K. P., Kenter, C. J., Stammeijer, J. G. F., Velde, J. J. van der., & Sayers, C. M. 2003. Whole earth 4D : Reservoir monitoring geomechanics. *Annual International Meeting, SEG Expanded Abstracts*, **73**, 1330–1333.

Hatchell, P.J., & Bourne, S.J. 2005a. Measuring reservoir compaction using time-lapse timeshifts. *Annual International Meeting, SEG Expanded Abstracts*, **24**, 2500–2503.

Hatchell, P.J., & Bourne, S.J. 2005b. Rocks under strain: Strain-induced time-lapse time shifts are observed for depleting reservoirs. *The Leading Edge*, **24**(12), 1222–1225.

Hoek, E., & Brown, E. T. 1980. *Underground excavations in rock*. Inst. Mining and Metal., London.

- Holt, R.M., Nes, O-M., & Fjaer, E. 2005. In-situ stress dependence of wave velocities in reservoir and overburden rocks. *The Leading Edge*, **24**(12), 1269–1274.
- Hornby, B.E., Schwartz, L.M., & Hudson, J.A. 1994. Anisotropic effective-medium modeling of the elastic properties of shales. *Geophysics*, **59**, 1570–1583.
- Horsrud, P. 2001. Estimating mechanical properties of shale from empirical correlations. *SPE Drill. Complet.*, **16**, 68–73.
- Horsrud, P., Sønstebo, E.F., & Bøe, R. 1998. Mechanical and petrophysical properties of North Sea Shales. *Int. J. Rock. Mech. Min. Sc.*, **35**(8), 1009–1020.
- Janssen, A.L., Smith, B.A., & Byerley, G.W. 2006. Measuring velocity sensitivity to production-induced strain at the Ekofisk Field using time-lapse time-shifts and compaction logs. *Annual International Meeting, SEG Expanded Abstracts*, **25**, 3200–3204.
- Jizba, D., Mavko, G., & Nur, A. 1990. Static and Dynamic Moduli of Tight Gas sandstone. *Annual International Meeting, SEG Expanded Abstracts*, **9**, 827–829.
- Jizba, D.L. 1991. *Mechanical and acoustical properties of sandstones and shales*. Ph.D. thesis, Stanford University.
- Jones, L. E. A., & Wang, H. F. 1981. Ultrasonic velocities in Cretaceous shales from the Williston basin. *Geophysics*, **46**, 288–297.
- Jorgensen, William L., Chandrasekhar, Jayaraman, Madura, Jeffery D., Impey, Roger W., & Klein, Michael L. 1983. Comparison of simple potential functions for simulating liquid water. *J. Chem. Phys.*, **79**(2), 926–935.
- Joslin, D.L., & Oliver, W.C. 1990. A new method for analyzing data from continuous depth-sensing microindentation tests. *J. Mater. Res.*, **5**(1), 123–126.
- Karaborni, S., Smit, B., Heidug, W., Urai, J., & Oort, van E. 1996. The Swelling of Clays: Molecular Simulations of the Hydration of Montmorillonite. *Science*, **271**(5252), 1102–1104.
- Katahara, K. W. 1996. Clay mineral elastic Properties. *Annual International Meeting, SEG Expanded Abstracts*.
- Katti, D., Schmidt, S., Ghosh, P., & Katti, K. 2005a. An insight into clay-water molecular interactions in the interlayer of Na-montmorillonite subject to external stress. *Poromechanics-Biot Centennial (1905-2005)*.

- Katti, D., Schmidt, S., Ghosh, P., & Katti, K. 2005b. Modeling the response of pyrophyllite interlayer to applied stress using steered molecular dynamics. *Clays and Clay Minerals*, **53**(2), 171–178.
- Komadel, P. and Hrobarikova, J., Smrcok, L., & Koppelhuber-Bitschnau, B. 2002. Hydration of reduced-charge montmorillonite. *Clay Minerals*, **37**(3), 543–550.
- Laird, David A. 1999. Layer change influences on the hydration of expandable 2:1 Phyllosilicates. *Clays and Clay Minerals*, **47**(5), 630–636.
- Ledbetter, H., Kim, S., Dunn, M., Xu, Z., Crudele, S., & Kriven, W. 2001. Elastic constants of mullite containing alumina platelets. *Journal of the European Ceramic Society*, **21**, 2569–2576.
- Likos, William J., & Lu, Ning. 2002. Water Vapor Sorption Behavior of Smectite-Kaolinite Mixtures. *Clays and Clay Minerals*, **50**(5), 553–561.
- Likos, William J., & Lu, Ning. 2006. Pore-Scale Analysis of Bulk Volume Change from crystalline swelling in  $\text{Na}^+$  and  $\text{Ca}^{++}$  smectite. *Clays and Clay Minerals*, **54**(4), 515–528.
- Liu, Chen-Wuing, & Lin, Wen-Sheng. 2005. A Smectite Dehydration Model in a Shallow Sedimentary Basin: Model development. *Clays and Clay Minerals*, **53**(1), 55–70.
- Logsdon, Sally D., & Laird, David A. 2004. Electrical conductivity spectra of smectites as influenced by saturating cation and humidity. *Clays and Clay Minerals*, **52**(4), 411–420.
- Manevitch, O.L., & Rutledge, G.C. 2004. Elastic Properties of a Single Lamella of Montmorillonite by Molecular Dynamics Simulation. *J. Phy. Chem.B*, **108**, 1428–1435.
- Marion, D., Nur, A., & Han, D. 1992. Compressional velocity and porosity in sand-clay mixtures. *Geophysics*, **57**, 554–563.
- Matsouka, O., Clementi, E., & Yoshimine, M. 1976. CI study of the water dimer potential surface. *J. Chem. Phys.*, **64**, 1351–1361.
- Mcneil, L.E., & Grimsditch, M. 1993. Elastic moduli of muscovite mica. *J. Phys. Condens. Matter*, **5**, 1681–1690.
- Measurements-Group, Inc. Tech Notes. *TN-506, Bondable Resistance Temperature Sensors and Associated Circuitry; TN-507, Errors due to Wheatstone bridge non-linearity; and TN-514, Shunt Calibration of Strain Gage Instrumentation.*

- Metropolis, N., Rosenbluth, A.W., Rosenbluth, M.N., & Teller, A.H. 1953. Equations of state calculations for fast computing machines. *J. Chem. Phys.*, **21**(6), 1087–1092.
- Micro-Measurements. Product Bulletin PB-105. *Temperature Sensors and LST Matching Networks*.
- Mikowski, A., Soares, P., Wypych, F., Gardolinski, J.E.F.C., & Lepienski, C.M. 2007. Mechanical properties of kaolinite macro-crystals. *Philosophical Magazine*, **87**(29), 4445–4459.
- Mooney, R.W., Keenan, A.C., & Wood, L.A. 1952. Absorption of water vapour by montmorillonite. *J. Am. Chem. Soc.*, **74**, 1367–1374.
- Moore, D.M., & Hower, John. 1986. Ordered interstratification of dehydrated and hydrated Na-smectite. *Clays and Clay Minerals*, **34**, 379–384.
- Moore, Duane M., & Reynolds, JR. Robert C. 1989. *X-ray diffraction and the identification and analysis of clay minerals*. Oxford, New York: Oxford University Press.
- Music, D., Kreissig, U., Czigány, ZS., Helmersson, U., & Schneider, J.M. 2003. Elastic modulus-density relationship for amorphous boron suboxide thin films. *Applied Physics A*, **76**, 269–271.
- Nagelschmidt, G. 1936. The structure of montmorillonite clays. *Z. Kristallogr.*, **93**, 481–487.
- Newman, A.C.D. 1987. *Chemistry of Clays and Clay minerals*. Mineralogical Society.
- Oliver, W.C., & Pharr, G.M. 1992. An improved technique for determining hardness and elastic modulus using load and displacement sensing indentation experiments. *J. Mater. Res.*, **7**, 1564–1583.
- Olsen, C., Christensen, H.F., & Fabricius, I.L. 2008. Static and Dynamic Young's modulus of chalk from the North Sea. *Geophysics*, **73**(2), E41–E50.
- Palko, J.W., Sayir, A., Sinogeikin, S.V., Kriven, W.M., & Bass, J.D. 2002. Complete elastic tensor for mullite ( $2.5\text{Al}_2\text{O}_3\cdot\text{SiO}_2$ ) to high temperatures measured from textured fibers. *Journal of the American Ceramic Society*, **85**, 2005–2012.
- Park, S.H., & Sposito, G. 2003. Do montmorillonite surfaces promote methane hydrate formation?: Monte Carlo and molecular dynamics simulations. *J. Phy. Chem.B*, **107**, 2281–2290.

- Piner, R.D., Xu, T.T., Fisher, F.T., Qiao, Y., & Ruoff, R.S. 2003. Atomic Force Microscopy Study of Clay Nanoplatelets and Their Impurities. *Langmuir*, **19**, 7995–8001.
- Prasad, M. 2001. Mapping Impedance Microstructures in Rocks with Acoustic Microscopy. *The Leading Edge*, **20**, 172–179.
- Prasad, M., Kopycinska, M., Rabe, U., & Arnold, W. 2002. Measurement of Young's modulus of clay minerals using atomic force acoustic microscopy. *Geophysical Research Letters*, **29**, 13–16.
- Røste, T., Stovas, A., & Landrø, M. 2005. *Estimation of layer thickness and velocity changes using 4D prestack seismic data*. Ph.D. thesis, Norwegian University of Science and Technology (NTNU).
- Saha, R., & Nix, W.D. 2002. Effects of the substrate on the determination of thin film mechanical properties by nanoindentation. *Acta Materialia*, **50**, 23–38.
- Sarkar, D., Bakulin, A., & Kranz, R.L. 2003. Anisotropic inversion of seismic data for stressed media: Theory and a physical modeling study on Berea Sandstone. *Geophysics*, **68**(2), 690–704.
- Sato, H., Ono, K., Johnston, C.T., & Yamagishi, A. 2005. First-principles studies on the elastic constants of a 1:1 layered kaolinite mineral. *American Mineralogist*, **90**, 1824–1826.
- Sayers, C.M., & Kachanov, M. 1995. Microcrack-induced elastic wave anisotropy of brittle rocks. *J. Geophys. Res.*, **100**, 4149–4156.
- Simmons, G., & Brace, W.F. 1965. Comparison of Static and Dynamic Measurements of Compressibility of Rocks. *J. Geophys. Res.*, **70**(22), 5649–5656.
- Skipper, N. T., Refson, K., & McConnell, J. D. C. 1991. Computer simulation of interlayer water in 2:1 clays. *J. Chem. Phys.*, **94**(11), 7434–7446.
- Skipper, N.T., Chang, Fang-Ru Chou, & Sposito, Garrison. 1995a. Monte Carlo simulation of interlayer molecular structure in swelling clay minerals; 1, Methodology. *Clays and Clay Minerals*, **43**, 285–293.
- Skipper, N.T., Chang, Fang-Ru Chou, & Sposito, Garrison. 1995b. Monte Carlo simulation of interlayer molecular structure in swelling clay minerals; 2, Monolayer hydrates. *Clays and Clay Minerals*, **43**, 294–303.

- Soper, A. K., Bruni, F., & Ricci, M. A. 1997. Site-Site pair correlation functions of water from 25 to 400 °C: Revised analysis of new and old diffraction data. *J. Chem. Phys.*, **106**, 247–254.
- Souza, G.B., Foerster, C.E., Silva, S.L.R., & Lepienski, C.M. 2006. Nanomechanical properties of rough surfaces. *Materials Research*, **9**(2), 159–163.
- Sposito, G., Park, S.-H., , & Sutton, R. 1999a. Monte Carlo simulation of the total radial distribution function for interlayer water in sodium and potassium montmorillonite. *Clays and Clay Minerals*, **47**(2), 192–200.
- Sposito, G., Skipper, N.T., Sutton, R., Park, S.-H., Soper, A.K., & Greathouse, J. 1999b. Surface geochemistry of the clay minerals. *Proc. Natl. Acad. Sci. USA*, **96**, 3358–3364.
- Tambach, Tim J., Bolhuis, Peter G., & Smit, Berend. 2004. A Molecular Mechanism of Hysteresis in Clay Swelling. *Angewandte Chemie International Edition*, **43**(20), 2650–2652.
- Tamura, Kenji, Yamada, Hirohisa, & Nakazawa, Hiromoto. 2000. Stepwise hydration of high-quality synthetic smectite with various cations. *Clays and Clay Minerals*, **48**(3), 400–404.
- Taylor, J.R. 1939. *An introduction to error analysis: the study of uncertainties in physical measurements*. Mill Valley Calif: University Science books.
- Teppen, B. J., Rasmussen, K., Bertsch, P. M., Miller, D. M., & Schafer, L. 1997. Molecular Dynamics Modeling of Clay Minerals. 1. Gibbsite, Kaolinite, Pyrophyllite, and Beidellite. *J. Phy. Chem.B*, **101**(9), 1579–1587.
- Thomsen, L. 1986. Weak elastic anisotropy. *Geophysics*, **51**, 1954–1966.
- Tosaya, C.A. 1982. *Acoustical properties of clay-bearing rocks*. Ph.D. thesis, Stanford University.
- Vallejo, L.E., & Lobo-Guerrero, S. 2005. The elastic moduli of clays with dispersed oversized particles. *Engineering Geology*, **78**, 163–171.
- Vanorio, T., Prasad, M., & Nur, A. 2003. Elastic properties of dry clay mineral aggregates, suspensions and sandstones. *Geophysical Journal International*, **155**, 319–326.
- Vaughan, M.T., & Guggenheim, S. 1986. Elasticity of muscovite and its relationship to crystal structure. *J. Gephys. Res*, **91**, 4657–4664.

- Vega, Sandra. 2003. *Intrinsic and stress-induced velocity anisotropy in unconsolidated sands*. Ph.D. thesis, Stanford University.
- Wang, Z. 2002. Seismic anisotropy in sedimentary rocks, part 2: Laboratory data. *Geophysics*, **67**(5), 1423–1440.
- Wang, Z., Wang, H., & Cates, M. E. 2001. Effective Elastic Properties of Solid Clays. *Geophysics*, **66**, 428–440.
- Woehler, A.F., Katz, S., & Ahrens, T.J. 1963. Elasticity of selected rocks and minerals. *Geophysics*, **28**, 658–663.
- Wyllie, M.R.J., Gregory, A.R., & Gardner, G.H.F. 1958. An experimental investigation of factors affecting elastic wave velocities in porous media. *Geophysics*, **23**, 459–493.
- Zaidan, Omar F., Greathouse, Jeffery A., & Pabalan, Roberto T. 2003. Monte Carlo and Molecular Dynamics Simulation of Uranyl Adsorption of Montmorillonite Clay. *Clays and Clay Minerals*, **51**(4), 372–381.
- Zhang, J., Al-Bazali, T.M., Chenevert, M.E., Sharma, M.M., Clark, D.E., Benaissa, S., & Ong, S. 2006. Compressive strength and acoustic properties changes in shales with exposure to water-based fluids. *U.S. Symposium on Rock Mechanics (USRMS)*, **41**(06900), 900–912.
- Zhang, J.-X. 1991. *Mechanical compaction and the brittle ductile transition in porous rocks: Geological implications for accretionary wedge seismicity*. Ph.D. thesis, SL University.
- Zimmer, M.A. 2003. *Seismic velocities in unconsolidated sands: Measurements of pressure, sorting and compaction effects*. Ph.D. thesis, Stanford University.
- Zunjarrao, S.C., Sriraman, R., & Singh, R.P. 2006. Effect of processing parameters and clay volume fraction on the mechanical properties of epoxy-clay nanocomposites. *J. Mater. Sc.*, **41**, 2219–2228.



## APPENDIX

The full appendix is included on a CD-ROM in a pocket inside the back cover of this thesis. This text serves only to outline what is contained on the CD. The files contained in the CD are:

|                 |   |
|-----------------|---|
| README.txt      | : Information about the files                                   |
| ini.txt         | : An example temperature and pressure input file                |
| ini ClayGeo.txt | : An example initial basal spacing and water content input file |
| out.txt         | : An example output file  |
| R.xyz           | : An example output clay structure                              |